

THE MAGNETIC SOLAR PHOTOSPHERE AND CORONA:
OBSERVATION, MODELING, AND PREDICTION

A DISSERTATION
SUBMITTED TO THE DEPARTMENT OF PHYSICS
AND THE COMMITTEE ON GRADUATE STUDIES
OF STANFORD UNIVERSITY
IN PARTIAL FULFILLMENT OF THE REQUIREMENTS
FOR THE DEGREE OF
DOCTOR OF PHILOSOPHY

Xudong Sun
August 2012

FOR MY PARENTS AND GRANDPARENTS

Abstract

The Sun’s magnetic field drives the dynamic behavior of its atmosphere and modulates the space weather conditions that we experience at the Earth. This dissertation focuses on the recent advances in understanding magnetic field measurements, static-state modeling of the corona, and their applications in space weather forecasting.

We revisit the full-Sun line-of-sight magnetic field data archive from the Michelson Doppler Imager (MDI). Using the Wang-Sheeley-Argge (WSA) model coupled with the potential field source surface (PFSS) model, we retrospectively optimize the space weather forecasting scheme for the MDI data. We evaluate the long-term performance of the model: the solar wind speed prediction near the Earth yields a 16% error over solar cycle 23, and the interplanetary magnetic field polarity is correctly predicted 81% of time. The prediction accuracy is strongly correlated with the activity cycle phase. We design a new interpolation scheme to estimate the unobserved magnetic field in the polar region which improves the solar wind speed prediction.

Making use of the PFSS model and the MDI data, we characterize the global-scale coronal and heliospheric magnetic field structure and its evolution during cycle 23. The modeled features agree reasonably well with remote-sensing and in-situ observations. The recent cycle displayed an extended minimum activity period, whose peculiar heliospheric consequences can be partly explained by a reduction of the polar magnetic field strength. The PFSS model may need to adopt a smaller source surface radius to better fit some observations.

We use a series of vector magnetograms from the Heliospheric and Magnetic Imager (HMI) to study the magnetic field and energy evolution of NOAA active region (AR) 11158. With the aid of a non-linear force-free field (NLFFF) extrapolation, we find substantial electric current and magnetic free energy increase during early flux emergence. The computed free energy is enough to power the ensuing X-class flare. We find a step-wise energy decrease during the flare, but the value is likely underestimated. The new observations confirm the rapid and irreversible change of the photospheric field during a major flare. The horizontal field was enhanced, with the field becoming more inclined

and more parallel to the polarity inversion line. Such change is consistent with the conjectured coronal field “implosion”.

Observation and modeling of this AR also illustrates the important role of magnetic topology. A small bipole emerged in the sunspot complex, subsequently created a quadrupolar flux system, and induced a series of eruptions with highly inclined trajectory. Field extrapolation suggests complicated magnetic connectivity with a coronal null point, which is supported by coronal observations. Owing to the asymmetrical photospheric flux distribution, the confining magnetic pressure decreases much faster horizontally than upward, and thus likely guided the non-radial eruption during its initial stage.

Acknowledgement

I am fortunate to have spent my years of graduate study at the Stanford Solar Physics group where I learned from and worked with so many wonderful people. I am grateful to Dr. Todd Hoeksema, my adviser, for his insightful remarks, fatherly encouragement, and patient guidance over the years. I am grateful to Prof. Phil Scherrer, for his support and the provision of such wonderful opportunity to work first-hand on the amazing new data. I am indebted to Yang Liu, Xuepu Zhao, and Keiji Hayashi, for their hands-on instruction and discussion on so many of the details of my research. There are so many people I have worked or collaborated with, in the Stanford group or outside, without whose help I could not have done half of what I am able to show in this dissertation: Thomas Wiegmann, Nick Arge, Marc DeRosa, Mike Turmon, Graham Barnes, Qingrong Chen, Chenglong Shen, and many, many more... I enjoyed my three-year residence at the Wilcox Solar Observatory: during all the routine observation procedures I have re-learned the value of self-containment. Last but not least, my life would not be complete without my family across the ocean and so many wonderful friends and classmates here, of all the time we spent on the phone, in the gym, on the trips... I could never be grateful enough for your love and companionship.

Contents

Abstract	v
Acknowledgement	vii
List of Tables	xii
List of Figures	xiii
1 Introduction	1
1.1 Sun, Solar Magnetic Field, Space Weather	1
1.2 Observing the Photospheric Magnetic Field	4
1.2.1 Zeeman Effect and Spectropolarimetry Inversion	4
1.2.2 Three Generations of Solar Telescopes at Stanford	5
1.2.3 Constructing Line-of-Sight Magnetic Maps	6
1.2.4 Constructing Vector Magnetic Maps	9
1.3 Modeling the Coronal Magnetic Field	11
1.3.1 The Quasi-Static, Force-Free Coronal Field	11
1.3.2 Potential Field Extrapolation	13
1.3.3 Force-Free Field Extrapolation	14
1.4 Outline of the Dissertation	15
2 Improving Space Weather Prediction: Optimizing the Wang-Sheeley-Argé (WSA)	
Model for MDI Data	17
2.1 Introduction	17
2.2 Optimization of the Scheme	20
2.3 MDI Solar Wind Velocity Prediction Result	22
2.3.1 Example Prediction	22

2.3.2	Statistical Evaluation	24
2.4	Factors Effecting Prediction Accuracy	27
2.4.1	The Optimization Scheme	27
2.4.2	Various Solar Features	29
2.5	Comparison Between Different Extrapolation Methods	31
2.5.1	Field Configurations	31
2.5.2	Different Field Line Mappings	33
2.5.3	Testing Correlation Between FTE and SW Speed	35
2.5.4	Space Weather Prediction with Different Extrapolations	35
2.6	Summary	37
3	Improving Space Weather Prediction: A New Polar Field Interpolation Scheme	39
3.1	Introduction	39
3.2	Brief Review of Existing Methods	40
3.2.1	Seven Interpolation Methods	40
3.2.2	Comments on Existing Methods	42
3.3	The New Interpolation Scheme	42
3.3.1	Procedures	42
3.3.2	Notes on the New Method	44
3.4	Validation and Discussion	46
3.4.1	WSA Model	46
3.4.2	MHD Simulation	50
3.5	Summary	51
4	Large-Scale Magnetic Field and Solar Wind During Solar Cycle 23	52
4.1	Introduction	52
4.2	Global Magnetic Field and Coronal Structure Near the Sun	53
4.2.1	Minimum vs. Maximum Phase	53
4.2.2	The Secular Evolution	55
4.3	SW Speed and IMF Polarity Near Earth	58
4.4	On the Peculiar Solar Minimum Phase Between Cycles 23-24	60
4.4.1	Weakened Solar Magnetic Field and Its Consequences	60
4.4.2	Implications for Field Extrapolation Models	63

5	Evolution of Magnetic Field and Energy in a Major Eruptive Active Region	68
5.1	Introduction	68
5.1.1	Energy Storage and Release	68
5.1.2	Data and Modeling	69
5.2	Long-Term Evolution	72
5.2.1	An Illustrative Snapshot	72
5.2.2	Long-term Evolution of Magnetic Field	74
5.2.3	Long-term Evolution of Magnetic Energy	76
5.2.4	On Energy Estimation	78
5.3	Rapid, Irreversible Field Changes During Major Flares	81
5.3.1	Field Change During the X-class Flare	81
5.3.2	Possible Causes and Consequences	87
5.4	Discussion on Field Extrapolation	89
5.5	Summary	91
6	Non-Radial Eruptions Modulated By Magnetic Field Topology	93
6.1	Introduction	93
6.1.1	Solar Eruption and Magnetic Topology	93
6.1.2	Data and Modeling	94
6.2	Non-Radial Eruption	95
6.3	Emerging Bipole As Energy Source	97
6.4	Interpretation Based on Magnetic Field Topology	100
6.4.1	Coronal Null and the Inclined Trajectory	100
6.4.2	The Inverted-Y Structure	102
6.4.3	Observational Evidence	103
6.5	Discussion	103
6.5.1	On the Coronal Field Topology	103
6.5.2	On the Flare Emissions	104
6.5.3	On the Eruption Mechanism	105
6.6	Summary	106
7	Concluding Remarks	108

A	Global Potential Extrapolation	111
A.1	Basic Equations	111
A.2	Issues on Normalization	114
A.3	Alternative Method for Computing g and h	115
A.4	PFSS-Like Models	116
B	Magnetic Field Topology Near A Null Point	119
B.1	Searching for Null Points	120
B.2	Spine and Fan Field Lines	121
B.3	Classification of Null Point	122
B.4	Error Estimation	123
	Bibliography	124

List of Tables

1.1	Three generations of solar telescopes at Stanford	5
2.1	Optimized WSA coefficients for different extrapolations and their prediction accuracy.	24
2.2	Statistical evaluation of in-ecliptic SW speed and IMF polarity prediction at L1 point	24
2.3	Prediction accuracy for different SW speed ranges	25
3.1	Statistical evaluation of solar wind speed prediction using different input	47
5.1	Estimated field parameters in the filament channel	73
5.2	Flare-related change in magnetic energy and photospheric field	84
A.1	Various forms of $R_l(r)$ in different potential models	117

List of Figures

1.1	Sunspot, coronal loops, streamers, and coronal mass ejection	2
1.2	LOS magnetograms from HMI and MDI	6
1.3	Regular and “timely-updated” synoptic maps from MDI	7
1.4	Automatically identified HMI active region patch	9
1.5	Vector magnetic maps for HARP 1638	10
2.1	Illustration of the WSA model	18
2.2	Characteristics of the empirical function	19
2.3	Example of the WSA model results	23
2.4	Statistical evaluation of the prediction from 1996 to 2009	26
2.5	Example of misleading prediction statistics	28
2.6	Prediction of recurring fast SW streams and their coronal sources	29
2.7	Drastic change of HCS ecliptic cross-over position	30
2.8	Illustration of coronal field derived from different extrapolations	32
2.9	Comparison of three extrapolation models based on an axisymmetric case	33
2.10	Correlation between inferred FTE and observed SW speed	34
2.11	Examples of prediction made by different extrapolation methods.	36
3.1	MDI synoptic maps of the radial field view from the poles	40
3.2	Illustration of the new polar field correction scheme	43
3.3	Comparison of four polar field extrapolation methods	45
3.4	Statistical metrics for WSA solar wind speed and IMF polarity prediction	48
3.5	Comparison of derived open field foot-points in high-latitude with different input . .	49
3.6	Solar wind speed maps from daily MHD simulation with different input	50
4.1	Examples of global modeling and observation for minimum and maximum phase . .	54

4.2	Modeled global SW speed distribution, SW source regions, and HCS	56
4.3	Modeling and observation of the Sun's secular evolution from 1996 to 2010	57
4.4	Bartel chart of SW speed and IMF polarity prediction and observation at L1	59
4.5	Large scale solar field from 1976 to 2008 based on WSO data	61
4.6	A comparison of the photospheric field and IMF strength for two minima	62
4.7	Modeled coronal structure of CR2069 with different dipole component	62
4.8	Optimal source surface height in terms of total open flux	64
4.9	Optimal source surface height in terms of SWS and IMF polarity prediction	65
4.10	Optimal source surface height in terms of HCS shape and IMF polarity prediction	66
5.1	Observations and modeling results for AR 11158	70
5.2	Close-up view of the core field structure of AR 11158	71
5.3	Five snapshots of the evolving AR11158	75
5.4	Evolution of magnetic energy and related quantities of AR 11158	77
5.5	Three snapshots of a flux emergence site	79
5.6	Estimation of flare energy release	79
5.7	Rapid field changes at the photosphere and in the corona during the 2011 February 15 X-class flare	82
5.8	Difference images of pre- and post-flare magnetic field	83
5.9	Close-up view of the pre- and post-flare vector field in the AR core region	83
5.10	Observed EUV coronal loop retractions	85
5.11	Altitude profile for extrapolated field around the time of the X-class flare	86
5.12	Schematic illustration of the field connectivity as possible results from reconnection	87
6.1	Full-disk AIA 171 Å image showing the non-radial eruption	95
6.2	Geometry of the non-radial eruption	96
6.3	A snapshot of magnetic field of AR 11158 before the eruption	98
6.4	Evolution of the entire AR and the region of interest	99
6.5	Magnetic topology based on NLFFF extrapolation	100
6.6	Various flare emission observations during the non-radial eruption	101
6.7	Schematic illustration of the possible scenario for eruption	105
B.1	Illustration of topological structures	119

Chapter 1

Introduction

1.1 Sun, Solar Magnetic Field, Space Weather

Our Sun is a typical main sequence G-type star with well-measured radius ($R_{\odot} = 6.96 \times 10^8$ m), mass ($m_{\odot} = 1.99 \times 10^{30}$ kg), and luminosity ($L_{\odot} = 3.85 \times 10^{26}$ W). Its $\sim 5,800$ K surface temperature provides roughly 1.4 kW m^{-2} energy near the Earth, ideal for the existence of liquid water and hence the sustainment of life.

The solar interior can be divided into three layers: the core, the radiation zone, and the convection zone. The core extends to about $0.2R_{\odot}$, is extremely hot (~ 15 MK), and hosts the Sun's energy source: the proton-proton chain fusion process. Outside the core, the radiation zone extends to about $0.7R_{\odot}$ where the photons carry the fusion energy upward and encounter continuous scattering along the way. The convection zone resides between $0.7R_{\odot}$ to $1.0R_{\odot}$, where the plasma is convectively unstable and thus forms convection cells. Motions of plasma become the major means of transferring the energy. Shear at the base of the convection zone, coupling with the large-scale motions of the convection zone, namely the differential rotation and the meridional flow, are believed to give rise to the solar magnetic field and its cyclic behaviors through the dynamo effect.

Between the solar interior and atmosphere lies the photosphere at which the plasma turns optically thin. The convective flows below overshoot and forms cell-like structures known as granules and supergranules. Magnetic field concentrations emerge from the convection zone, the largest manifest themselves as sunspots (Figure 1.1(a)) where the field (B) can be as strong as a few thousand kG (kilo Gauss, or 0.1 T). Many absorption lines form in this cool, thin layer; the ones sensitive to magnetic field can be used to probe the solar surface magnetism (see Section 1.2).

The temperature and density continue to drop with height in the next layer, the chromosphere. The temperature falls to a minimum of $\sim 4,500$ K before increases rapidly through a thin layer

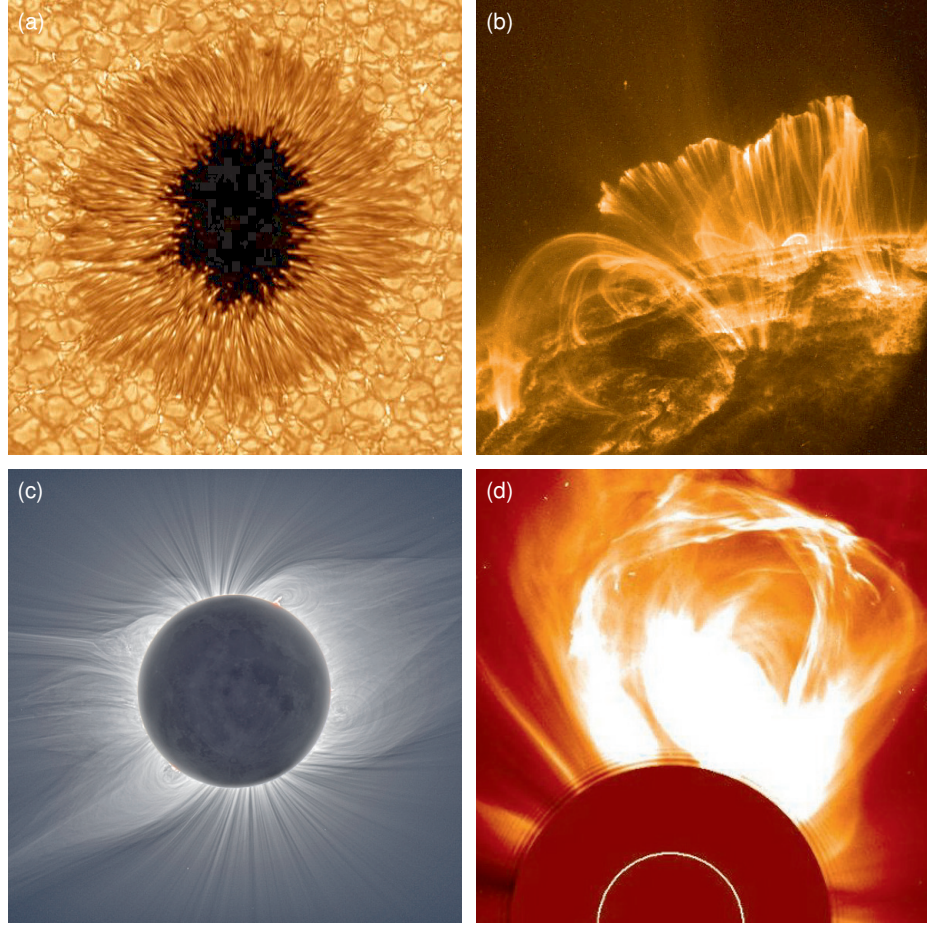


Figure 1.1: Various solar observations illustrating the magnetic structures. (a) Sunspot on the photosphere observed in white light by the *New Solar Telescope*. The dark core is the umbra, with kilo Gauss field that is mostly vertical to the solar surface. The filamentary structure around the umbra is the penumbra, where the field is slightly weaker and more horizontal. The granular structure in the background is clearly visible. Image courtesy *Big Bear Solar Observatory*. (b) Coronal loops observed in extreme ultraviolet (EUV) waveband by *TRACE* satellite showing the million degree corona. Plasma is organized as loops by the magnetic field. Image courtesy NASA and the TRACE team. (c) White light corona observed during the 2008 total eclipse. The plume-like structures on the top (north) and bottom (south) delineate the open field lines. The large cusp-like structures are the streamers. Image courtesy M. Druckmüller. (d) Coronagraph (white light) of a CME taken by the C2 instrument aboard the *Solar and Heliosphere Observatory*, or *SoHO*. The Sun is marked by the white circle. Image courtesy NASA.

called the transition region, and finally reaches several million K in the lower corona, just a couple of megameters (Mm, or 10^6 m) above. The heating mechanism is generally believed to be magnetic, but is still under intense debate. Starting from the chromosphere up to a couple solar radii in the corona, the ratio between the gas pressure (p) and magnetic pressure ($B^2/8\pi$, in cgs unit) is much

smaller than 1, or, plasma $\beta = 8\pi p/B^2 \ll 1$ (e.g. [Gary, 2001](#)). This indicates the dominance of the magnetic field. Owing to the high temperature and low density, the plasma becomes highly ionized and conductive, so the magnetic field is fully coupled with the plasma motion (“frozen-in” effect). The structure of the plasma thus reflects the structure magnetic field, as in the case of the coronal loops (Figure [1.1\(b\)](#)) (e.g. [Aschwanden, 2004](#)).

The Sun’s large-scale magnetic field flips its polarity roughly every 11 years. The strong magnetic field concentrations (e.g. sunspots) in low latitudes undergo the same cycles, and so do the explosive solar activities. During the activity minimum phase, the large-scale field can be approximated by a dipole. Field opens into interplanetary space in the polar region where the plasma is cool and forms the so-called “coronal holes”. Large closed loops form helmet-shaped streamers near the equator (Figure [1.1\(c\)](#)). The hot corona accelerates plasma outward along the open magnetic field, forming the solar wind ([Parker, 1958](#)) whose supersonic speed ranges from about 300 to 800 km s⁻¹. During most of the cycle the solar wind speed is significantly affected by the higher order terms of the magnetic field (see Chapter [4](#)), particularly in the ecliptic. The solar wind blows into the interstellar material and forms a bubble-like structure that we call the heliosphere ([Parker, 1961](#)). Because plasma β increases above 1 again outside a few solar radii, the solar wind plasma travels quasi-radially in the co-rotating frame, dragging the magnetic field along. This forms a spiral-like interplanetary magnetic field (IMF) structure in the rest frame. During the activity maximum phase, the axial dipole becomes weak; active regions (ARs) with strong field in the low latitudes give rise to the more complicated coronal structures; higher order magnetic moments dominate the global field.

The steady solar wind and the IMF constitute the ambient space weather we experience at the Earth. Owing to the Earth’s magnetosphere, most of the energetic particles are deflected with minimal harm done. Nevertheless, energized magnetic fields in the lower corona often exhibit explosive behavior, disturbing the ambient solar wind and IMF. Dissipative processes such as magnetic reconnection (e.g. [Priest and Forbes, 2000](#)) lead to the rapid global relaxation of the field. The released magnetic energy can power flares with rapidly enhanced emission over the spectra from radio to possibly gamma-ray, or coronal mass ejections (CMEs) with millions of tons of plasma thrown out into the heliosphere (Figure [1.1\(d\)](#)). Under certain conditions (e.g. southward IMF), the energized particles can enter the magnetosphere in high latitude regions, creating aurora, inducing strong electric currents that disturb communication, navigation, and power transmission, thus posing threats to flight safety and space missions. These hazardous space weather events are the practical motivation for us to study and try to predict the behavior of the solar magnetic field.

1.2 Observing the Photospheric Magnetic Field

1.2.1 Zeeman Effect and Spectropolarimetry Inversion

The solar photospheric magnetic field is commonly measured using the Zeeman effect. The interaction between the electron magnetic moment and the field splits the atomic energy levels. For a transition between two split energy levels, the spectral line will split correspondingly, and each component will have a distinctive polarization state. The relative wavelength of these polarized components can be used to probe the magnetic field at where the line is formed in the photosphere.

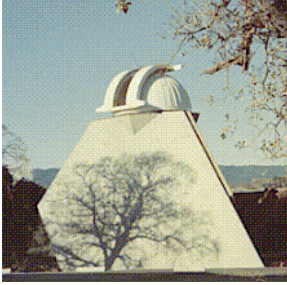
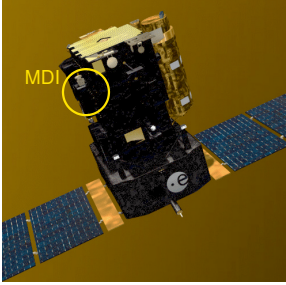
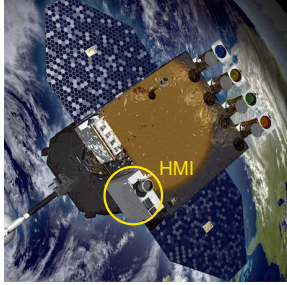
In the presence of magnetic field along the line of sight (LOS) of the observer, the spectral line splits into shifted circular polarized σ components and an unshifted π component. The shift of the wavelength $\Delta\lambda$ is proportional to the LOS field B_l , $\Delta\lambda \propto B_l$. This is the so-called *longitudinal Zeeman effect*. In the presence of magnetic field perpendicular to the LOS (B_t), the shifted components are linearly polarized. This is the *transverse Zeeman effect*.

In practice, the polarized line profiles are described by the Stokes vector (I, Q, U, V) . The Stokes $I(\lambda)$ profile represents the intensity as a function of wavelength λ ; Stokes $Q(\lambda)$ the intensity difference between vertical and horizontal linear polarization; Stokes $U(\lambda)$ the intensity difference between linear polarization at $+45^\circ$ and -45° ; while Stokes $V(\lambda)$ the intensity difference between right- and left-handed circular polarization.

Both B_l and B_t can be estimated directly from the Stokes profiles when the field is weak (see, e.g. [Stenflo, 1994](#)). However, when field becomes strong, the simple scaling no longer holds, and a *spectropolarimetry inversion* method is needed to retrieve the 3D magnetic field information. This method is essentially a fitting scheme that infers the likely magnetic and thermal dynamic parameters that give rise to the observed Stokes profile through radiation transfer calculations. It generally requires detailed knowledge of the line formation mechanism and an appropriate atmospheric model (e.g. [Borrero, 2004](#)).

The linear polarization signal (Q, U) is generally one order of magnitude weaker than the circular polarization (V). The detection limit of B_t is generally on the order of 100 G (strictly speaking, the derived magnetic signal takes the meaning of averaged flux density rather than field strength; its proper unit in cgs convention is thus Mx cm^{-2}) for current instruments, compared to ~ 10 G for B_l . There is also an intrinsic 180° ambiguity in the azimuth direction of B_t (e.g. [Harvey, 1969](#)), which may be resolved under certain assumptions. A brief description of the inversion and azimuthal disambiguation algorithm can be found in [Section 1.2.4](#).

Table 1.1: Three generations of solar telescopes at Stanford

Specs	WSO	MDI	HMI
			
Observatory		<i>SoHO</i>	<i>SDO</i>
Launched	Since May 1975	Since Dec 1995	Since Feb 2010
Location	Palo Alto, CA	L1 point	Geosynchronous
Spectral line	Fe I 5250/5247 Å	Ni I 6768 Å	Fe I 6173 Å
Magnetic data	LOS magnetogram and solar mean field	LOS magnetogram	LOS and vector magne- togram
Resolution	3'	4'' (2'' pixel) ^b	1'' (0.5'' pixel)
Cadence	Daily	96-minute ^a	45- and 720-s ^b

^a Higher resolution and cadence data are available in campaign mode at 1-minute and 0.6''.

^b There are two cameras on HMI. One is devoted to line-of-sight (LOS) observations with 45-s cadence. The other is devoted to vector (spectropolarimetry) observations, but also produces similar LOS data. It takes 135-s cadence filtergram set, which are then averaged to a 720-s cadence before being processed to magnetograms.

1.2.2 Three Generations of Solar Telescopes at Stanford

Over the past four decades, the Stanford solar group has successfully led the effort of designing, building, and operating three generation of solar telescopes that advanced our knowledge in solar oscillation and magnetism. They are: 1) the Wilcox Solar Observatory (WSO; Scherrer *et al.*, 1977); 2) the Michelson Doppler Imager (MDI; Scherrer *et al.*, 1995) at Stanford; 3) the Helioseismic and Magnetic Imager (HMI; Schou *et al.*, 2012). The MDI telescope is aboard the Solar and Heliospheric Observatory (*SoHO*), which is a joint mission between the European Space Agency (ESA) and the National Aeronautics and Space Administration (NASA). The HMI telescope is aboard the Solar Dynamic Observatory (*SDO*), which is the first mission in the Living with a Star (LWS) program from NASA.

Some basic facts of these telescopes are summarized in Table 1.1. They provide the photospheric

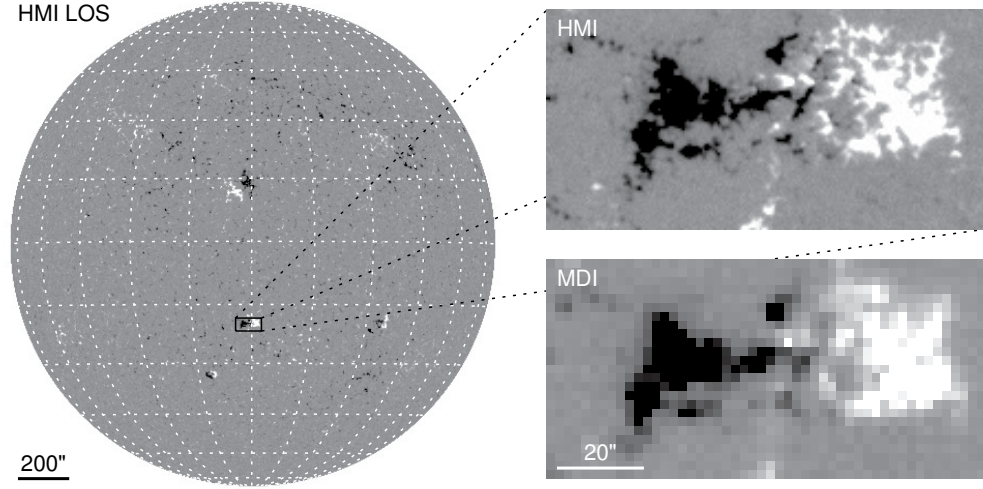


Figure 1.2: LOS magnetograms taken by HMI and MDI on 2010.06.01 at 08:03 UT. (a) HMI full disk magnetogram scaled between ± 100 G. (b) Zoomed in view of AR 11076. (c) Same as (b), taken by MDI and scaled by a factor of $1/1.4$. Both (b) and (c) are shown with a scale between ± 200 G.

magnetic data used in this dissertation, which span over three solar activity cycles. We introduce their relevant data products in the following chapters when appropriate.

1.2.3 Constructing Line-of-Sight Magnetic Maps

A magnetogram is a map of the magnetic field distribution on the solar disk (on the photosphere). All three Stanford observatories generate LOS magnetogram regularly (Figure 1.2 and Table 1.1). WSO produces one or two magnetograms daily with $3'$ resolution, weather permitting. The MDI instrument provides 96-minute cadence observations (15 frames daily), with $2''$ pixels ($4''$ resolution), and a ~ 20 G noise. Higher cadence and resolution data are available for campaign mode. The HMI magnetogram has a cadence of 45 s (720s average also available), pixel size of $0.5''$ ($1''$ resolution), and a noise level around 10 G. The reported field values from different observatories can differ owing to different spectral lines, instrumentation types, data reduction schemes, etc. The values between MDI and HMI magnetograms have an empirical scaling factor $B_l^{\text{MDI}}/B_l^{\text{HMI}}$ of about 1.4 (Liu *et al.*, 2012).

For global-scale studies, it is desirable to have full-sun magnetic maps. We utilize the solar rotation, which has a synoptic period of roughly 27 days, to overcome the lack of far-side observation. Assuming the large-scale field does not change drastically over one solar rotation, we may approximate the full-sun map by a mosaic using magnetograms taken during this period.

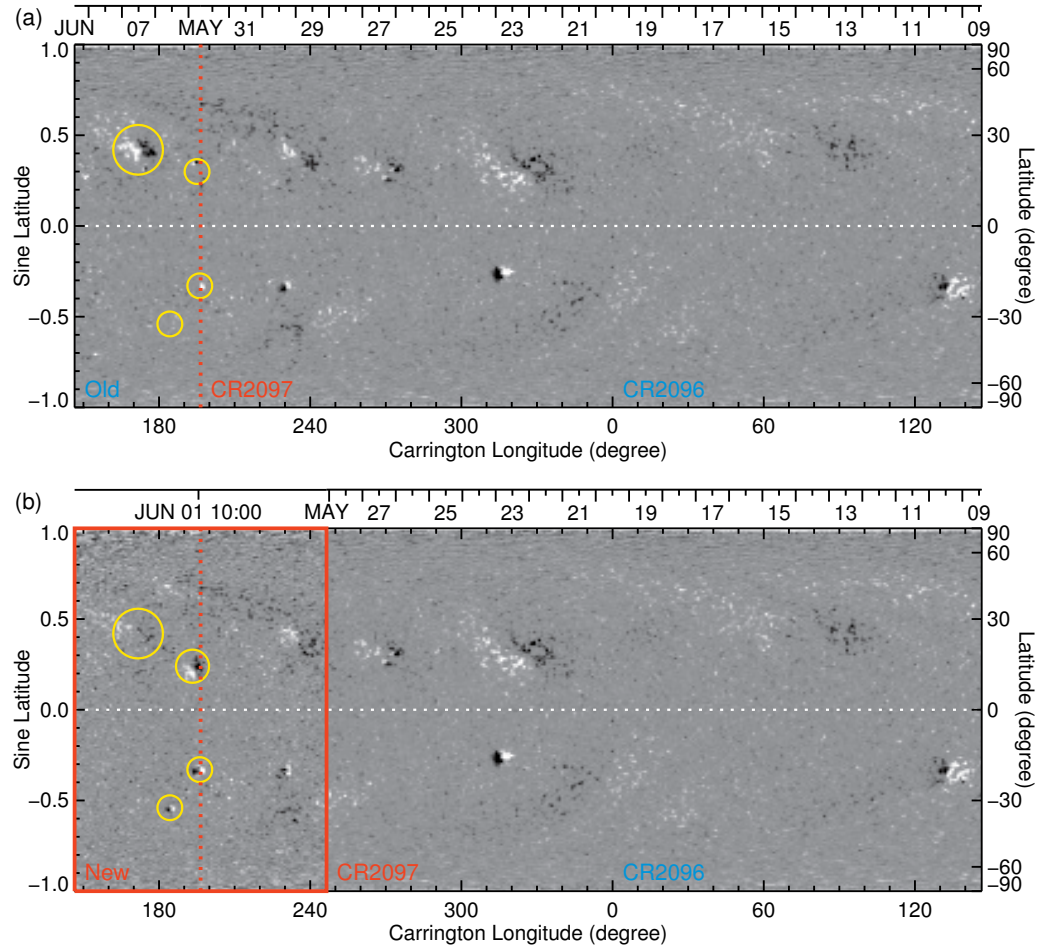


Figure 1.3: (a) A regular synoptic map of MDI radial magnetic field. The longitude spans from CR2097 196.5° (2010 June 01) to CR2096 196.5° (2010 May 09). To better compare with the updated version below, the part between 146.5° and 196.5° of CR2096 is rotated to the left edge. The dates marked above the map indicate the central meridian (CM) passage time. (b) An updated MDI synoptic map. The part enclosed by the red rectangle is from the remapped magnetogram taken at 2010 June 01 10:00 UT. The CM longitude is 196.5° . Data within a 100° longitudinal window are updated from one magnetogram. Compared with the data taken over 20 days ago (region to the left of the vertical red dashed line in the upper panel), field in some ARs has changed significantly. Some decays away, more emerges. The most significant changes are denoted by yellow circles.

To create a commonly used “synoptic map”, a series of LOS measurements are de-projected to the radial direction (Harvey and Worden, 1998; Wang and Sheeley, 1992), corrected for the viewing angle with regard to the solar equator (the solar b angle), and mapped into the Carrington heliographic coordinate accounting for the differential rotation (Zhao, Hoeksema, and Scherrer, 1999; Meunier, 2005). For each pixel in the MDI map, about 20 individual measurements that are registered to

the same Carrington coordinate system are averaged from different magnetograms. The routine MDI synoptic map has a dimension of 3600×1080 (longitude and sine latitude), equivalent to a 0.1° (longitude and latitude) resolution near the equator. The new HMI synoptic map has a size of 3600×1440 . One such map is produced for each Carrington rotation (CR; about 27.28 days). Data included in the final map are generally observed within 10° of the central meridian (CM).

The synoptic map is generally a good proxy for the full-Sun snapshot. Nevertheless, the coronal structure can change substantially within one CR owing to fast evolving ARs (Zhao, Hoeksema, and Scherrer, 1999). For time-sensitive purpose such as space weather prediction, new surface field condition should be incorporated timely to reflect these changes. As one scheme, we may construct a series of “timely-updated” synoptic frames (e.g. Zhao, Hoeksema, and Scherrer, 1999): the newly obtained magnetograms are integrated into the existing synoptic map whenever needed. As illustrated in Figure 1.3, the CM of the remapped new magnetogram is placed at its corresponding Carrington longitude. Data within 50° longitude of the CM on each side are replenished by the new observation in this scheme. This approach is especially effective to account for the new flux that just rotates to the front side (see Chapter 2), and has been shown to improve the solar wind parameter prediction accuracy (Arge and Pizzo, 2000). They are now provided by the HMI pipeline on a daily basis.

The inclination of the Sun’s rotation axis with regard to the normal of the ecliptic is 7.25° . The north (south) pole is not observable during intervals around March (September) when it tilts away from the Earth. Consequently, missing data appear in the synoptic maps in the north (south) polar region. Although the polar region accounts for only a small fraction of the solar surface (just 3.4% above 75° latitude), its field strength proves to be crucial to large-scale modeling efforts (e.g. Arge and Pizzo, 2000; Luhmann *et al.*, 2009) because the field has a dominant polarity. We have developed a new interpolation method to fill in the polar field in a consistent way (Sun *et al.*, 2011), which improves the modeling results. The method has been applied to the MDI synoptic maps, and will be available for HMI as well. We describe this method in Chapter 3.

One of the primary scientific objectives of HMI is to study the evolution of ARs with its high cadence, continuous time coverage, and good spatial resolution. Its unique ability to regularly measure full-disk photospheric vector magnetic field from space makes it particularly suitable for the task. The HMI team developed an algorithm for automatic AR identification based on earlier works with the MDI data set (Turmon *et al.*, 2010), in which we spatially group the magnetic activity from the LOS magnetograms into objects on the scale of active regions, and track these objects from

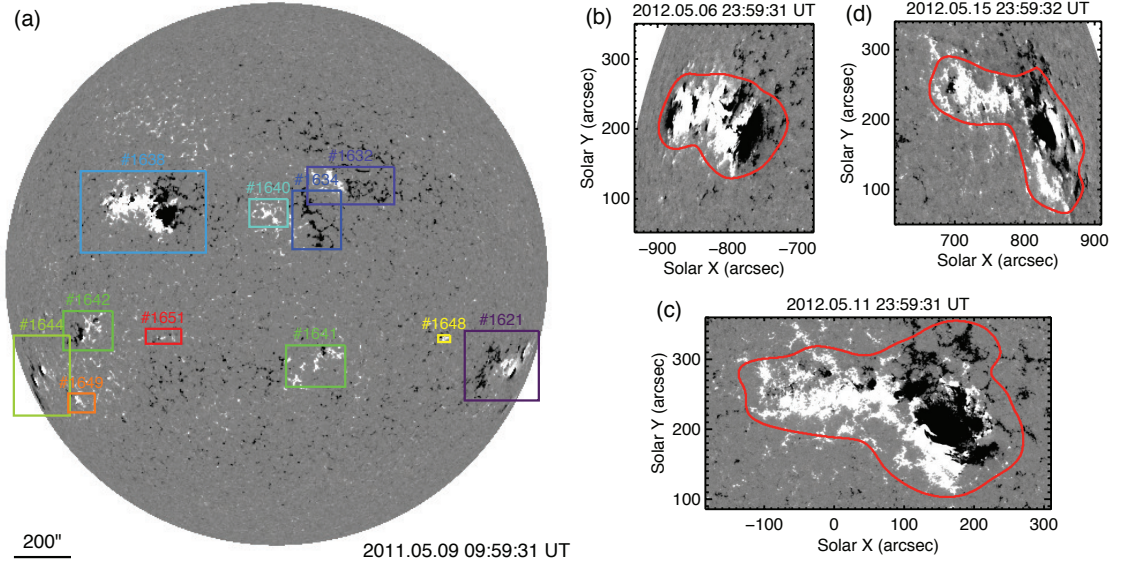


Figure 1.4: Example of automatically identified HMI active region patches (HARPs). (a) All HARPs on disk for 2011.05.09 10:00 UT. Boxed regions are identified ARs with HARP number (analog to NOAA AR number) marked above them. The rectangles enclose the maximum longitude and latitude extent reached during the ARs’ entire disk passages. (b)-(d) Examples of HARP number 1638 (NOAA AR 11476) near east limb, central meridian, and west limb. The red contours encircle the identified “active pixels” within the rectangles at that time.

image to image. The data product is named HMI Active Region Patch (HARP). For detailed documentation on the data product, see <http://jsoc.stanford.edu/jsocwiki/HARPDaDataSeries>. The tracking process synthesizes the AR’s entire disk transit information, thus provides a consistent measure of the AR’s evolution history on the visible solar disk. The geometry information can then be used to extract the regions where we can study the vector field in better detail (see Section 1.2.4). Figure 1.4 shows an example of the identification result.

1.2.4 Constructing Vector Magnetic Maps

The HMI instrument measures the Stokes vector (I, Q, U, V) at 6 wavelengths across the Fe I absorption line at 6173 Å. A new inversion code optimized for HMI, Very Fast Inversion of the Stokes Vector (VFISV; Borrero *et al.*, 2011), is used to retrieve vector magnetic field information from these spectropolarimetric observations. Assuming a Milne-Eddington solution to the radiative transfer equation (Landolfi and Landi Degl’Innocenti, 1982), VFISV utilizes the traditional iterative non-linear least-squares fitting algorithms to speed up the inversion process. The inversion results include

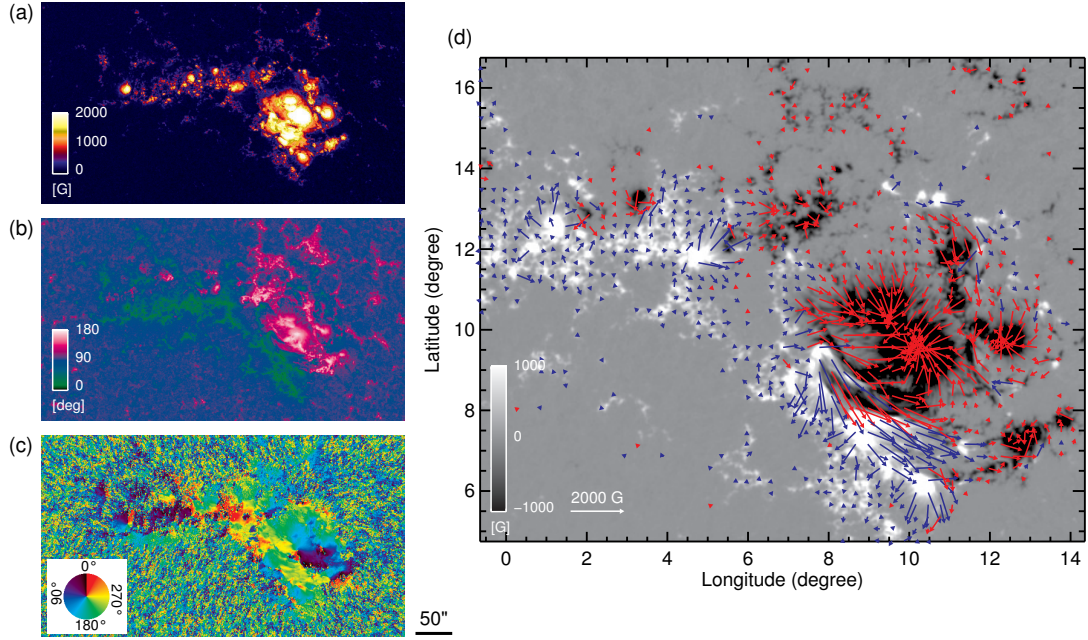


Figure 1.5: Vector magnetic maps for HARP 1638 taken at 2012.05.11 23:59:31 UT (c.f. Figure 1.4(c)). (a) Field strength. (b) Inclination, defined as 0° when pointing toward the observer, 180° when away. (c) Azimuth after with 180-degree ambiguity removed, defined as 0° pointing *up* on the HMI CCD and increasing counterclockwise. Panels (a)-(c) are presented in the observed coordinate. (d) Plate-Carrée projected vector map. The background grayscale image illustrates the radial field. The blue/red arrows denote horizontal field with positive/negative radial counter part. Their length shows the horizontal field strength; their direction shows the azimuth. Arrows are not drawn for weak field regions (field strength below 150 G).

full disk maps of field strength (B), inclination (γ), azimuth (α), a set of thermodynamic parameters (e.g. Doppler width), their estimated uncertainties and mutual correlation coefficients, etc. An example set of the magnetic maps of an automatically identified AR (HARP 1638, c.f. Figure 1.4) is shown in Figure 1.5.

The azimuth value of the transverse field suffers from a well-known 180-degree ambiguity inherent to the linear polarization (Harvey, 1969). Various algorithms have been proposed to address this problem (for review, see Metcalf *et al.*, 2006). For the HMI pipeline, we implemented an improved version of the “minimum energy” algorithm (Metcalf, 1994; Leka *et al.*, 2009), where the weighted combination of vertical current ($|J_z|$) and field divergence ($|\nabla \cdot \mathbf{B}|$) is minimized by the chosen azimuth permutation, for the region of interest. An extended set of recently observed HMI fields are used to estimate the noise level of the current observation. Such estimate is applied in the format of a full disk mask. In the strong field regions where the field strength is above the mask threshold, a simulated annealing algorithm is used. In the weak field regions where the measurements are

less reliable, the solutions from simulated annealing are smoothed with a neighboring acute angle algorithm (Leka *et al.*, 2009). To speed up the algorithm, the ambiguity in the weak field can be optionally resolved with simpler methods, such as potential-acute, radial-acute, or randomization.

Two types of format are involved in each representation of the vector magnetograms. The first refers to the location on the Sun where a measurement is made; the second refers to the decomposition of the field vector obtained at that point. We may call the conversion from one format to another “remapping” in the first case; “vector transformation” in the second. The “as-is” HMI vector data are represented in the native coordinate (as captured by the camera), with images of B , γ , and α . We have developed a module that performs various types of remapping and vector transformation (see Figure 1.5(d)). The module includes various map projection methods for remapping (Calabretta and Greisen, 2002; Thompson, 2006); the vectors can be optionally transformed to a local Cartesian coordinate (e.g. Gary and Hagyard, 1990). Oversampling and binning are applied to reduce aliasing.

1.3 Modeling the Coronal Magnetic Field

1.3.1 The Quasi-Static, Force-Free Coronal Field

The coronal magnetic field is much weaker than that of the photosphere; its polarization is harder to measure. It is therefore of practical interest to infer them from the photospheric observations. Generally speaking, the highly ionized solar coronal plasma can be described by magnetohydrodynamics (MHD) equations.

In particular, the governing MHD equation for the momentum conservation is:

$$\rho \left(\frac{\partial \mathbf{v}}{\partial t} + (\mathbf{v} \cdot \nabla) \cdot \mathbf{v} \right) = \mathbf{j} \times \mathbf{B} - \nabla p + \rho \mathbf{g}, \quad (1.1)$$

where ρ denotes density, \mathbf{v} velocity, \mathbf{j} current, \mathbf{B} magnetic field, p gas pressure, and \mathbf{g} solar gravity field. In the low corona (below a few hundred megameters), the Lorentz force dominates the other forces (Gary, 2001). The parameter plasma β , which describes the relative importance of gas pressure and magnetic pressure, satisfies

$$\beta = 8\pi p / B^2 \ll 1. \quad (1.2)$$

If the field is quasi-static, then the left side of Equation 1.1 vanishes. Then Lorentz force must balance itself, i.e. it satisfy the the “force-free condition”

$$\mathbf{j} \times \mathbf{B} = 0. \quad (1.3)$$

Note that Ampere's Law under the MHD approximation states

$$\mathbf{J} = \frac{4\pi}{c}(\nabla \times \mathbf{B}). \quad (1.4)$$

We then have

$$(\nabla \times \mathbf{B}) \times \mathbf{B} = 0, \quad (1.5)$$

which means the current must align (parallel or anti-parallel) with the field. This and the divergence free criteria

$$\nabla \cdot \mathbf{B} = 0 \quad (1.6)$$

describe the force-free magnetic field.

Equation 1.5 is equivalent to

$$\nabla \times \mathbf{B} = \alpha \mathbf{B}, \quad (1.7)$$

where α is called the torsional parameter and can be any scalar field. Taking the gradient of Equation 1.7 on both sides and consider Equation 1.6, we have

$$\mathbf{B} \cdot \nabla \alpha = 0. \quad (1.8)$$

This indicates that α must be constant along each individual magnetic field line.

The quiescent coronal field generally responds to the change of the photosphere in a quasi-static way. Due to the large density contrast, the time scales of the dynamic processes in the photosphere (characterized by the Alfvén time scale, $t_A = L/v_A = L\sqrt{4\pi\rho}/B$, where L is the system's length scale, $v_A = B/\sqrt{4\pi\rho}$ is the Alfvén speed) is one or two magnitudes greater compared to the corona. This leaves the coronal field enough time to relax, making the quasi-static assumption a good approximation in general. The assumption, of course, does not apply to the explosive events such as flares and CMEs, where the coronal field reorganizes in within (as little as) a few minutes. In addition, vector field measurements at different heights have shown that the field indeed becomes force-free a few hundred kilometers above an AR (Metcalf *et al.*, 1995). Years of force-free extrapolation (mostly current-free, or potential) have demonstrated reasonably good agreement between the modeled and the observed large-scale field. These observational and empirical evidences validate the force-free assumption. Nevertheless challenges remain, especially for the more realistic and sophisticated models (e.g. Schrijver *et al.*, 2008; DeRosa *et al.*, 2009). More about various methods are presented in the next sections.

1.3.2 Potential Field Extrapolation

For the simplest case where the field is current-free, the field assumes the lowest energy state, known as the potential field. It satisfies:

$$\nabla \times \mathbf{B} = 0. \quad (1.9)$$

Such field may be expressed by a scalar potential Ψ : Ψ :

$$\mathbf{B} = -\nabla \Psi. \quad (1.10)$$

Consider the divergence free condition, we have a Laplace boundary problem

$$\nabla^2 \Psi = 0, \quad (1.11)$$

for the volume (lower corona) that we are interested in. The lower boundary is often taken to be the observed photospheric field.

In a semi-infinite space with the normal field component (B_n) specified on the boundary (∂_n), the potential field can be obtained using a Greens function method (for review, see [Sakurai, 1989](#), and references therein). The method is often used to model the AR field: the lower boundary can be approximated by a plane, and the problem is solved for a finite region using Cartesian coordinate. Ideally speaking, the region should be isolated, with little magnetic flux across the side and upper boundary. The Fourier expansion method can also be used for such purpose.

For global-scale modeling, the widely used model is the potential field source surface (PFSS) model ([Schatten, Wilcox, and Ness, 1969](#); [Altschuler and Newkirk, 1969](#)). The photospheric observation, such as the synoptic map, is used as the inner boundary at $r = R_\odot$ in heliocentric spherical coordinate, where R_\odot denotes the solar radius. It is common to use only the inferred radial component of the observed photospheric field ([Wang and Sheeley, 1992](#))

$$\nabla \Psi \cdot \hat{\mathbf{r}} \Big|_{r=R_\odot} = -B_r \Big|_{r=R_\odot}, \quad (1.12)$$

where $\hat{\mathbf{r}}$ is the unit radial vector, and B_r the radial field. The outer boundary is set on a sphere known as the “source surface”, $r = R_s$, where the field is required to be radial.

$$\nabla \Psi \times \hat{\mathbf{r}} \Big|_{r=R_s} = 0. \quad (1.13)$$

The source surface is commonly set at $2.5R_{\odot}$ (Hoeksema, 1984), but can be treated as a free parameter in special cases to fit the observed coronal structures (Lee *et al.*, 2011).

Equations 1.11-1.13 can be numerically solved using the spherical harmonic expansion method. A detailed description of the mathematical schemes can be found in Appendix A.

The PFSS model has been shown to provide good description of the large scale coronal field. It is qualitatively comparable with full MHD solutions (e.g. Riley *et al.*, 2006), while being much easier to implement and faster to execute. On the other hand, some of its drawbacks include: it cannot provide information on flow, thermodynamic parameters, etc.; it does not prescribe field beyond the source surface; it is unable to describe the non-potential active region field; and the amount of magnetic flux with open configuration is generally too small.

A variety of PFSS-like models have been introduced to better fit certain observational features. Some adopted sheet-like currents at the zero-radial-field isosurface in the otherwise potential field solution above a certain height (e.g. Schatten, 1971), or additional volume-filling currents that satisfy the magnetohydrostatic equations (e.g. Wolfson, 1985; Wang and Sheeley, 1988; Zhao and Hoeksema, 1995). These models, along with the PFSS model, may be used to infer a variety of magnetic and non-magnetic coronal features. The algorithms are described in Chapter A. The results will be discussed in Chapters 2 and 4.

1.3.3 Force-Free Field Extrapolation

The ARs, with kilogauss field in the sunspots, are generally not potential, especially during their emerging phase (Leka *et al.*, 1996). Under the force-free condition, the field aligned currents render the torsional parameter α non-zero.

The solution to Equations 1.7 and 1.8 (equivalent to Equations 1.5 and 1.6) with a constant, non-zero α is called linear force-free field (LFFF). To obtain a LFFF solution, the constant α is essentially a free parameter for a given boundary condition. The existence and the uniqueness of the solutions are critically dependent on the choice of the boundary condition (for review, see Thalmann, 2010). Moreover, from vector field measurement, α can be directly mapped using the normal component

$$\alpha = \frac{J_n}{B_n} = \frac{\nabla \times \mathbf{B}_t}{B_n}, \quad (1.14)$$

where the subscripts n and t denote the normal and tangential components, respectively. In many cases it varies greatly in space and clearly cannot be approximated by a constant.

A more general approach is called non-linear force-free field (NLFFF), where α varies in space.

A series of algorithms have been proposed and tested, using both analytical data and solar data (a series of recent comparative studies are described in [Schrijver *et al.* \(2006\)](#); [Metcalf *et al.* \(2008\)](#); [Schrijver \(2009\)](#); [DeRosa *et al.* \(2009\)](#)). Amongst the tested, one of the better performing is an “optimization” based algorithm ([Wiegmann, 2004](#)). It seeks to minimize the metrics

$$L = \int_V (w_f |B|^{-2} |(\nabla \times \mathbf{B}) \times \mathbf{B}|^2 + w_d |\nabla \cdot \mathbf{B}|^2) dV \quad (1.15)$$

in the computation domain, where w_f and w_d are empirical weighting functions. The lower boundary is derived from the observed vector field; the side and top boundary are usually taken from the potential field solution, but with a finite boundary layer of small w_f and w_d as to mitigate the boundary’s undesired influence.

This NLFFF algorithm, along with all others, suffer from various drawbacks ([DeRosa *et al.*, 2009](#)). An obvious problem is that the field measured in the photosphere is not force free. Thus the boundary is intrinsically inconsistent with the model’s assumption (not to speak about the uncertainties in measurement). One method to alleviate this discrepancy is to “preprocess” the photospheric magnetogram so that the force-free condition is better satisfied ([Wiegmann, Inhester, and Sakurai, 2006](#)). The procedure slightly alters the horizontal field and performs a certain amount of smoothing by iteratively minimizing the net flux, net Lorentz force, and net Lorentz torque on the boundary. Additional constraints during this step may come from $H\alpha$ observations, where the direction of the chromosphere fibrils outline the horizontal direction of the force-free chromospheric field ([Wiegmann *et al.*, 2008](#)). More discussion on the algorithm can be found in Section 5.4.

1.4 Outline of the Dissertation

This dissertation includes works under various topics that aim at the improvement of understanding solar magnetic field observation, modeling, and prediction. The spatial scale of the topics divide the dissertation into two main parts: Chapters 2, 3, and 4 focus on the global scale field, while Chapters 5 and 6 focus on the local AR field.

Chapter 2 describes the effort to improve space weather forecasting using MDI data. We first introduce the Wang-Sheeley-Argue (WSA) model, linking global magnetic field structure inferred from the MDI synoptic map and PFSS model to the solar wind speed. The empirical function used to make such connection is then optimized using the in-situ solar wind speed and magnetic field polarity measured near the Earth. We assess the accuracy of the model, its relations with the solar

activity cycle phase and specific solar phenomena, as well as places where improvements can be made.

Chapter 3 presents a new polar field interpolation scheme that helps improve the space weather forecasting accuracy. We briefly review the importance and difficulty of correctly estimating the field in the unobservable polar region, as well as various existing interpolation scheme. The new scheme is then described, with its applications to the WSA and MHD simulations as validation.

Chapter 4 presents an archival study on the large scale magnetic field over solar cycle 23. We use the PFSS model and MDI data to delineate the evolution of global dipole field moment, heliospheric current sheet topology, coronal hole size and location, open magnetic flux, global solar wind speed distribution, etc. Their mutual relationships are explored, and the modeling results are compared against various observations. In particular, we look into the recent quiet minimum phase and try to explain the surface magnetic origin of the peculiar coronal and heliospheric features.

Chapter 5 utilizes a series of new vector magnetograms from HMI to study the evolution of field and pertinent energy of the first major eruptive AR of solar cycle 24. We continuously monitor its highly non-potential surface field and use a NLFFF extrapolation to study its evolving 3D field structure in the low corona. For the first time, we are able to map such field and energy distributions continuously for several days with high cadence. The modeled results are corroborated with coronal observations. During a large flare, we find unambiguous evidence that the photospheric magnetic field changes within tens of minutes. We show that this picture is consistent with the conjectured magnetic “implosion” (Hudson, 2000), and the coronal field becomes more compact after the flare.

Chapter 6 further studies a subregion of the same AR where a newly emerged bipole led to a series of homologous, highly non-radial eruptions. Modeling suggests a highly inclined coronal magnetic structure with a distinct coronal null point. The inferred structure is consistent with white light, EUV, soft X-ray (SXR), and hard X-ray (HXR) observations during the eruptions. The inclined field geometry naturally guided the non-radial trajectory of the ejecta.

Finally, we conclude our findings and discuss future work in Chapter 7.

* Along with introduction to the basic facts about the Sun and its magnetic field, some of my works involving the development of the HMI magnetic field data pipeline are described in this chapter: synoptic map polar field interpolation (Section 1.2.3); automatic active region identification (Section 1.2.3); 180-degree azimuthal ambiguity resolution for vector field (Section 1.2.4); vector data remapping and vector coordinate transformation (Section 1.2.4); global potential field extrapolation module (Section 1.3.2); non-linear force-free extrapolation module (Section 1.3.3).

Chapter 2

Improving Space Weather Prediction: Optimizing the Wang-Sheeley-Argge (WSA) Model for MDI Data

2.1 Introduction

The solar wind (SW) originates from open magnetic field structures in the corona and accelerates along open flux tubes ([Parker, 1961](#)). Their major source region, known as coronal holes (CH), have lower density and temperature than the background corona with predominantly unipolar fields. Their shape, size and location vary drastically as the large scale field evolves over an activity cycle. The structure of the solar wind changes accordingly too. For example, the Ulysses missions fast latitudinal scans showed that during the minimum phase, the heliosphere is dominated by fast solar wind flows that originate from polar CHs ([Balogh *et al.*, 1995](#); [Neugebauer *et al.*, 1998](#)) whose speeds appear latitude-independent. During maximum, however, a more variable speed structure was found with slow solar wind coming from smaller low-latitude CHs as well as the edge of ARs ([Neugebauer *et al.*, 2002](#)).

One important aspect of the space weather forecasting is the prediction of the background SW speed. The ambient SW may interact with CMEs to speed up or delay their propagation, thus affecting the arrival times at the Earth. The interaction between the fast and slow SW streams form the corotating interaction regions (CIRs), which generate shocks capable of accelerating energetic particles. When the interplanetary magnetic field (IMF, e.g. magnetic field near the Earth) has a sustained southward component, it may reconnect with the Earth's magnetic field, allowing energetic particles to penetrate deep into the atmosphere which pose serious threats to our power and communication systems.

Although the acceleration mechanism of the SW is not yet fully understood, a correlation between

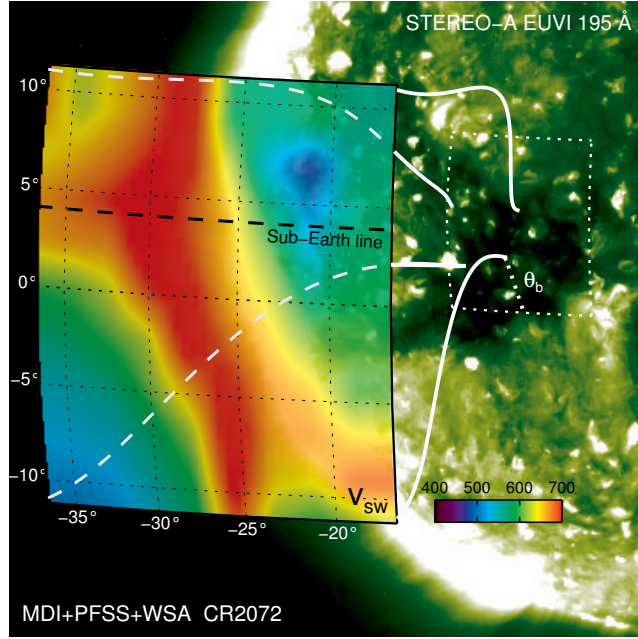


Figure 2.1: Illustration of the WSA model based on calculations for CR2072. The background is a 195 Å EUV image from *STEREO-A* satellite SECCHI EUVI instrument. The dark region near the image center corresponds to an equatorial coronal hole. In the foreground is a $25^\circ \times 20^\circ$ region at the source surface ($R_s = 2.5R_\odot$). A SW speed map inferred from the WSA model is plotted on the surface. Field lines computed from the PFSS model connect the four corners of the region down to the coronal hole, where a super-radial expansion (i.e. $f_s > 1$) is obvious. The other parameter in the WSA model, θ_b as the angular distance of the flux tube footpoint to the edge of the CH, is also shown in the plot schematically. The Earth orbit is projected on to the surface and takes the form of the sub-Earth line. In the model, SW computed on this line maps radially to the Earth.

the coronal field geometry and SW speed has been established over the years. Reasonable success has been achieved in modeling as well. [Levine, Altschuler, and Harvey \(1977\)](#) suggested that the divergence of magnetic flux tubes plays an important role in the acceleration of solar wind. Small flux tube divergence in large CHs corresponds with high speed winds. [Wang and Sheeley \(1990\)](#) used magnetic field synoptic maps and the PFSS model ([Schatten, Wilcox, and Ness, 1969](#); [Altschuler and Newkirk, 1969](#)) to compute the magnetic flux-tube expansion factor (FTE). They found a clear inverse correlation between the FTE and the observed in-ecliptic SW speed.

The concept of the FTE is illustrated in [Figure 2.1](#). For a particular flux tube, FTE (f_s) is defined as

$$f_s = \frac{B_r(R_\odot) R_\odot^2}{B_r(R_s) R_s^2}, \quad (2.1)$$

where $B_r(R_\odot)$ and $B_r(R_s)$ denote the radial field strength at solar surface (R_\odot) and the source surface (R_s), connected by the same flux tube.

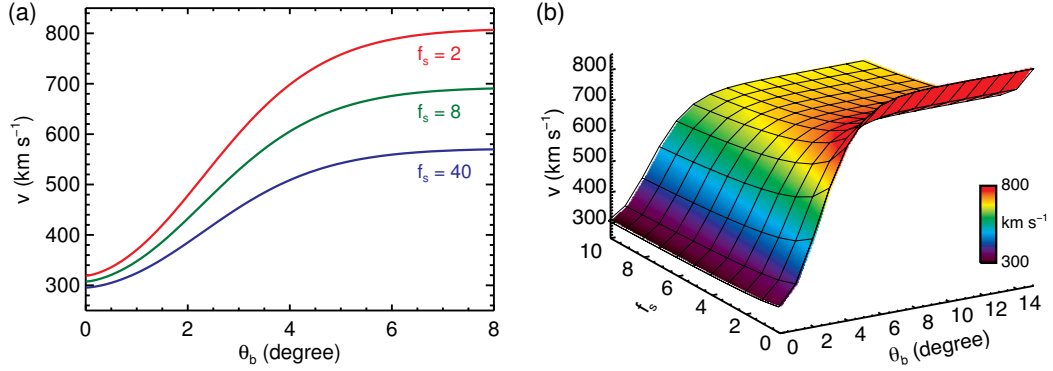


Figure 2.2: Characteristics of the empirical function. (a) SW speed v as a function of θ_b , for $f_s = 2, 8$, and 40 . The function used here is optimized for the MDI data set, but holds the general characteristics of the empirical function itself. For example, for center of the large CHs with θ_b greater than 6° , v is always greater than 500 km s^{-1} regardless of f_s . Small f_s corresponds to higher speed, given the same θ_b . (b) 3D contour of v as a function of θ_b and f_s .

Arge and Pizzo (2000) followed this discovery and developed an empirical function to relate the FTE to the wind speed. A statistically significant correlation (~ 0.4) between the modeled and observed SW speed was obtained over a 3-year period. Arge *et al.* (2004) later adopted a second parameter (θ_b) proposed by Riley *et al.* (2001), which describes the minimum angular separation (at the photosphere) between an open field footpoint and its nearest CH boundary. Flux tubes from the center of large polar CHs have large θ_b and thus will produce higher speed. After kinematically mapping the SW speed forward to near the Earth, one can make prediction of the speed and the IMF polarity (directed toward or away from) at the Earth a few days in advance. This model, known as the Wang-Sheeley-Arge (WSA) model, is now widely used to predict the ambient space weather conditions.

The empirical function from Arge *et al.* (2004) adopts the following form:

$$v = 265 + \frac{1.5}{(1 + f_s)^p} [a - b \exp(1 - (\frac{\theta_b}{\theta_0})^q)]^k (\text{kms}^{-1}), \quad (2.2)$$

where f_s and θ_b are computed from the modeled field, θ_0 is the resolution of the modeled field, p , q , k , a , and b are free coefficients (some constraints may apply, see Section 2.2) that may be fit against observations. Note that the parameters depend on the source of the observed data input. In this function, solar wind is given a higher speed if it is accelerated along a less expanded flux tube (smaller f_s) and originates from deeper in a CH (greater θ_b). Figure 2.2 offers a visualization of the characteristics of the function. The SW speed value is then assigned to the SW speed at a certain

height (source surface, for example).

There are numerous aspects that can affect the prediction. For example, different observatories provide synoptic maps with different spatial resolutions, cadences, and different field values. The measurements in the solar polar regions are generally less reliable due to the viewing angle, but prove important to the extrapolation outcome. Various extrapolation algorithms may yield different coronal field structures. The model used to map the SW speed from near the Sun to near the Earth also affects the result.

Here we retrospectively tune the empirical function for the MDI data with a set of commonly used procedures that we describe below. We seek to optimize the scheme for a large part of the data archive, which spans about 13 years (from July 1996 to July 2009) and covers most of the cycle 23. In a sense, such an approach provides a “conditioned” upper limit of the long term prediction accuracy. We explore the characteristics of the result during different solar cycle phases and link them to certain types of solar phenomena as well.

We describe the procedures in Section 2.2. Results based on PFSS extrapolation, the statistical evaluation, and factors that may effect the prediction accuracy are presented in Section 2.3 and 2.4, respectively. A comparison with other extrapolation methods is discussed in Section 2.5. Section 2.6 summarizes the chapter.

2.2 Optimization of the Scheme

The coronal structure can change substantially within one CR owing to fast evolving ARs (e.g. Schrijver and Title, 2011). For time-sensitive purposes such as space weather prediction, new surface field conditions should be incorporated in a timely way to reflect these changes. For this study, we construct a series of daily-updated synoptic maps: each day the newly obtained magnetograms are integrated into the existing synoptic map. The procedures were described earlier in Section 1.2.3.

We employ a new polar field interpolation method (Sun *et al.*, 2011) to fill the unobserved or poorly observed polar regions. The method utilizes the annual best-observed polar field when it tilts towards the Earth to interpolate the missing pixels and merge them back to the map smoothly; this improves the long-term performance of the model. We describe the method in Chapter 3.

The input maps here are binned to a resolution of $2.5^\circ \times 2.5^\circ$ (longitude and latitude). We compute the PFSS coronal field using the spherical harmonics expansion method (Appendix A), where we truncate the series at $l = 72$. Other extrapolation methods have also been tested and discussed in Section 2.5.

We trace magnetic field lines from a uniform grid from the source surface ($R_s = 2.5R_\odot$) downward to the photosphere. The parameter f_s is then calculated at each grid point using Equation 2.1. The footpoints of these open field lines determine what we define as CHs.

We use the empirical function (Equation 2.2) to determine the SW speed at the source surface. The velocity of the solar wind in the heliosphere is subject to the dynamic processes during its journey outward. In a simplified approach, we assume the plasma propagates radially outward in the co-rotating frame, its speed remains constant except when fast-slow stream interaction occurs. The magnetic field is considered to be simply “dragged” by the plasma due to the frozen-in effect. Hence, the IMF polarity is solely determined by the polarity of the solar wind source region. An ad hoc one-dimensional kinetic model described in (Arge and Pizzo, 2000) is used to model this process to 1 AU.

We sample along the sub-Earth line where the accelerated solar wind directly reaches the Earth and perform the calculation with a resolution of 2.5° . This yields a 27-day time series of SW speed and IMF polarity with a 4.5-h cadence near the Earth (or L1 point). To emulate the operative space weather forecasting, for predictions made from one daily-updated synoptic map, we choose to analyze only the solar wind predicted to arrive between 2.5 and 3.5 days afterwards (3-day advanced prediction) (Owens *et al.*, 2005). The final model output is thus a time series that consists many one-day chunks, and is updated daily. Owing to the varying SW speed and the stream interactions, the L1 time series may not be equally sampled in time. We simply interpolate it into a 4.5-h cadence series. In addition, we compute the SW speed and IMF polarity at 2.5° north and south of the sampled sub-earth point and use those values as an estimate of uncertainty (Arge and Pizzo, 2000). An example of the predicted time series can be found in Figure 2.3.

To determine the best-fit coefficients of the function for the MDI data, we perform a search in the coefficient space. For each time, a set of trial coefficients is chosen, the trial function is used to predict the solar wind at L1 and the result is compared with in situ observation. This procedure can be done repeatedly within a reasonable range until a statistically “best” set is found. We constrain the coefficient set (a, b, p, q, k) in Equation 2.2 such that the lowest possible value is 265 km s^{-1} , the highest about 800 km s^{-1} , consistent with the observation. Four common statistical metrics are evaluated: 1) root mean square errors (RMSE) of speed; 2) mean absolute percentage error (MAPE) of predicted speed v_p compared to observation v_o : $\langle |v_p - v_o|/v_o \rangle$; 3) Pearson correlation coefficient (CC) between predicted and observed speed time series; 4) the success rate of IMF polarity prediction (PIMF). We note that a variety of coefficient combinations may have similar statistical

performance. In this case, we evaluate the detailed speed predictions for 9 random selected high-speed streams ($v > 600 \text{ km s}^{-1}$). A single set of coefficients is finally selected based on these 9 cases. The optimization process is statistically based, largely objective, and the fit is based on result of over a solar cycle. It essentially gives an estimate of the upper limit of the model’s statistical performance under the current scheme (see Section 2.4 for a discussion of its implications).

The OMNI data set (King and Papitashvili, 2005) provides the solar wind bulk speed and the IMF polarity at the L1 point. During the fit, we exclude the observations at times when the protons have extra low temperature (i.e. the measured proton temperature T_p and the expected temperature from normal solar wind expansion T_{ex} satisfy $T_p/T_{ex} \leq 0.5$) to reduce the effect of transient ejecta. These observations are included during the final statistical evaluation (Richardson and Cane, 1995).

2.3 MDI Solar Wind Velocity Prediction Result

2.3.1 Example Prediction

Figure 2.3 shows an example of the result. Panel (a) shows the input of the model, a daily-updated synoptic map (updated on 1996.08.27, mapped back to the solar surface), where the front side data between the red dashed lines reflect the most recent observation. A region of predominantly positive magnetic polarity appears near the ecliptic. It corresponds to a large extension of the northern polar CH, as shown in panel (b). Such large CH is usually the birth place of fast SW streams. As expected, the PFSS extrapolation indicates open magnetic field configuration in this region, as shown in panel (d). Its relatively large size and associated small flux tube expansion yield a fast SW stream, indicated by the arrow in panel (c).

SW streams computed along the sub-Earth line (pink lines in Figure 2.3) traverse the ecliptic and reach the Earth. The 3-day advanced prediction, made using data from Aug 27, include a warning of the aforementioned fast stream that is indeed measured on the 30th in situ at the L1 point. The predicted speed time series is shown in Figure 2.3(e).

The large scale coronal field at the source surface is dominated by the dipole component with a strong quadrupole warp. The polarity inversion line (PIL) is shown in Figure 2.3 as a yellow curve. North of the PIL, the field is positive. The sub-Earth line traverses the PIL from west to east as the Sun rotates, moving from the north of the PIL to the south. Therefore, the polarity of IMF near the Earth is expected to switch. In the more commonly used Geocentric Solar Ecliptic (GSE) coordinate, the IMF polarity switches from negative (“towards” the Earth) to positive (“away” from the Earth), as shown in Figure 2.3(f) (opposite to the heliocentric convention).

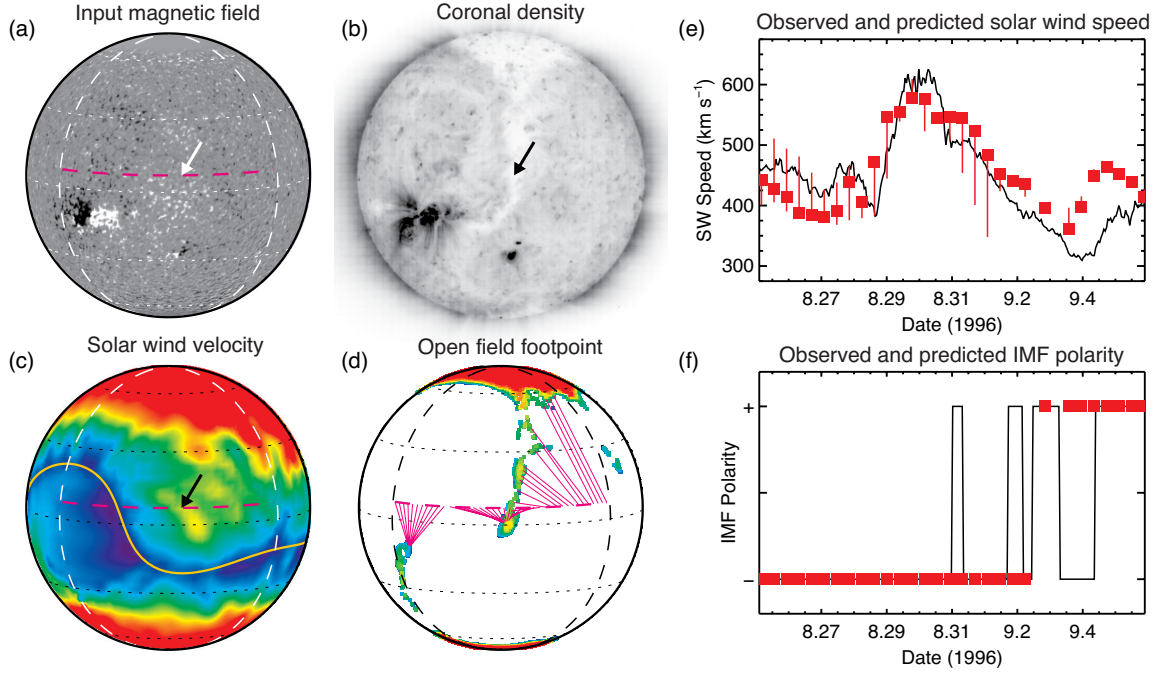


Figure 2.3: Example of the WSA model results: input, output, and observation. (a) Near side of the daily-updated MDI magnetogram for 1996.08.27 around noon. The two dashed lines at $\pm 50^\circ$ longitude bracket the part that has been updated. The dotted lines are latitudes at 0° , $\pm 30^\circ$, and $\pm 60^\circ$. The pink dashed line is the sub-Earth line (projected trajectory of the Earth). The arrow indicates the approximate region from which the 3-day advanced prediction is made. The field is predominantly unipolar close-by. (b) Negative EUV image at 195 \AA band from the EIT telescope on board *SOHO*. The famous “elephant trunk” (c.f. Zhao, Hoeksema, and Scherrer, 1999) coronal hole extends from the north polar region to equator which appears bright here. It is the source of the high speed SW stream. (c) WSA predicted SW speed at the source surface ($2.5R_{\odot}$). Red color shows speed above 650 km s^{-1} , blue about 300 km s^{-1} . The yellow curve is the polarity inversion line (PIL) of radial field. IMF above the curve is pointing away from the Sun. The arrow indicates the high speed SW stream that reaches the Earth. (d) Open field line footpoints at R_{\odot} indicating the source locations of the SW. They are colored according the speed of SW assigned by the WSA model. The pink solid lines connect the sampled sub-Earth points to their source regions on the solar surface. (e) Observed SW speed at L1 point and 3-day advanced prediction. The black line is the hourly averaged SW bulk speed obtained from the OMNI data set. The red squares show the prediction, binned to a 9 hr resolution. The high speed stream on the 30th originates from the CH near disk center on the 27th. (f) Observed IMF polarity at L1 point and prediction. The polarity is positive when the field is pointing from the Earth to the Sun.

This example demonstrates the data product we are able to make, near real time, for ambient space weather prediction. It is also an example of the typical coronal field and solar wind conditions during the minimum activity phase. The polar regions host mostly unipolar field which assumes an open configuration, and act as the primary source of fast SW that dominate the heliosphere (e.g. Balogh *et al.*, 1995). A detailed description of these characteristics for different phases of Cycle 23

Table 2.1: Optimized coefficients in WSA empirical function (Equation 2.2) for different extrapolation methods and their prediction accuracy. The PFCS and CS methods are described in Section 2.5

Model	p	q	k	a	b	RMSE (km s ⁻¹)	MAPE	CC	P _{IMF} (%)
PFSS	0.22	1.5	3.4	6.08	1.21	96.8	0.159	0.470	81.2
PFCS	0.25	1.5	3.4	6.11	1.29	98.9	0.160	0.476	80.9
CS	0.27	1.5	3.4	6.14	1.40	107.8	0.176	0.333	80.2

Table 2.2: Statistical evaluation of in-ecliptic SW speed and IMF polarity prediction at L1 point

	Interval	Activity Phase	RMSE (km s ⁻¹)	MAPE	CC	P _{IMF} (%)
Overall	07/1996-07/2009		96.8	0.159	0.470	81.2
I	07/1996-06/1998	Minimum	71.4	0.137	0.448	76.4
II	06/1998-01/2002	Maximum	101.1	0.161	0.282	78.3
III	01/2002-01/2007	Declining	106.1	0.167	0.463	85.1
IV	01/2007-07/2009	Minimum	89.3	0.159	0.584	80.4

will be presented in Chapter 4.

2.3.2 Statistical Evaluation

We list the optimized coefficient set in the first row of Table 2.1 and use the updated empirical function to predict the a 3-day advanced space weather indices. The 12-year-long, 4.5-hour time series of in-ecliptic SW speed and IMF polarity is statistically compared against the OMNI data set on a point-by-point basis. The hourly OMNI speed series is averaged to the same time resolution by using a 4.5-hour window centered at the time each prediction is made. The hourly OMNI IMF data is reduced according to the counts of each polarity of B_x (in GSE coordinate) within the 4.5-hour window. If 3 or more hourly B_x values have the same polarity, that polarity is assigned to the entire 4.5-hour interval; otherwise the interval is of mixed polarity. Data points with mixed polarity are not included in evaluation.

The overall statistical performance of the WSA model is shown in the first row of Table 2.2. During solar cycle 23, the model exhibits an overall root mean square error (RMSE) of 96.8 km s⁻¹.

Table 2.3: Prediction accuracy for different SW speed ranges

Speed Range ^a (km s ⁻¹)	RMSE (km s ⁻¹)	MAPE	CC	PIMF (%)	Occurrence (%)
$v < 500$	71.2	0.145	0.291	75.0	75.1
$v \geq 500$	149.3	0.202	0.208	90.9	24.9
$v < 400$	75.9	0.166	0.079	69.1	42.9
$400 \leq v < 500$	64.5	0.116	0.221	82.8	32.1
$500 \leq v < 600$	112.3	0.175	0.100	89.8	15.6
$v \geq 600$	196.1	0.249	0.058	92.8	9.4

^a Based on observed solar wind speed.

The mean absolute percentage error (MAPE), which shows the error relative to the observed speed, is about 0.159. The correlation factor (CC) between the predicted and observed series is about 0.470 (with probability of chance occurrence well below 0.1% (Taylor, 1997)). The success rate of IMF polarity prediction is 81.2%.

In order to compare this result with previous work, we interpolate our prediction to an 1-hour resolution. For the period between mid-1996 (start of the MDI mission) and 2002, our calculation gives a RMSE of 92.3 km s⁻¹, which is comparable to the 94.9 km s⁻¹ RMSE (1995-2002, NSO data) reported by Owens *et al.* (2005). The daily averaged IMF polarity prediction accuracy for the 12-year time series, on the other hand, is 87.9%. It is consistent with the result from the first 8 years' MDI data (86.2%) reported by (Zhao *et al.*, 2006). We note that the new polar field interpolation method (see Chapter 3) improves the long-term SW speed prediction accuracy. A comparison of the mean square error (MSE) from two input series (one treated with the new polar field interpolation scheme and the other with a simple 1D interpolation to the pole along the same longitude) shows an overall 14.4% improvement. The improvement can be as high as ~40% during solar minimum (Sun *et al.*, 2011).

In Table 2.3, we classify the prediction according to observed speed and find that the slow wind ($v < 500$ km s⁻¹) is generally better predicted in term of errors. A finer classification reveals that the most accurately predicted SW speed lies between 400 km s⁻¹ and 500 km s⁻¹. The RMSE is the lowest, and the correlation between prediction and observation is the highest. It is partly because the slow wind makes up the majority of solar wind, 75.1% of total samples. They are thus heavily weighted and well represented by the optimized empirical function. On the other hand, the success

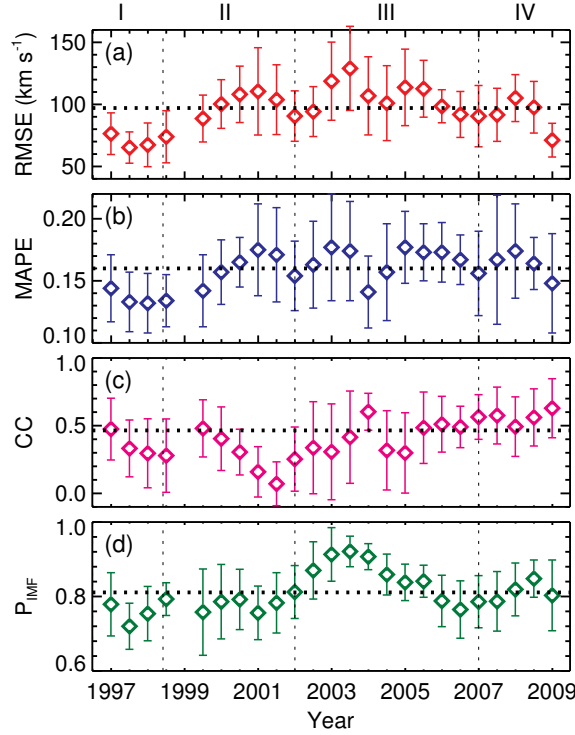


Figure 2.4: Statistical evaluation of the prediction from 1996 to 2009 against OMNI data. Each point represent the result from 1-year’s 4.5-hour time series centered at that time. Points are sampled every half year; data with temporal coverage below 50% are not included. (a) root mean square error, or RMSE (km s^{-1}) of speed prediction; (b) mean absolute percentage error (MAPE) of speed; (c) Pearson correlation coefficient (CC) between observed and predicted speed; (d) success rate of IMF polarity prediction (P_{IMF}). Horizontal dotted line denotes the mean value over a cycle. Vertical dotted lines roughly divide the solar cycle into four different phases (see Table 2.2). Error bars in (a) and (b) show the standard deviation of all data within 1-year’s window. Error bars in (c) and (d) show the standard deviation from 12 monthly results in each 1-year window. The result here includes all data points in the time series, whereas those suspected as transient ejecta were excluded from the parameter fitting.

rate of IMF prediction monotonically increases with observed speed. This is because fast wind usually comes from large coronal holes, the shape and location of which are well-defined. The field mapping is thus less error-prone.

We find that the performance of the model is strongly dependent on the phase of a solar cycle. Figure 2.4 shows the four statistical metrics with regard to time. In this figure, each point represents the statistics within a window of one year, and the windows are centered half year apart. Dotted line in each panel shows the overall value for the solar cycle. We subjectively divide the cycle into four phases according to the metrics value and show them with vertical dotted lines in Figure 2.4. They roughly correspond to different phases of cycle 23. The start, end time of each phase and the

overall metrics value are shown in rows 2 to 5 of Table 2.2.

1. The RMSE (as well as MAPE) is smaller during the minimum phases (I and IV). For phase I, this is due to the overall low SW speed. Fast streams were largely absent as discussed earlier. Phase IV had plenty of long-lived fast streams (discussed in Chapter 4), many of them were predicted with too low speed. This generally raises the RMSE value, but the error is still lower than the maximum and declining phases.
2. The correlation coefficient between the predicted and observed SW speed is the lowest during phase II (maximum), and highest during phase IV (minimum). The low correlation during the maximum phase is largely caused by the transient ejecta that frequently disturb the background solar wind (Cane and Richardson, 2003), when we do not expect the models to work well in general. On the other hand, the quasi-stable background wind during the minimum phase provides a good base for the WSA model. The recurring streams during phase IV enhanced the contrast of fast-slow streams and made the structures easier to be captured by the model.
3. The IMF polarity is most accurately predicted during phase III (declining). The large inclination of the current sheet forms well-defined 2 or 4 sector structures during this period. The current sheet usually intersects the ecliptic plane at a large angle, so the latitudinal uncertainty in the extrapolated field will not effect the result to a large extent. The waning of solar activity and transient ejecta also helps increase the accuracy.

We note that although the general trend in these metrics is clear and easy to interpret, it only applies when a longer time scale is considered. Counter-examples can almost always be found during each phase, and the causes can be very complex. In addition, the metrics can vary greatly on a shorter time scale (e.g. 1 CR), as seen from the “error bars” in Figure 2.4.

2.4 Factors Effecting Prediction Accuracy

2.4.1 The Optimization Scheme

Because the empirical function is retrospectively fit prior to the modeling, the statistical metrics obtained in this study give an estimate of the upper limit under the current modeling scheme over solar cycle 23. This approach is largely objective and provides a less biased evaluation on the capability of the WSA model. Nevertheless, some intrinsic issues with this approach can make the result misleading.

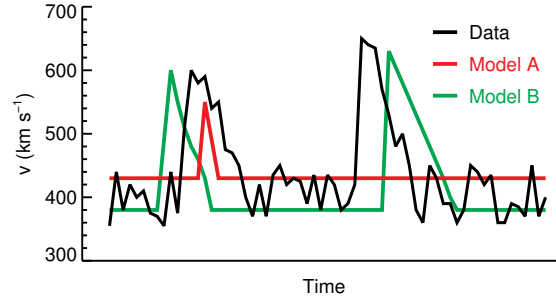


Figure 2.5: Example of misleading prediction statistics illustrated by artificial observed and modeled SW speeds. Black shows the observations. Model A fails to capture the large scale behavior, but performs statistically better than model B. The plot is adapted from Owens *et al.* (2005).

The current scheme usually underestimates the fast streams, which is evident from the relatively large errors for the $v \geq 600 \text{ km s}^{-1}$ category in Table 2.3. To lower the overall error, the optimization scheme tends to “compensatively” overestimate the slow background wind. This effectively yields a relatively “flat” prediction.

Figure 2.5 is adapted from the example in Owens *et al.* (2005). It demonstrates the issue with a hypothetical case. Three artificial SW speed series are plotted. The black line denotes the observation; the red and green lines show two hypothetical model predictions A and B. Although model B captures the large-scale behavior much better than A, the RMSE is greater than A (95.2 km s^{-1} vs. 71.8 km s^{-1}), and the correlation coefficient is lower (0.156 vs. 0.305).

Model A in Figure 2.5 is an extreme example but it explains the overall “flatness” of statistically fitted prediction. During the optimization process, empirical functions that predict a speed profile similar to B will be eliminated sooner due to the poor statistical performance. For practical purposes, one may adopt an event-based strategy (e.g. Owens *et al.*, 2005) that focuses on the “hit rate” of such high-speed streams. If high-speed events are the priority of the prediction, one may train the model more specifically, at the cost of overall statistical errors (which may be less important) and more false-positives. Such strategy seems more appropriate in practice.

Because the statistical metrics are dependent on the solar cycle, it is natural to consider fitting the empirical function for a certain period of time prior to the prediction. Repeated trial-and-error is naturally needed. Arguments against this approach is that we found 1) large variations of the model’s performance is often seen on a short time scale (from one CR to the next) and 2) the same phase of two cycles can act very differently.

We note that a straightforward but less accurate way to determine the coefficients for a specific

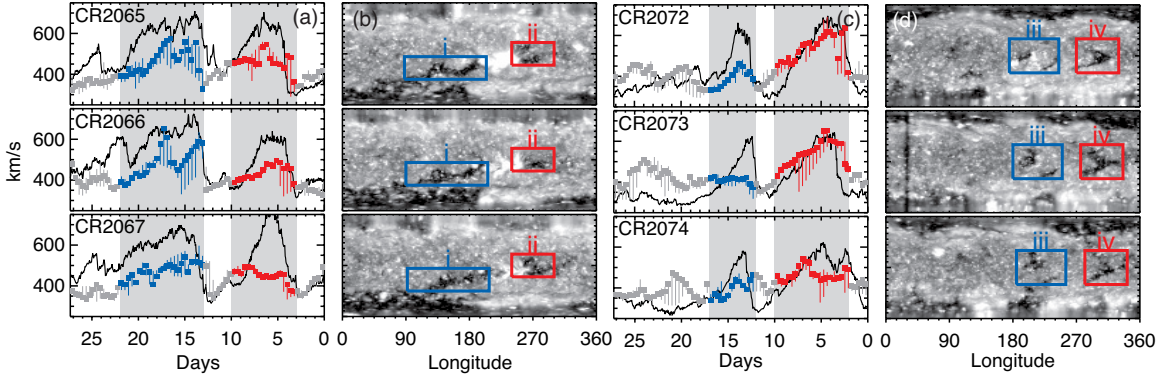


Figure 2.6: Prediction of four different kinds of recurring fast SW streams and their coronal sources. Note that time runs from right to left in the left column for easier comparison. (a) SW speed at L1 for CR2065-CR2067. Red squares show prediction; black curve shows the OMNI observation. Shaded background denotes the recurring fast stream. (b) *STEREO-A* SECCHI EUVI 195 Å synoptic maps. Red box identifies the derived source for the fast stream: low-latitude CHs that appear dark in EUV data. (c) Same as (a), for CR2072-CR2074. (d) Source regions for (c). These source regions are different from each other in term of configuration, size, and evolution trends.

input data set is to map the solar wind speed observed at L1 “ballistically” back to the source surface. Its source in the lower corona is then found by tracing field lines using the PFSS model to correlate the speed v with the parameter pair (f_s, θ_b) , thus we can directly use this correlation to fit the coefficients for the empirical function. There are several backward mapping schemes, some using constant solar wind transit time, some utilizing observed L1 speed. The mapping generally works well, but it overlooks the interaction between fast and slow streams. In fact, as the solar wind speed is highly supersonic at the L1 point, in principle, it is not possible to propagate the solar wind backward and account for the detail physical processes at the same time.

The longitudinal accuracy of such simple backward mapping was estimated to be from 10° to 20° (see Neugebauer *et al.*, 2002, and references therein). While larger discrepancy was found between different backward mapping schemes on individual cases, different schemes don’t seem to greatly affect the long-term correlation between SW speed and FTE (Poduval and Zhao, 2004). This makes the backward mapping a convenient tool for long-term studies.

2.4.2 Various Solar Features

We have shown in section 2.3.2 that the accuracy of prediction is strongly dependent on the phase of the activity cycle. Due to different coronal field structures, some aspects of the models are not expected to work as well in certain solar cycle phases (e.g. transient fast wind speed during maximum phase, or IMF polarity during deep minimum phase).

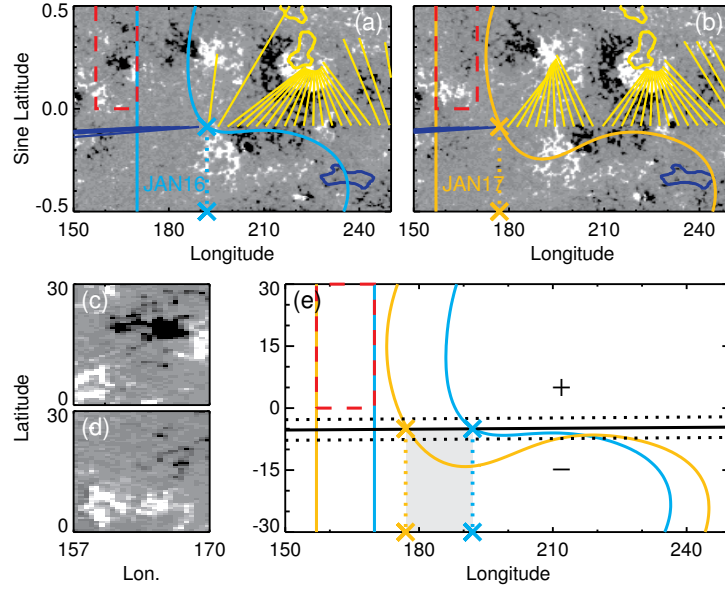


Figure 2.7: Drastic change of HCS ecliptic cross-over position due to its horizontal orientation and the change of surface field. (a) Derived HCS and sources of in-ecliptic flux based on input of January 16th, 2002. Background gray scale image is part of the daily-updated synoptic map between $\pm 30^\circ$ latitude and between 150° and 250° Carrington longitude. Straight line on the left shows the leading edge of the map; data left to this line is one CR older. Yellow/blue lines link the sub-Earth points to their sources for positive/negative open flux. Yellow/blue contours are observed CH boundary from KPVT He observation. The red dashed box shows the position where the surface field changes. The “X” mark shows the longitude where HCS crosses the ecliptic. (b) Same as (a), from January 17th input. (c) Close view of the boxed region in (a), which shows the condition about 1 month prior. (d) For boxed region in (b) where the negative flux disappears. (e) Comparison of derived HCS from two inputs. The horizontal solid line is the sub-Earth line and the dotted lines are $\pm 2.5^\circ$ in latitude. The grey area indicates the $\sim 15^\circ$ longitudinal difference in the HCS ecliptic crossover.

Some observed features on the Sun may give straightforward indications of model accuracy. For example, we identify in Figure 2.6 four kinds of recurring fast streams according to their source regions: i) large polar CH extensions; ii) newly formed low-latitude CH adjacent to decaying ARs; iii) less well-defined, evolving low-latitude CHs; iv) well-defined, large and long-lived low-latitude CHs. A survey of the 13-year archive suggests that the prediction seems more accurate for type iv, as the shape and size of such CHs are usually stable and well modeled. On the contrary, type i, ii and iii are less accurately modeled because those CHs often have a fragmented shape. The field mapping is thus less certain, leading to larger errors in the speed prediction. For detailed discussion on their formation and evolution, see [Abramenko et al. \(2010\)](#); [Wang et al. \(2010\)](#).

Another example involves the heliospheric current sheet (HCS) that is largely horizontally oriented and lies close to the ecliptic (note that HCS is co-spatial with the PIL). It is often seen during

the minimum phase, when the polarity of the IMF is constantly changing sign at the Earth. A “mixed” polarity will be observed, and the prediction is more uncertain. Similar situations sometimes occur during the maximum, too. In these cases, IMF polarity prediction can be wrong for days with a definitive sign. Figure 2.7 shows such an example for CR1985 in early 2002. Panels (a) and (b) show the derived sources of open flux from two daily-updated MDI synoptic map from January 16th and 17th. The leading edge of the map is denoted by the vertical line (data left to this line is one CR older). The yellow lines, indicating positive sign, map the flux between 180° and 210° to a positive plage region north to the ecliptic in panel (b). However, a majority of them gets mapped to a negative plage region about 30° east in the southern hemisphere in panel (a), according to the input of Jan 16. Note the disappeared (decayed) negative flux marked by the red boxes. A closer look of this region is shown in panel (d), whereas the corresponding region from the previous CR is shown in (c). In panel (e), the polarity inversion line from the 16th and 17th are overlaid. The flat shape of the HCS, in combination with the introduction of the new flux, causes a $\sim 15^\circ$ difference in the ecliptic crossover, roughly corresponding to a day. Moreover, if we consider the spatial resolution of our computation (2.5°), a difference as large as $\sim 40^\circ$ (3 days) may be found.

2.5 Comparison Between Different Extrapolation Methods

2.5.1 Field Configurations

Several potential-like field extrapolation models have been developed over the years. They have been briefly introduced in Section 1.3. The mathematical formulae are listed in Appendix A. Here, we discuss two of them and compare them with the PFSS model. We are especially interested in their performance at space weather prediction, when incorporated with the WSA model.

One of them is the potential field current sheet (PFCS) model (Schatten, 1971). The field is identical to PFSS extrapolation below R_s . Field above R_s , on the other hand, hosts a sheet-like current to emulate the effect of the HCS. It preserves the initial radial field constraint in the inner region and re-distributes the flux in the outer region. Discontinuity in tangential field is significant at the boundary (McGregor *et al.*, 2008), but the radial component is kept continuous.

The other is derived from the magnetostatic solutions, as formulated by Zhao and Hoeksema (1994). Magnetic field is extrapolated by using the current-free assumption up to R_s , but is no longer required to be radial there. As a result, the open flux is more evenly distributed in the heliosphere, consistent with Ulysses observation (Balogh *et al.*, 1995). The model proposed in Zhao and Hoeksema (1994) also include a parameterized, uniform volume-filling horizontal current near

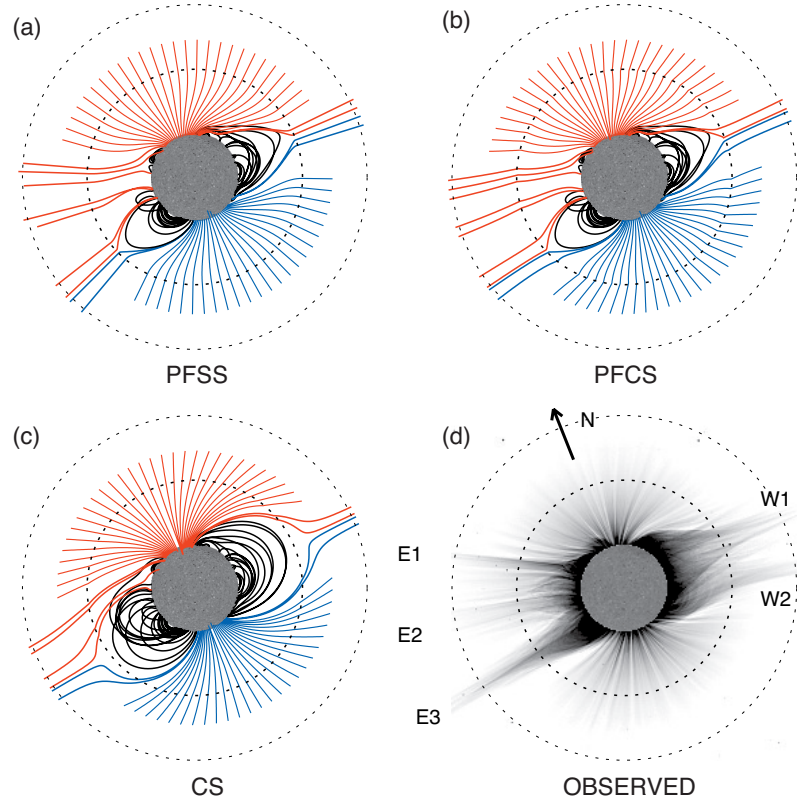


Figure 2.8: Illustration of coronal field structures derived from three different extrapolations and observation during the August 2008 total eclipse. Central meridian longitude is approximately 23° CR2072. Two dashed circles indicate radii of $2.5R_\odot$ and $4R_\odot$. Selective field lines that are located close to the limbs are plotted. Black is for closed loops simulating the helmet structure. Blue/red are for positive/negative open field lines. Field lines that reach $4R_\odot$ are selected to outline the helmet streamer; shorter ones are for polar plumes. (a) For PFSS model. (b) For PFCS model. (c) For CS model with a source surface of $2.5R_\odot$. (d) Negative of composite white light corona photo courtesy M. Druckmüller. Streamers marked with E2, W1 and W2 are helmet streamers, while E1 and E2 are likely to be “pseudo-streamers” (Wang, Sheeley, and Rich, 2007a). Direction of solar north is shown by the arrow in (d).

the Sun (see Appendix A). We set this current to 0, so the only difference between this model and the PFCS model is the radial field requirement at R_s . We call this model the current sheet (CS) model.

We illustrate the characteristics of these models in Figure 2.8 using the example of the 2008 solar eclipse (e.g. Wang *et al.*, 2007b). The negative of the white light coronal photograph in panel (d) shows five prominent streamer structures, as well as clear polar plume structure. We use a synoptic map centered at longitude 23° , CR2072 (when the eclipse occurred) to extrapolate the coronal field using three different models. Panel (a) (b) (c) shows the selected field lines from the PFSS, PFCS, and CS model respectively. Note only field lines located near the limbs are represented. For all three

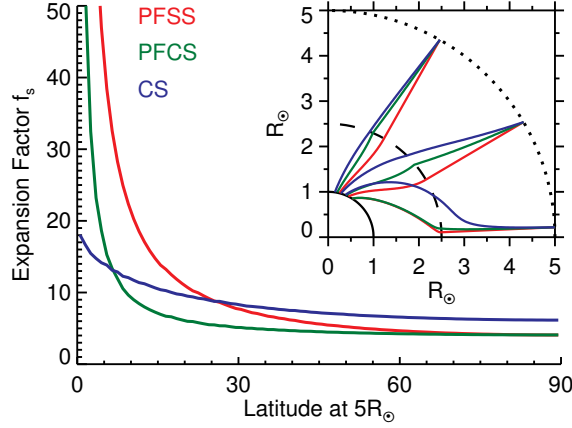


Figure 2.9: Comparison of three extrapolation models based on an axisymmetric case with photospheric field $B = \cos^7 \theta$, where θ is the latitude. FTE from three extrapolation models are plotted as a function of latitude at $5R_\odot$, where the field line tracing first begins. The CS model with a $2.5R_\odot$ source surface shows a much uniform profile than the other two models. The inset shows three sets of field lines starting from 2.5° , 30° and 60° latitude at $5R_\odot$ respectively.

models, we use $R_s = 2.5R_\odot$. Three distinctive characteristics can be concluded.

1. The polar plume structure appears to be non-radial above $2.5R_\odot$. The radial constraint of the PFSS model and the “kinks” at R_s in the PFCS model do not match observation very well. The CS model simulates the structure better than the previous two.
2. The closed loops of the helmet streamers (marked E3, W1, W2 in Figure 2.8(d)) are confined below $2.5R_\odot$. The PFSS and PFCS model have the same closed field structure, and both reasonably reproduce the shape of E3 and W1. (W2 originates closer to the disk center and is not plotted here.) On the other hand, the CS model does not have a radial field constraint at R_s so less flux becomes open. A much larger closed loop structure thus appears for both E3 and W1.
3. The open field lines of helmet streamers (E3 and W1) are reasonably modeled in terms of location and direction. Nevertheless, the negative (red) field lines seem to be mapped to very different locations in the CS model than the other two.

2.5.2 Different Field Line Mappings

In the WSA model, the mapping of the open flux back to the photosphere exclusively determines the modeled SW speed. Figure 2.8 suggests that the mappings in the PFSS model and the coupled

PFCS model are similar to each other. The CS model, on the other hand, seems to have a different field configuration.

Figure 2.9 shows the value of f_s as a function of latitude for an axisymmetric photospheric input $B_r = \cos^7 \theta$. θ is the latitude. This is a similar test done by Wang and Sheeley (1990): only the polar caps are available as the source of open flux. A $2.5R_\odot$ source surface is used for CS, and f_s is computed between $2.5R_\odot$ and photosphere. Also shown are three sets of field lines, traced down from latitude 2.5° , 30° , and 60° respectively. The CS model maps low-latitude open flux to a higher photospheric latitude than the other two models, resulting in 1) a smaller polar CH and 2) a weaker latitudinal gradient of f_s . In fact, the radius of the CS polar cap is about 22° , about 10° smaller than the other two models. Big expansion is seen near the polarity reversal region for PFSS and PFCS model. The CS's profile, on the contrary, is more uniform. This test leads us to believe that the CS gives a more uniform solar wind prediction, one differs from the other two models. The performance is evaluated in the next section.

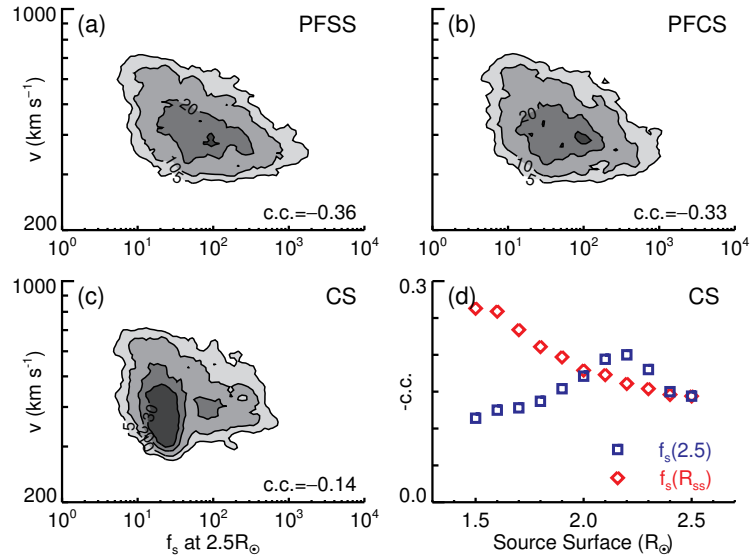


Figure 2.10: Correlation between inferred FTE (f_s) computed from three extrapolation models and observed SW speed (v). Density of scatter plot (2D histogram) of the 13-year time series is shown. The bin size is 0.01×0.01 in logarithm space. Correlation coefficient is shown in each case. The OMNI data is mapped back to $5R_\odot$ with a 4.5-hour resolution. Field lines are traced back from 5° to get the FTE. (a) For PFSS model. (b) For PFCS model. (c) For CS model with a source surface of $2.5R_\odot$. (d) Negative correlation coefficient for CS with different trial cusp surface heights R_s . One set computes FTE between $2.5R_\odot$ and photosphere despite the varying R_s (blue square); the other computes FTE between the varying R_s and photosphere (red diamond).

2.5.3 Testing Correlation Between FTE and SW Speed

To initially assess these models' long-term performance with real solar wind prediction, we first perform the basic expansion factor v.s. SW speed correlation test described in the Section 2.4.1. 13-years SW speed (1996-2009) time series is simply mapped back to R_s and paired with the modeled f_s . If there is a strong anti-correlation between the inferred f_s and the observed v , similar to what led to the development of the WSA model (Wang and Sheeley, 1990), then there is good possibility that the extrapolation can be used for space weather prediction. In Figure 2.10(a)-(c), we show the density distribution of scatter plot for f_s - v in a logarithm scale. While the PFSS and PFCS model display similar behavior with -0.36 and -0.33 correlation coefficient respectively, the CS model suffers from a large cluster of f_s 's that have similar values but correspond to a wide range of SW speed (the narrow vertical region shaded with darkest gray). As a result, the correlation is only -0.14.

We test other values of cusp surface radius R_s for the CS model as well. Two sets of f_s are studied: one measures the expansion between the varying source surface and the photosphere (red); the other uses $2.5R_\odot$ as upper boundary despite the changing R_s (blue). As shown in Figure 2.10(d), the correlation peaks at -0.26 with $R_s = 1.5R_\odot$ for the first set, and about -0.20 with $R_s = 2.0R_\odot$ for the second set. Both correlations are still much worse than the other two models.

2.5.4 Space Weather Prediction with Different Extrapolations

To get a more accurate measure, we formally employ the PFCS and the CS model to predict the SW speed and IMF polarity at L1 point. For the CS model, we use $R_s = 2.5R_\odot$ as an example. All the steps done in the PFSS case are followed. The trial-and-error empirical function optimization is also performed in the hope to quantify the upper limit of each model's performance. The optimized coefficients of the empirical function and statistical metrics are listed in Table 2.1. The larger values of empirical coefficients used for the CS model magnify the variation of the coronal structure (f_s , θ_b), which is weak in the model.

As shown by the metrics in Table 2.1, the CS model still yields a lower correlation between the predicted and observed speed series. On the other hand, the polarity prediction is similar for all three models, suggesting the error in speed does not greatly affect the long-term IMF result. We use Figure 2.11 to show how detailed predictions typically differ from each other. Only the PFSS and CS models are shown here; results from the PFCS model are very similar to that of the PFSS model.

1. The CS model maps open flux to polar regions instead of low-latitude regions, causing too

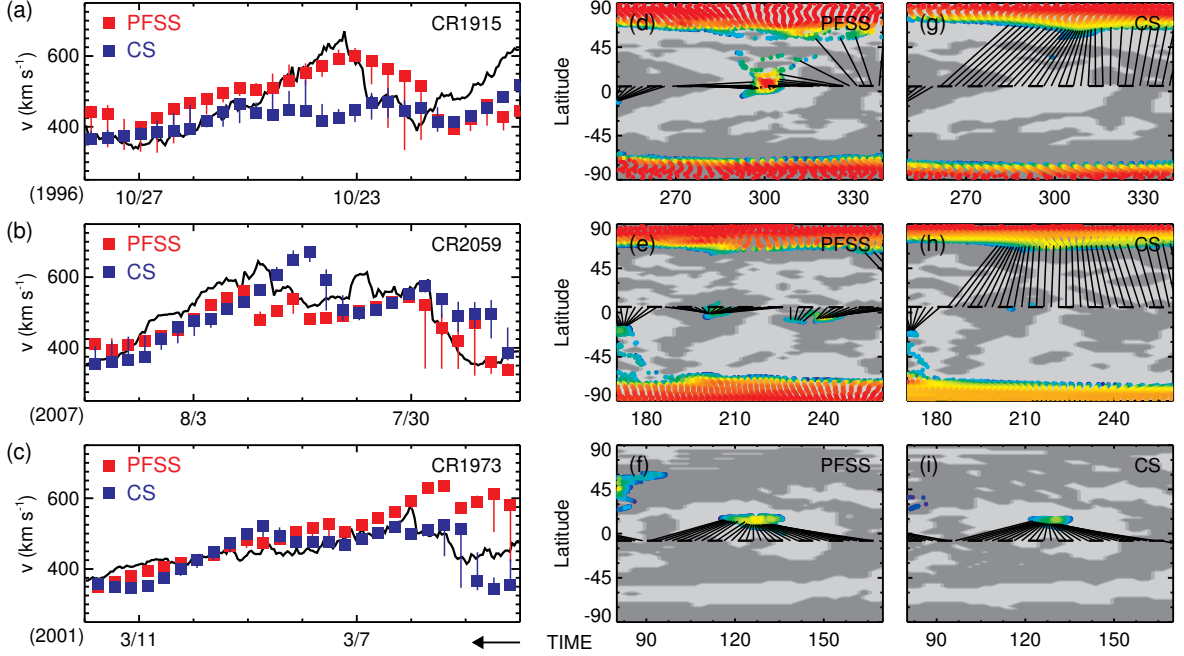


Figure 2.11: Examples of prediction made by different extrapolation methods. 8 days from CR1915, CR2059, CR1973 each are selected to illustrate how models differ in various ways. Only the results from the PFSS and CS model are shown. The empirical functions used are fitted specifically for different models. Note that time runs from right to left in the left column for easier comparison. (a)-(c) WSA solar wind prediction at L1, similar to Figure 2.6. (d)-(i) Derived photospheric source from the PFSS and CS model, similar to those in Figure 2.3(d).

little speed variation. Panel (a) shows one of these cases. A high speed stream whose trailing edge is well modeled by the PFSS model (note that time runs from right to left) but the CS model predicts a speed series to uniform and slow. Panels (d) and (g) in the top row show the corresponding coronal sources derived from the PFSS and CS model. A large low-latitude CH serves as the origin of this stream in the PFSS scenario, whereas all flux comes from the polar region for the CS case.

2. The CS model maps the open flux to polar regions instead of to low-latitude regions, but deep enough into the polar cap to make up for the differences. In panel (b), predictions from two models reasonably agree with each other, but the solar wind sources are totally different. In PFSS, solar wind comes from two individual low-latitude CHs. In the CS model, the solar wind comes from several degrees within the large polar cap. The effect of parameter θ_b is strong enough to offset the differences in f_s .

3. All models map to the same CH (either polar or low-latitude). In this case, the results tend to be similar. Although f_s derived by the CS model is usually still more uniform, the optimized empirical function seems to make up for the differences. The bottom row in the figure illustrate such a case.

When the background solar wind is stable, it may often be possible to differentiate the correct mapping from the wrong one by using the in-situ solar wind plasma component data (e.g. [Neugebauer et al., 1998, 2002](#)). However, it is out of the scope of this dissertation.

2.6 Summary

We retrospectively optimize the space weather forecasting scheme for the MDI data for solar cycle 23 (1996-2009). First, we make use of improved boundary condition for the field extrapolation: a series of daily-updated maps provides timely surface magnetic conditions, and a polar field interpolation scheme that provides a better estimate of the high latitude field strength. Second, we statistically optimize the empirical function that links the extrapolated coronal field configuration to the observed SW speed and IMF polarity near the Earth.

We evaluate various statistical metrics of the 3-day advanced in-ecliptic prediction. Overall, the scheme yields a percentage error of $\sim 16\%$ for the SW speed, and the IMF polarity forecast are correct $\sim 81\%$ of the time. This result slightly improves upon the previously literature. During different phases of the solar cycle, the performance of the model can be very different. For example, the error of speed prediction is the lowest during the minimum phase, while the IMF polarity accuracy is the highest during the declining phase.

Because the evaluated statistical metrics are also used to optimize the model prior, the performance of the model is effectively a “conditioned” upper limit under the current scheme. Various factors may affect its accuracy, including some distinctive solar features such as long-lived CHs, or fast evolving flux patches. The statistical optimization scheme seems yield an overall “flatter” prediction: an event-based scheme which favors the prediction of high speed streams may be more appropriate for practical purposes.

We evaluate the coupling of the WSA model and two additional extrapolation methods that include the effect of an outer corona current sheet: the PFCS and the CS model. The CS model does not require the field to become radial at the source surface, which yields more closed field. The field line mappings are thus different: the CS model maps most of the open flux to higher latitudes, resulting in a smaller latitudinal gradient of FTE, and consequently little variations in the modeled

SW speed. It seems that the extrapolation methods without radial field requirement on the source surface is not suited for the WSA model, given the current prediction procedures.

* For this Chapter I adapted the extrapolation code, performed the modeling and all the analysis. Dr. X. Zhao provided the original PFSS and HCCSSS extrapolation code. Dr. C. N. Arge provided the kinetic solar wind propagation code.

Chapter 3

Improving Space Weather Prediction: A New Polar Field Interpolation Scheme

3.1 Introduction

The observed photospheric magnetic field, in the form of line-of-sight (LOS) magnetograms assembled into synoptic maps, has been used to model the coronal field for more than 30 years (Schatten, Wilcox, and Ness, 1969; Hoeksema, 1984; Wang and Sheeley, 1990; Linker *et al.*, 1999). The global field serves as the boundary condition, which is essential to most coronal and interplanetary models. Although much effort has been devoted to improve the data quality, many issues are still not fully resolved. One of them is the quality of the magnetic field in the polar regions.

During most of the solar cycle, the polar region has a field of predominantly one polarity. Though it accounts for only a small fraction of the solar surface area, just 3.4% above 75° latitude, because the unipolar caps are the source of the stable polar coronal holes, the magnetic field from this region proves to be crucial to large-scale modeling efforts (Hoeksema, 1984; Arge and Pizzo, 2000; Luhmann *et al.*, 2009). Due to the Sun’s tilted rotation axis relative to the ecliptic and the line-of-sight nature of the magnetic field observations, there are data missing or poorly measured at one or both poles throughout the year, and the noise level is relatively high. For MDI synoptic maps, there can be as many as 16 rows of pixels missing from the upper/lower edge out of the total 1080. Figure 3.1 shows a stereoscopic polar projection of the magnetic field during CR1920 (March 1997) and CR1924 (July 1997). Black regions indicate missing data.

This chapter describes a new interpolation method (a.k.a. “polar field correction”) for estimating the problematic values in the polar region. The method can be applied to interpolate historic values and extrapolate future field strength. We note that any such polar field correction method is designed

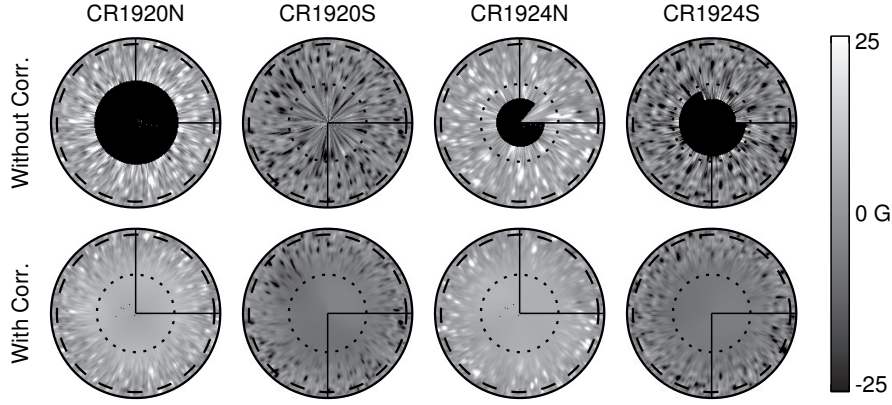


Figure 3.1: MDI synoptic maps of the radial field strength above 60° stereoscopically viewed from the poles: CR1920 (March 1997) and CR1924 (July 1997). In this projection, colatitude (θ) increases with the distance (R) from the pole at the center of the circle as $R \propto \tan \theta/2$, approximately linearly in this plot. Black indicates missing data. The top row shows the original data. The bottom row shows the field after interpolation. The small dotted circles indicate 75° latitude, the larger is at 62° . Horizontal solid lines show 0° Carrington longitude, vertical 90° .

for the study of long-lived, global, large-scale magnetic field. Individual small-scale structures of the photospheric field, such as rapidly evolving magnetic elements, are not as important for global field models and are beyond the scope of this chapter.

The MDI magnetic synoptic map construction method was introduced earlier in Section 1.2.3 and will not be repeated here. In Section 3.2, we give a brief review of several existing interpolation schemes. A detailed description of the new method is presented in Section 3.3. To validate the method, we prepare MDI maps processed with the new method as well as some of the old methods and apply them to the WSA model and a daily MHD simulation (Hayashi, Zhao, and Liu, 2008). A comparison of results is shown in Section 3.4.

3.2 Brief Review of Existing Methods

3.2.1 Seven Interpolation Methods

Seven different polar field interpolation methods have been studied and compared in Liu *et al.* (2007). We briefly summarize these methods.

1. *One-dimensional cubic spline interpolation.* 4 successive observed pixels are chosen from each column in the Carrington data array at one longitude adjacent to the missing data area. Another 4 pixels are chosen 180° in longitude away in the same fashion. A cubic-spline

interpolation is performed with 4 known pixels at each end and the interpolated values are used for the polar region.

2. *Modified one-dimensional cubic spline interpolation.* Similar to method 1. The original map is smoothed before the interpolation.
3. *Spheric harmonic smoothing method.* The one-dimension cubic spline interpolation (method 1) is performed on the original map first. A spherical harmonic expansion is performed and high-order components are truncated. The reconstructed, smoother field with only lower-order components is used for the polar region.
4. *Two-dimensional spatial interpolation.* Observed data from lower latitudes of each hemisphere are fit with a third-order two-dimensional polynomial function that spans the polar region by using the least-square technique. The fit values are used for the missing data.
5. *Two-dimensional temporal interpolation.* Each year, about a month of the polar data centered at September 8th (March 6th) for north (south) pole is used. The Sun's tilt angle reaches maximum at those two times and one pole becomes better observed. After fitting with a polynomial function (same as method 4), these annual data form a temporal series that can be used to interpolate for field strength at any given time.
6. *Polar field model method.* A “topknot” polar field as modeled by [Svalgaard, Duvall, and Scherrer \(1978\)](#) is used (see also [Wang and Sheeley, 1988](#)). In this model $B_r = B_p \cos^n \theta$, $B_\theta = B_r \tan(q\theta)$, where B_p is the field strength at the very pole, and θ is the colatitude. Free parameters n and q are determined using observations from the Wilcox Solar Observatory (WSO) as $n = 8$ and $q = 0$. In this way, the polar field is entirely determined by the value of B_p . Each year, the best observed polar field (as mentioned in method 5) is longitudinally averaged above 65° and fitted for B_p . These annual values of B_p can be used to interpolate B_p and construct the polar field for any desired time.
7. *Method based on Flux Transport model.* Polar field determined from a flux transport model [Schrijver and DeRosa \(2003\)](#) is adopted. This model includes the effect of differential rotation, meridional flow and supergranular random-walk dispersal. Available MDI magnetograms are assimilated within 60 degrees from the disk center every 6 hours. When the 180 degree longitude of a synoptic map passes central meridian, assimilated polar field data at this instant of time is used to fill out the polar region of the entire map.

3.2.2 Comments on Existing Methods

In Liu *et al.* (2007), these methods were applied to a set of nine MDI synoptic maps that were used for PFSS computations. Three of these nine maps were taken from the solar cycle minimum phase, three from the maximum phase, and three from the declining phase. The computed open field line footpoints and the heliospheric current sheet (HCS) location were compared with observations, such as coronal hole maps from Kitt Peak (He 1083 nm) and measurements of the interplanetary magnetic field (IMF) polarity at 1 AU.

Overall, the two-dimensional temporal interpolation (method 4) gave the best result. Similar but slightly less satisfying results were obtained from method 5 and 7. Some of these models prove to be sensitive to the noise signal in the original map and are error-prone. For example, the one-dimensional cubic spline interpolation method does not give very reasonable FP configurations for the test Carrington rotations, because the interpolation heavily depends on the pixels we choose. If the chosen pixels happen to fall in some magnetic elements, the interpolated values will then be unreasonably high. We will see an example of this in Section 3.4.

In most of these methods, the actual area being interpolated varies from rotation to rotation during the year. For instance, during July (CR1924) when both poles have missing data, both poles will be corrected (Figure 3.1). However, during March (CR1920) when the south pole is well observed, only the north pole will be corrected. Clearly the two poles will then have different noise levels. We note that using unsmoothed polar data can lead to unreasonable modeling result even when they are well observed (see Section 3.4). Furthermore, simple interpolation will leave discontinuities at the boundary of original and interpolated data. This is because the filled-in values are usually smoothed, while the original data are noisier. These issues are worth considering when we design a new interpolation method.

3.3 The New Interpolation Scheme

3.3.1 Procedures

A good polar field interpolation method should be able to 1) give a reasonable estimate of missing data and 2) lower the noise by smoothing to prevent biased modeling results. An objective, self-consistent method that processes *all* synoptic maps with a *single* standard process is preferred. It is also desirable to utilize as much of the good-quality observed data as possible.

We base the new polar field correction scheme on the two-dimensional spatial and temporal

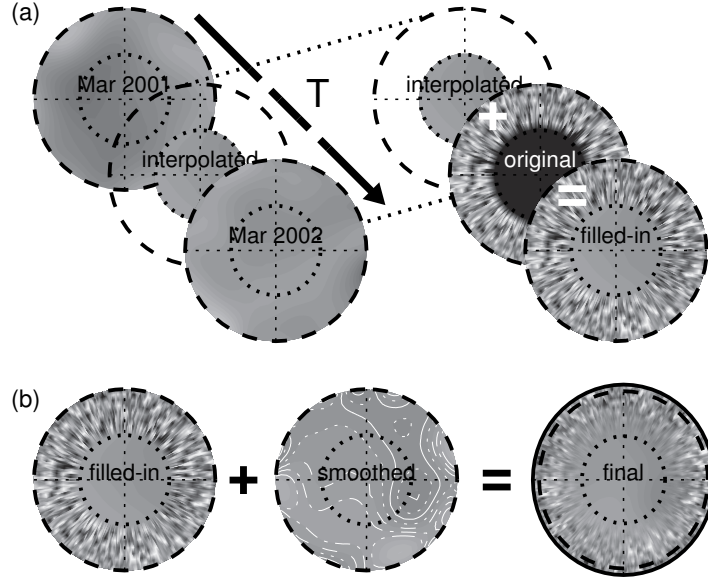


Figure 3.2: Illustration of the new polar field correction scheme. The circular plates are stereoscopic views of the South poles above 62° latitude. Smaller dotted circles indicate 75° . Black indicates missing data. Panel (a) shows the step of estimating the poorly measured pole-most pixels at a certain instant between March 2001 and March 2002 above 75° . The temporally interpolated values are used to replace the pole-most pixels in observation. Panel (b) shows the process of smoothly merging the filled-in data back to the map. The observed field with gap filled is smoothed and merged back to reduce the noise level in a standard way.

interpolation methods (method 4 and 5) and implement a few key improvements. For extrapolation, we incorporate a simple variation of the flux transport model (method 7) which is described later in this Section. Figure 3.1 shows the corrected polar field for CR1920 and CR1924 as a comparison with the original data.

Three major issues remain for the original spatial/temporal interpolation methods. 1) The observed data at the polar regions that are used for fitting or smoothing vary in quality themselves. If one pole is tilted away from the Earth, we will have to use fewer/noisier pixels to estimate more missing pixels. This is likely to result in very different data quality at two poles in a map, and also from map to map. 2) The missing/noisy pixels in the polar region are usually directly replaced by fitted/smoothed values, a discontinuity in noise level is usually unavoidable. 3) The method needs to provide an extrapolated result for modeling the present as well as interpolated results for historical study. As we will see in Section 3.4, not addressing these issues may lead to unreasonable model result.

Therefore, we design and describe the following procedures.

Step 1: *Estimate the higher-latitude data based on the best polar observations during the year.* Figure 3.2(a) illustrates this step. Instead of fitting directly from current low-latitude data that vary in quality, we make use of the best polar observations available at September 8th (March 6th) each year for north (south) pole. A total of 13 annual north (south) polar observations are thus gathered from 1996 to 2009 (excluding the “SOHO vacation” in summer 1998). We smooth the well-observed data above 62° using a seventh order polynomial function. The third-order polynomial originally used in Liu *et al.* (2007) does not seem to reproduce enough variations in the large scale field strength for the full-resolution maps. These smoothed data are aligned according to Carrington coordinate, so pixels with the same Carrington coordinates form a time series. We then use this annual time series and perform a temporal one-dimensional cubic spline interpolation to synthesize the values above 75° latitude, for *both* poles in *each* map for each rotation.

Step 2: *Merge the synthetic data with the original observation.* At this stage the polar data for any rotation consist of two parts: the original observation below 75° latitude, and the smoothed, evolved, filled-in data above, as shown in figure 3.2(b). In order to minimize the discontinuity between them, the same two-dimensional smoothing is first performed on this two-part polar data above 62° latitude to create a smoothed polar “mask” for each rotation. To produce the final polar field, pixels above 75° latitude are directly taken from the mask. Between 62° and 75° we make a linear combination of the mask data and the original unsmoothed observations, their weight linearly increases with latitude from 0 to 1 (or decreases from 1 to 0). As a result, the noise level gradually decreases from 62° to 75° without apparent discontinuity.

3.3.2 Notes on the New Method

Figure 3.3 shows the average radial field strength of the well-observed polar data above 75° latitude observed during each favorable season. As net new flux is gradually transported from lower latitudes, the flux density changes gradually from one year to the next. Note that due to the small size of the polar region, most global models respond sensitively only to the average value of the field, and do not so much depend on the detailed spatial flux distribution. The simple interpolation we use here reflects this gradual change of flux density and thus provides an adequate estimate of the missing pixels.

The well observed polar field data are assembled from standard synoptic maps that have a nominal resolution of 3600 in longitude and 1080 in sine latitude. The polar strips are 63 pixels high to include the region above $\sim 62^\circ$ latitude. The latitude range is chosen according to the polar

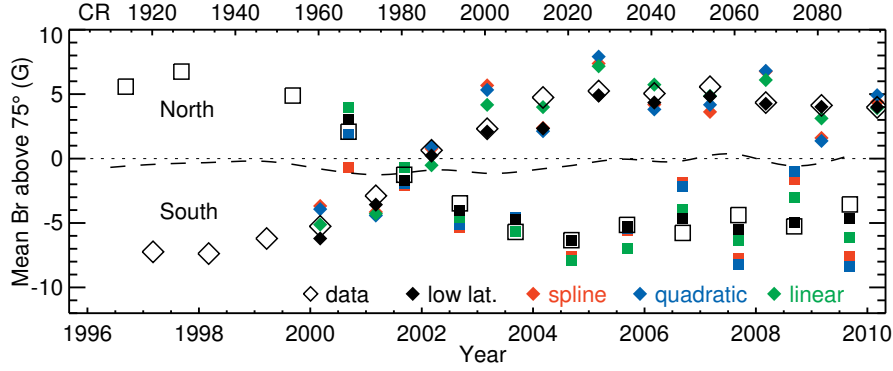


Figure 3.3: Comparison of four extrapolation methods for estimating the polar field strength of the next year: average from low-latitudes, cubic spline, quadratic and linear. Open squares (diamonds) indicate smoothed and averaged polar field flux density above 75° latitude in the north (south) during September (March). Each extrapolated point is based only on the data points before it. The low-latitude data are the average of the flux-density between 62° and 75° multiplied by 1.1, from the previous year. The dashed curve shows the average field strength difference between two poles after smoothing and averaging, which represents the residual imbalanced flux from polar field after the correction.

coronal hole size during the past sunspot minimum, which usually has a $\sim 30^\circ$ extent in latitude. The strips are significantly extended in longitude to account for differential rotation. Strips span 429° Carrington degrees (~ 32.5 days) in accordance with the differential rotation rate at 75° latitude [Meunier \(2005\)](#). As the polar region rotates more slowly, this extra ~ 5.2 days (compared with the nominal 27.3 day Carrington period) allows us to include information for the Sun's entire polar region.

Above 75° latitude (the top and bottom 18 rows) the values are simply replaced by the temporally interpolated data. This range is only slightly larger than the extreme cases where there can be 16 rows missing from the polar region of the synoptic map. The replacement is made for *both* poles and *all* synoptic maps to keep the noise level comparable for the two poles in each map, as well as for the same pole in different maps.

Because observations of the following September/March are not yet available when considering recent time intervals, an interpolation method cannot be used for the correction of up-to-date maps. A reliable extrapolation scheme must be developed to estimate the missing data. The results for several regular extrapolation methods (spline, quadratic, linear, sinusoidal, etc.) are shown by the indicated symbols in figure 3.3. Starting yearly in 2000, we extrapolate the averaged flux density of north/south pole based on the prior observation series. The extrapolated value depends heavily on a few points proceeding the desired time, so the prediction is prone to diverge from the actual observation whenever the evolution of the polar field deviates from what is described by the

extrapolation function. This is especially true for this deep sunspot minimum when the polar field remained significantly weaker for a longer period than the previous ones (e.g. in September 2006).

The best prediction uses the average flux density in the slightly lower latitude range between 62° and 75° from previous year. The result, multiplied by 1.1 (in filled black square/diamond), is much better correlated with the observed values (open square/diamond). Therefore we use this lower-latitude average value to scale the most recent September/March observation and use the scaled data as the “projected” observation for the following September/March. A regular temporal interpolation can then be performed. When new September/March observations eventually become available, we substitute the “projected” observation with the measured values. This means we will update the polar field values for the past year twice every year, in late March and September.

Like other polar field interpolation schemes, the two polar regions we have defined may not be in flux balance, as shown by the dashed line in figure 3.3. It is hard to tell how much of the residue is an artifact of the process and how much represents a real local imbalance. Systematic differences in the instrument or the specification of our polar geometry parameters may also play a role. The apparent monopole component of the full maps, which is typically discarded during modeling, may sometimes cause a significant shift of field inversion line location in the upper corona and lead to erroneous results. Quantitatively, the net flux in the corrected polar regions has a maximum average field strength of ~ 2 Gauss in the polar region during sunspot maximum, and is very close to 0 during most other times. A 2 Gauss average above 75° is equivalent to global offset of less than 0.1 Gauss. An offset of this magnitude is of less importance during the maximum phase due to the greater influence of the stronger high-order field components. The global coronal structure is more likely to be affected by the evolution and eruption of strong active regions.

3.4 Validation and Discussion

3.4.1 WSA Model

We use polar field corrected MDI synoptic maps as the input to the WSA model for solar wind prediction. Following the method described in Chapter 2, we predict the ~ 3 -day advanced solar wind speed at L1 from 1996 to 2009 (CR1912 to CR2084). The predicted solar wind speed at L1 is evaluated by comparing with the OMNI observations (King and Papitashvili, 2005) on a point-by-point basis. The prediction time series and the OMNI hourly data are first interpolated/averaged to the same temporal resolution. Four statistical metrics are studied: root-mean-square error of the predicted speed (RMSE), mean absolute percentage error (MAPE), correlation coefficient between

Table 3.1: Statistical evaluation of solar wind prediction from the WSA model from July 1996 to March 2009. Predictions were made using synoptic maps with the new polar field correction and the 1D interpolation. Results are based on the 3-day advanced prediction and are evaluated against the OMNI data set. Four statistical measures are evaluated: root-mean-square error of the predicted speed (RMSE), mean absolute percentage error (MAPE), correlation coefficient between the predicted and observed speed (CC), and the success rate of IMF polarity prediction (PIMF).

Synoptic Map	RMSE(km/s)	MAPE	CC	PIMF
New Method	96.8	0.159	0.470	0.812
1D Interpolation	104.6	0.179	0.364	0.781

the predicted and observed speed (CC), and the success rate of IMF polarity prediction (PIMF). Since these metrics are also used to optimize the empirical equation, the model result essentially estimates the model’s best statistical performance on solar wind prediction.

The first row of Table 3.1 shows the statistics for the prediction with a 4.5-hour resolution (corresponding to the 2.5° input resolution). The model gives an overall 96.8 km/s RMSE, which is equivalent to about 15.9% error. The predicted velocity time series has a correlation coefficient of 0.470 with the observed series. The IMF polarity prediction is correct 81.2% of time. If we interpolate our prediction to a 1-hour resolution (Owens *et al.*, 2008), the same analysis shows a RMSE of 92.3 km/s between 1996 and 2002, comparable to the result (94.9 km/s) given in the same paper (for 1995-2002).

To demonstrate the effect of the new correction scheme, synoptic maps with the polar correction based on the one-dimensional interpolation method described above are also evaluated using the same procedures. As shown in Table 3.1, the new polar field method improves the model’s performances in all 4 categories. The improvement is especially pronounced during the sunspot minimum phase when the polar fields are strongest and most uniform. We compare two versions of mean-square error of speed, through the index of “skill score” :

$$\text{skill} = \left(1 - \frac{\text{MSE}}{\text{MSE}_{\text{ref}}}\right) \times 100, \quad (3.1)$$

where we use the MSE of the 1D interpolated version as the reference. Figure 3.4(a) shows the RMSE value of two methods. Each point represents the RMSE of data within a one year window and the points are sampled every half a year. The skill score of MSE for the new method compared to the 1D method is shown in figure 3.4(b). It can be as high as ~ 40 (improvement of 40%) during the solar

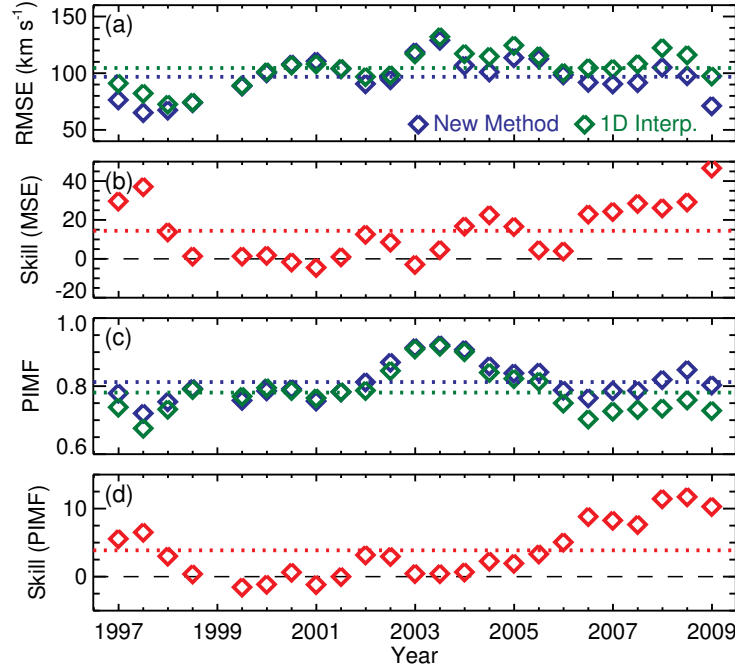


Figure 3.4: Statistical metrics for WSA solar wind speed and IMF polarity prediction compared with OMNI data. Results from synoptic maps with new polar field correction scheme are compared with those that use one-dimension interpolation. Each point represents a one-year window and the points are sampled every half a year. The overall average is shown as a horizontal dotted line. (a) Root mean square error (RMSE) from the new method (blue) and 1D interpolation method (green). (b) Skill score of mean square error (MSE) of the new method using the 1D method as reference. (c) Success rate of IMF polarity prediction (PIMF) from the new method (blue) and 1D interpolation method (green). (d) Skill score of the new method using the 1D method as reference.

minima, with an average of 14.4 over the solar cycle. The long-term, overall accuracy of solar wind prediction is improved after we apply the new method. We notice that from 1999 to 2001, when the polar field was near zero, the new method yields slightly worse result than the 1D interpolation result. It might be because the polar field does not change smoothly due to the arrival of new flux in the form of “magnetic surges”, which makes the new method inaccurate. Nevertheless it is hard to determine the cause because the effect of polar field is less dominant during the maximum phase and more transient ejecta start to affect the background solar wind flow.

Figure 3.4(c) and 3.4(d) show a similar comparison for PIMF. The skill score is now defined as

$$\text{skill} = \left(\frac{\text{PIMF}}{\text{PIMF}_{\text{ref}}} - 1 \right) \times 100, \quad (3.2)$$

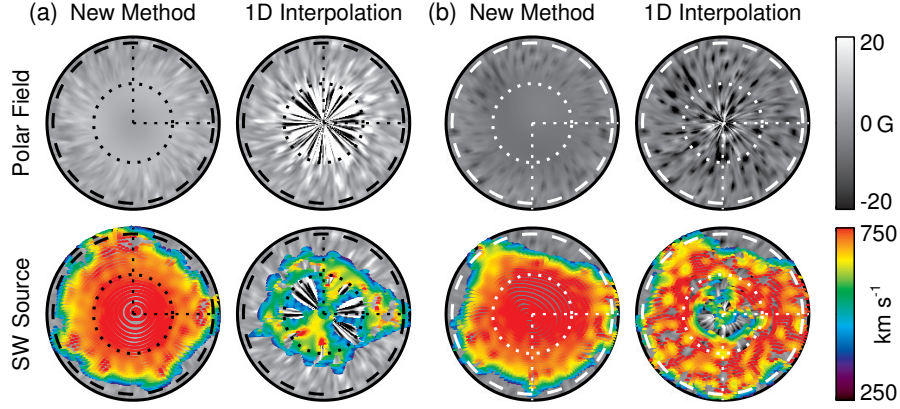


Figure 3.5: Comparison of derived open field line foot-points as the source location for high-latitude fast solar wind during solar minimum (CR1920), computed with new polar field correction and with 1D spatial interpolation method. (a) shows the North pole view. (b) show the South pole. In each panel, the top row shows the magnetic data after correction. The bottom shows the wind source overplotted on synoptic map, with colors indicating corresponding solar wind speed.

as higher PIMF indicates better accuracy. Again, we use the result from 1D interpolation as reference. Although the time variation of PIMF is very different from RMSE, the skill score shows a similar trend, being the highest during the recent minimum ($\sim 15\%$). The 1D interpolation sometimes produces biased polar field strength which distorts the shape and location of the HCS, leading to erroneous IMF polarity prediction. It is clear that a good estimate of the polar field is crucial to the models during solar minimum period.

In the WSA model, sources of solar wind are identified by mapping field lines back to the photosphere from the corona, as solar wind is accelerated along flux tubes. In figure 3.5(a), the top two plots show the north pole view of magnetic field synoptic map above 60° latitude for CR 1920. The left plot is computed based on data processed with the new method, the right one shows the result for the one-dimensional interpolation. The bottom two show the computed open field regions from these two maps. The color indicates the predicted solar wind speed. Figure 3.5(b) shows the same for south pole. (Since the south pole is well observed during this time, no correction is required at the south pole for the 1D method.) Note that even though the south pole is well observed, noisy data with large flux of the opposite polarity can still lead to large-scale closed field structures. Large-scale low-speed solar wind streams appears at the center of the large polar coronal hole, which disagrees with the concurrent Ulysses observations during sunspot minimum (Neugebauer *et al.*, 1998). For the north pole when the data are even noisier, a simple 1D interpolation yields even worse result. The smoothing scheme used in the new method has prevented this unreasonable

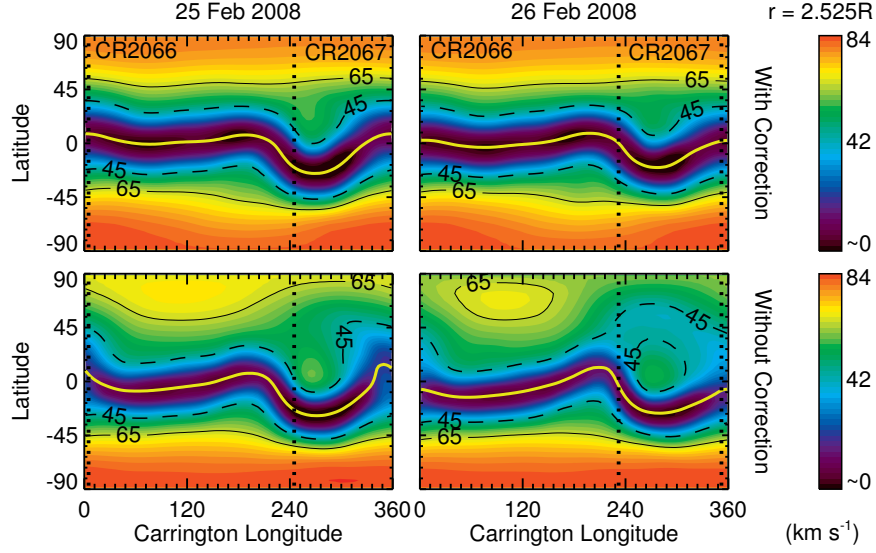


Figure 3.6: Solar wind speed distribution at the height of $2.525 R_{\odot}$ on Feb 25th and 26th, 2008, derived from a daily MHD simulation with MDI daily-updated synoptic maps as input. The top row is computed using maps with new interpolation. Maps used for the bottom row are not corrected. The Carrington longitude of the central meridian passage (CMP) for these two days are 305° for and 292° respectively. The leading edge of the map is 60° east to the CMP and data within a 120° longitudinal window centered at CMP (between the two dotted lines) is updated daily with new observations. In the speed contours, lines are drawn for values of 45 and 65 to highlight the high speed regions. Due to a few “bad pixels” in the north pole region of the updated data, great changes of the solar wind speed distribution are seen over one day. In addition, the typical high speed solar wind during solar minimum is altogether missing from the North pole.

modeling outcome.

3.4.2 MHD Simulation

The new polar interpolation method also proves to be useful for MHD simulations. In order to study the real-time solar corona conditions, we incorporate the MDI daily-updated synoptic maps into a time-relaxation MHD simulation (Hayashi, 2005; Hayashi, Zhao, and Liu, 2008). For this near real time exercise, the MHD code employs the polytropic assumption with a specific heat ratio of 1.05. This choice of specific heat generally yields lower solar wind speeds than observation, but reproduces realistic stream structures that can be directly compared with observations. The simulation result is sensitive to the input data, thus ideal for this test.

Daily-updated synoptic maps that include the information from the latest magnetograms are used as the inner boundary and the simulation is run on a daily basis (http://sun.stanford.edu/~keiji/daily_mhd/daily_mhd.html). The data are binned from the 360×180 daily-updated MDI

synoptic map to a 72×30 resolution map for MHD computation. Each pixel in the low-resolution map is simply the average of an evenly-spaced 5×6 window in the original map.

We use two sets of synoptic maps as input. The first set is treated with the new interpolation method and then binned to lower resolution. The second set does not have any specific polar field interpolation; if there are missing pixels in the binning window, we simply use the average of existing pixels in that window. Figure 3.6 shows the simulated solar wind velocity at the height of $2.525 R_{\odot}$, for Feb 25 and 26, 2008. The center of each map has been shifted so the left edge is placed at Carrington longitude 0° . The left edge of the original daily map is denoted by the vertical dotted line.

We expect the wind speed distribution to be largely stable over a period of two days. Both poles should produce high speed wind since it is during sunspot minimum phase. However, in Figure 3.6, the lower row that with no polar field correction contradicts the postulate. The poorly observed north pole produces solar wind that is much slower than the south pole, and the predicted speed distribution changes drastically from one day to the next. Detailed analysis suggests that the noisy polar field data on the upper-left edge of the input map are responsible for this result. The location of the inferred current sheet (zero radial field) also shifts due to the changing of flux imbalance from the two poles. In this occasion, the upper row that utilizes the new method gives a far more reasonable answer.

3.5 Summary

We describe a new polar field interpolation scheme for the MDI synoptic maps. The method relies on well-observed polar data during September/March each year to estimate the time-varying large-scale polar field and then merges the synthesized field back smoothly into the original map. The same procedure is applied to both poles and to all maps, so the noise level at the poles remains comparable over time. For global models such as the WSA model and daily MHD simulation, the method is shown to improve results when compared with some existing methods.

MDI full rotation synoptic maps with polar field corrected in this fashion are available as a standard product on the MDI website. We plan to apply the same method to the Helioseismic and Magnetic Imager (HMI) synoptic maps, after we study and compare the data in detail with MDI.

* The content of this Chapter, including all figures, is adapted from Sun *et al.* (2011) with kind permission of Springer Science and Business Media. I adapted the extrapolation code, performed the modeling and all the analysis. Dr. X. Zhao provided the original PFSS extrapolation code. Dr. C. N. Arge provided the kinetic solar wind propagation code. Dr. K. Hayashi performed the MHD simulation in Section 3.4.

Chapter 4

Large-Scale Magnetic Field and Solar Wind During Solar Cycle 23

4.1 Introduction

The large-scale solar wind and coronal field structures respond directly to the solar surface magnetic condition (for a recent review, see [Zurbuchen, 2007](#)). Large regions with unipolar field, known as coronal holes (CHs), maintain an open configuration, from which the fast solar wind accelerates into the heliosphere. Contrary to that, large closed field configurations appear as the bright coronal streamers, above which the heliospheric current sheet (HCS) lies between oppositely directed open field. Slow solar wind is thought to emit from the interface between the open and close fields.

The 11-year solar activity cycle modulates the open flux and the solar wind. This is reflected in the changes of the interplanetary magnetic field (IMF) polarity and solar wind (SW) speed structures and their source locations. During the minimum phase, the coronal field is dipole-like, with smaller contributions only affecting the equatorial regions ([Hoeksema, Wilcox, and Scherrer, 1982, 1983](#)). The heliosphere is dominated by fast solar wind flows from the polar CHs (e.g. [Balogh *et al.*, 1995](#); [Neugebauer *et al.*, 1998](#)). SW near the equator is slower and more variable. During the maximum phase, variable wind components are observed at all latitudes, with slow wind coming from smaller low-latitude CHs as well as the edge of active regions (ARs) (e.g. [Neugebauer *et al.*, 2002](#); [Sakao *et al.*, 2007](#)). Eruptive events produce ejecta fitfully, from both ARs and quiet Sun regions that interact with the background SW.

The recent solar minimum phase (roughly 2007-2009) is the weakest and the longest during the space era. The sunspot number (SSN) was low; very few explosive events took place on the Sun. At the same time, a series of long-lived, low-latitude CHs introduced recurring high speed SW

streams in the ecliptic. The weakened heliospheric magnetic field allowed more high-energy cosmic ray to enter the heliosphere. This peculiar minimum has been extensively studied, in terms of its coronal and heliospheric manifestations (e.g. [Smith and Balogh, 2008](#); [Thompson *et al.*, 2011a](#)), its phenomenological magnetic causes (e.g. [Sun, Liu, and Hoeksema, 2008](#); [Wang, Robbrecht, and Sheeley, 2009](#); [Zhao and Fisk, 2011](#)), and its subsurface origins (e.g. [Hathaway and Rightmire, 2010](#); [Nandy, Muñoz-Jaramillo, and Martens, 2011](#)).

In this chapter, we infer from the MDI data archive 15 years (1996–2010) of steady-state solar wind and coronal field structures based on the PFSS and the WSA model. The procedures have been optimized for the MDI data set, as described and evaluated in Chapter 2. This long-running data set enables us to study the secular evolution of the HCS, the solar wind source location, the SW speed, and the IMF polarity during different sunspot cycle phases. We briefly discuss the magnetic nature of the recent minimum, and its implications on the coronal modeling.

4.2 Global Magnetic Field and Coronal Structure Near the Sun

4.2.1 Minimum vs. Maximum Phase

The global structure of the solar wind and the coronal field evolves significantly from the activity minimum phase to the maximum. In Figure 4.1, we show the modeling results of CR 1912 (August 1996) as an example for the minimum phase, and CR 1963 (May 2000) for the maximum. The computed polarity inversion line at the source surface traces the base of the HCS; the flux-tube footpoints indicate the solar wind source; the WSA empirical function provides a global map of the initial SW speed near the Sun. We juxtapose relevant observations for comparison.

- *Heliospheric current sheet.* During CR 1912, the HCS is relatively flat except for the excursion related to a nearby AR (Figure 4.1(a)). It is overall displaced southward from the equator, which is common during the recent sunspot cycles due to the different activity levels of the north and south hemispheres (e.g. [Zhao, Hoeksema, and Scherrer, 2005](#); [Wang and Robbrecht, 2011](#), and references therein). In the corona, the electrons are highly concentrated near the HCS, which appear bright in white light coronagraph due to Thompson scattering. To compare the inferred HCS location with coronal observation, we simulate the total corona intensity assuming a higher electron density near the zero radial field isosurface ([Wang *et al.*, 1997, 2007b](#)). The simulated east-limb intensity synoptic map at $2.5R_{\odot}$ features a bright belt near the HCS, discontinued at 240° – 300° longitude due to the projection effect. It well resembles

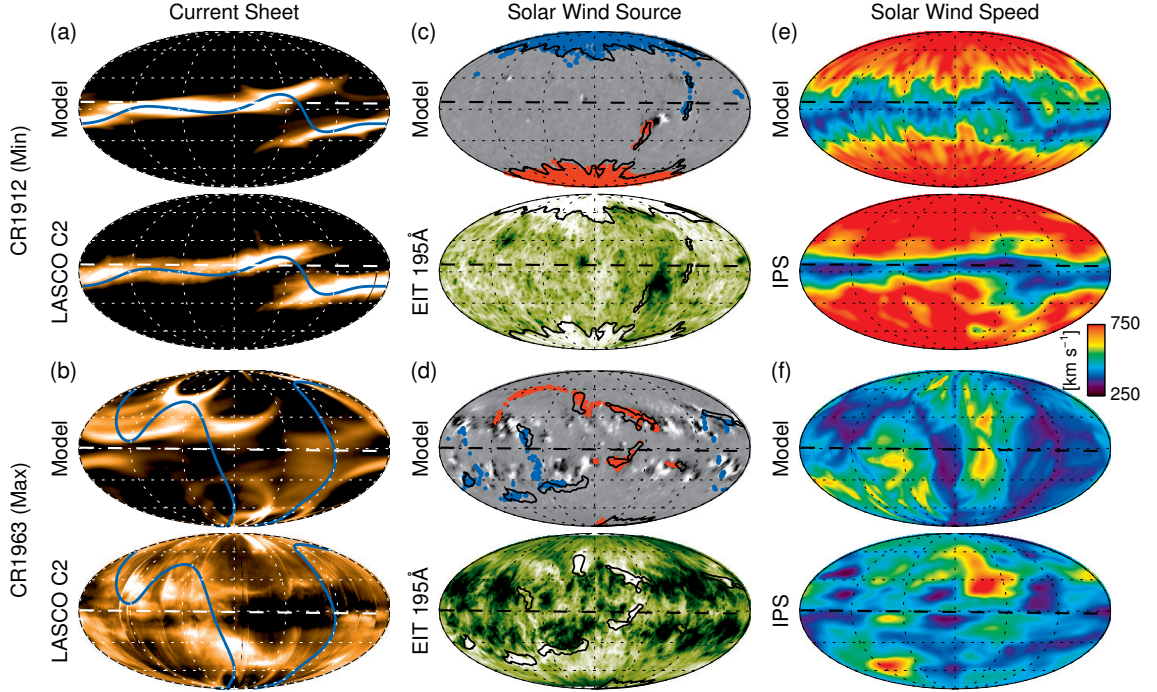


Figure 4.1: Examples of various global modeling results and observations, during the sunspot minimum (CR 1912) and maximum (CR 1963) phase. All panels show synoptic view of the Sun over 1 CR in Mollweide projection. The horizontal dashed line near the equator is the sub-earth line. (a) Simulated coronal streamer structures on the east limb at $2.5R_{\odot}$ (top) and LASCO C2 observation (bottom) for CR 1912. Thick blue curve show the computed polarity inversion line at $2.5R_{\odot}$. (b) Same as (a), for CR 1963. (c) Derived open field footpoints on the photosphere as solar wind source location plotted on synoptic map (top) and EIT 195 Å observation in reversed contrast (bottom) for CR 1912. White (black) are for positive (negative) photospheric field, clipped at 50G. Blue (red) color in the top panel indicates positive (negative) magnetic polarity at the footpoint. Black contours are the CH boundaries derived from the NSO KPVT He I observation. (d) Same as (c), for CR 1963. (e) Inferred SW speed at $2.5R_{\odot}$ (top) and IPS observation (bottom) for CR 1912. Speed is clipped at 750 km s^{-1} . (f) Same as (e), for CR 1963.

the observation by the LASCO C2 instrument aboard *SOHO*. During CR 1963, on the other hand, the HCS becomes highly tilted, almost north-south oriented, and extends all the way to the south pole (Figure 4.1(b)). The simulated intensity matches the observation poorly. This suggests a more dynamic corona with frequent intensity enhancement away from the current sheet.

- *Solar wind source.* During CR 1912, the open field polar regions extend down to almost 60° latitude (i.e. “polar cap”). These polar CHs are the major source of solar wind (Figure 4.1(c)); their size and location agree well with the extreme ultraviolet (EUV) observation by the EIT instrument on *SOHO* (bright in the negative 195 Å images). Additional smaller source regions

exist at lower-latitudes in both hemisphere, and are corroborated by the CH boundaries derived from the *NSO* KPVT He I 10830 Å observation (black contours). In contrast, the solar wind sources during CR 1963 are clustered in a series of smaller mid- and low-latitude regions (Figure 4.1(d)). The polar CHs have almost disappeared. Only about half of the modeled flux tubes trace back to the observed He I CHs; some of them map to the edge of ARs (dark patch in the negative 195 Å image).

- *Global solar wind speed.* The SW speed structure during CR 1912 is well organized and clearly bi-modal (Figure 4.1(e)). Fast wind (above 600 km s^{-1}) from the polar region occupies most latitudes, while a narrow band of slow wind lies near the ecliptic. A sharp latitudinal speed gradient exists between these two components. The speed distribution from the *interplanetary scintillations* (*IPS*) measurements (e.g. Kojima and Kakinuma, 1990; Kojima *et al.*, 1998) supports this description, and the slow wind belt appears even narrower. This picture changes completely during CR 1963, when the fast polar streams completely disappear. More variable slow streams become dominant, with few intermittent fast streams from larger low-latitude CHs (Figure 4.1(f)). This is also qualitatively confirmed by the *IPS* observation.

4.2.2 The Secular Evolution

We illustrate the Sun’s secular evolution in Figure 4.2 with a selection of 9 CRs spanning 15 years. Between the distinctive minimum (e.g. CR 1912) and maximum (e.g. CR 1960), the rising activity phase features shrinking polar caps and a warping/tilting HCS (e.g. CR 1936). These processes are reversed for the declining phase (e.g. CR2008, CR2032).

Figure 4.3 further summarizes the modeling results and relevant observations. We highlight a few aspects below.

- *Polarity reversal.* The modeled HCS becomes increasingly tilted during the rising phase and reaches its maximum in mid-2000 (Figure 4.3(d)); the global dipole ($l = 1$ component) reverses sign at about the same time (reaches 0 in Figure 4.3(d)). Both precede the peak time of the sunspot number (SSN) by only a few months (Figure 4.3(a)). This indicates the flux of the new cycle has effectively canceled out that from the old cycle. The net new flux is transported poleward through preferential supergranular diffusion and meridional circulation (e.g. Wang, Nash, and Sheeley, 1989b), forming surge-like flux patterns along the way (Figure 4.3(g)). This reversal is not immediately manifested in the polar region (Figure 4.3(b)) measured from

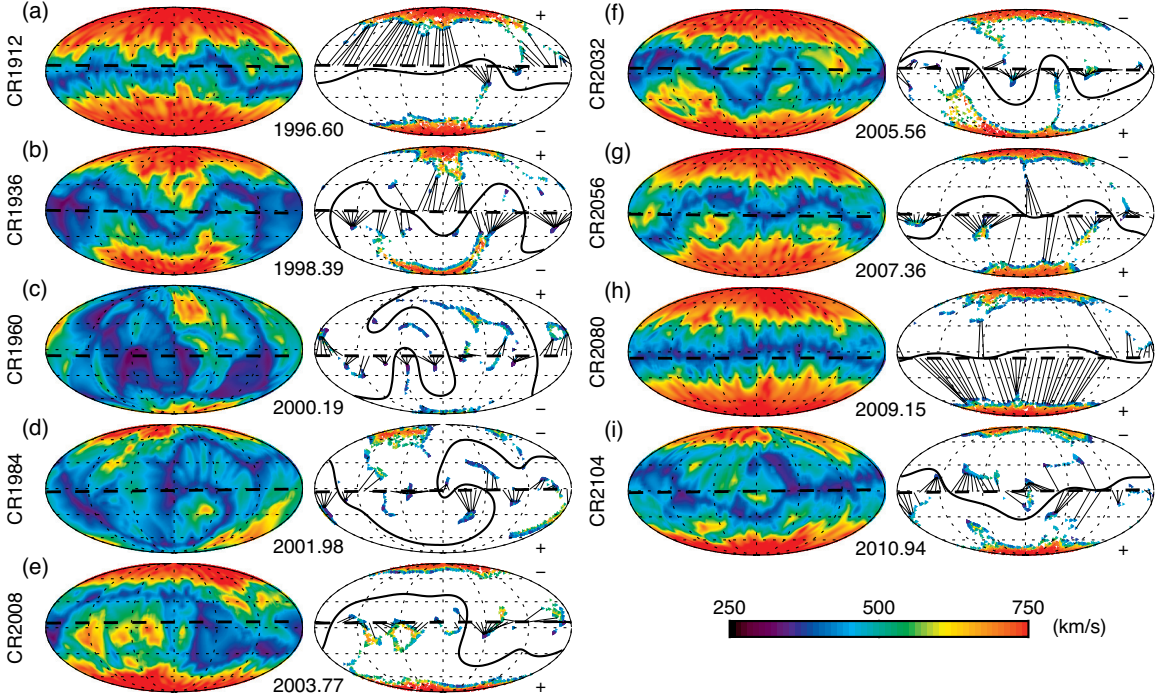


Figure 4.2: Modeled global SW speed distribution (left); solar wind source regions and HCS on synoptic map (right). Adjacent maps are about 24 CRs (1.8 years) apart and represent different phases of cycle 23. In each row, the CR numbers are marked on the right; the time is marked in unit of year. All panels are shown in Mollweide projection. In each map, the horizontal dashed line tracks the sub-earth points. In the right column, colored areas show the open field footpoint locations and their associated SW speed. A series of straight solid lines show the connectivity between sub-earth points and their photosphere origins. The thick curved line shows the modeled HCS location. The plus and minus signs on the right show the polarity of mean polar field above 75° . (See accompanying movie for all available CRs.)

70° latitude and above: it takes another 0.5–1 year for them to be neutralized in 2001. The north polar field regains its strength much faster after the reversal, owing to a strong incoming flux “surge” near 2002 (Figure 4.3(g)). As a consequence, both the polar CH (Figure 4.2(d)) and the fast solar wind streams (Figure 4.3(h)) reappears earlier in the north.

- *Evolving open flux source.* The latitudinal distribution of the open flux sources displays a dichotomy during the minimum phase (Figure 4.3(e)). Above 60° latitude, computed large polar CHs occupies about 10% of the solar surface in 1996, which situates between the values determined from EUV ($\sim 8\%$) (Kirk *et al.*, 2009) and He I ($\sim 15\%$) (Harvey and Recely, 2002) observations. On the other hand, open field regions below 60° latitude are small and scarce, accounting for at most 2% of the surface area. Fast solar wind emits almost exclusively from these polar CHs (e.g. Figure 4.2(a)). Approaching maximum, the polar CHs quickly shrink.

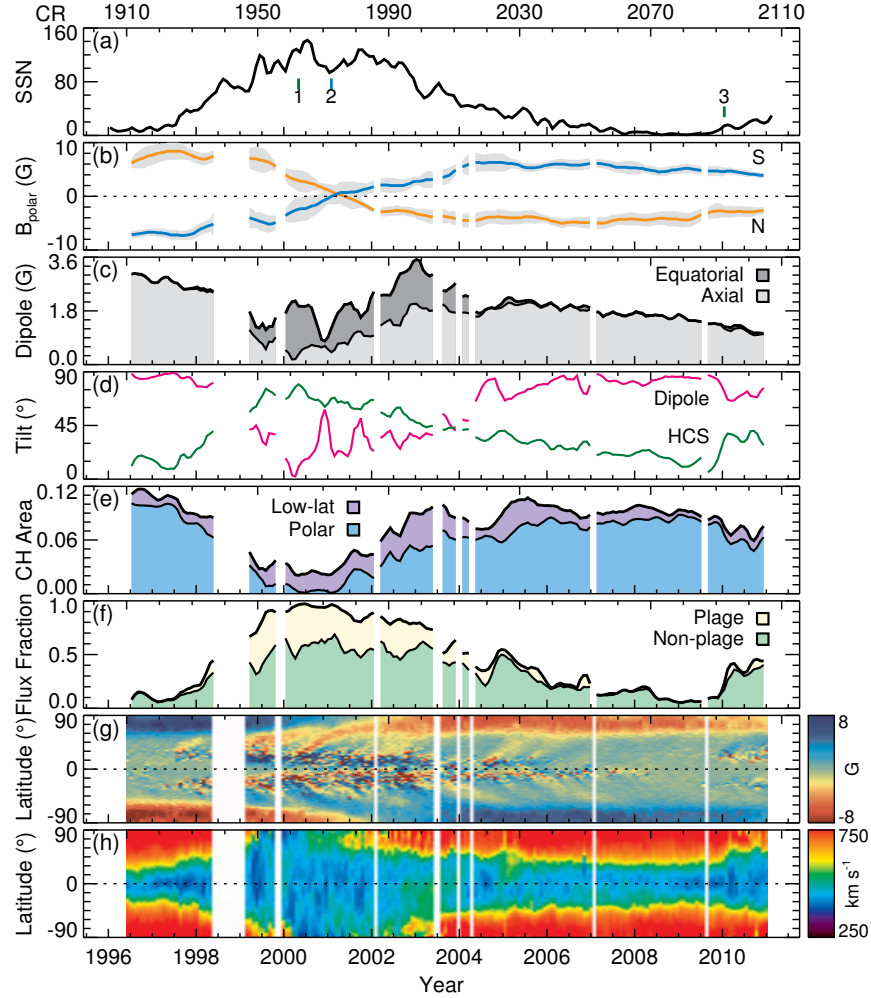


Figure 4.3: Modeling results and observations of the Sun’s secular evolution from 1996 to 2010. (a) Three-month running averaged sunspot number (SSN). The numbers 1, 2 and 3 mark the time of maximum HCS tilt, polar field reversal time, and the recent onset of the HCS tilt increase. (b) Averaged polar flux density for 70° latitude and above. A 20 nHz low-pass filter is applied to smooth the variations due to the change of viewing angle. Grey bands indicated the standard deviation of measurements within a one-year window. (c) Photospheric dipole strength proxy ($l = 1$ spherical harmonic coefficients). The upper curve shows the total; the lower (shaded light grey) shows the axial component ($m = 0$); the difference (shaded dark grey) shows the equatorial component ($m = \pm 1$). (d) Tilt angle of the HCS, defined as the mean of its maximum north and south latitudinal extent (green); tilt of the photospheric dipole ($l = 1$), defined as the latitude of the magnetic north pole (pink). (e) Fractional area of the computed open field regions. The upper curve shows the total; the lower (shaded cyan) represents those above 60° latitude; the difference (shaded purple) represents those from below 60° . (f) Fraction of the open flux from sources below 60° latitude. The upper curve shows the total; the lower (shaded green) indicates the amount that originates from regions where $|B_r| < 100$ G; the difference (shaded yellow) is for $|B_r| \geq 100$ G, which we define as the magnetic “plage”. (g) Butterfly diagram of the photospheric field, constructed by zonally averaging the synoptic maps of each CR and stack them in time. (h) Similar to (g), for modeled solar wind speed. Blank stripes indicate CRs with data gap. For panels (c)–(f), we adopt a 1° resolution input map and truncate the harmonics at $l = 180$. A 3-CR running average is applied to panels (c)–(f).

The low-latitude CHs often form in the remnant of the decayed ARs, which appear slanted due to the differential rotation (Figure 4.2(c)). They now appear in higher latitudes; their total area increases to about 3%–4%. The band of slow wind correspondingly becomes broader (Figure 4.3(h)). A survey of the open flux origin (Figure 4.2(f)) shows that a significant portion ($\sim 40\%$) of the total flux comes from the magnetic plage region (defined as $|B_r| > 100$ G at 1° resolution here) (c.f. Schrijver and DeRosa, 2003).

- *Deep minimum and the onset of new cycle.* The minimum phase of cycle 23/24 is unusually long. The sunspot numbers are low, the polar field is almost half of the previous. Compare CR 1912 and CR2056 whose SSNs are similar (Figure 4.2(a) and (g)), we see the recent minimum has a more warped HCS, smaller polar caps, larger low-latitude CHs, more low-latitude open flux, and recurring fast solar wind streams at 1 AU (e.g. Wang, Robbrecht, and Sheeley, 2009; Gibson *et al.*, 2011). All of these phenomena are natural consequences of the declining dipole strength (e.g. Sun, Liu, and Hoeksema, 2008; Lee *et al.*, 2009; Luhmann *et al.*, 2009), which reaches its maximum strength during 2005 and has been decreasing since (Figure 4.3(c)). Around 2010, the sunspot activity restarts, suggesting the onset of the new cycle. The polar CHs quickly recede, especially in the north. Low-latitude open flux accounts for $\sim 40\%$ of total by the end of 2010, compare to below 10% a year earlier. The tilt of HCS also increases from $\sim 5^\circ$ to $\sim 40^\circ$ within a year. We will discuss this topic more in Section 4.4.

4.3 SW Speed and IMF Polarity Near Earth

Using the WSA model optimized for the MDI data set (Chapter 2), we make a time series of 3-day advanced SW speed prediction at the L1 point, which can be compared against the in situ observations. An example of the prediction is shown earlier in Figure 2.3.

We now study the large scale, characteristic (recurring) structures of the SW streams. In Figure 4.4(a), daily average of the predicted SW speed is shown as a single pixel, colored according to their speed, red being the highest. The pixels are aligned 27 days per row, in the format of the “Bartel stack-plot”. In this format, recurring fast streams stand out as yellow and red blocks in the low speed blue background. The width of the block structure is proportional to the size of the stream; the vertical extension indicates their life time. Transient flows that last less than one day are smoothed over in this plot. Transient flows longer than 1 day can also be distinguished since they usually do not reappear in the next rotation, thus the pattern do not extend vertically. Figure 4.4(b) shows the OMNI data in the same format.

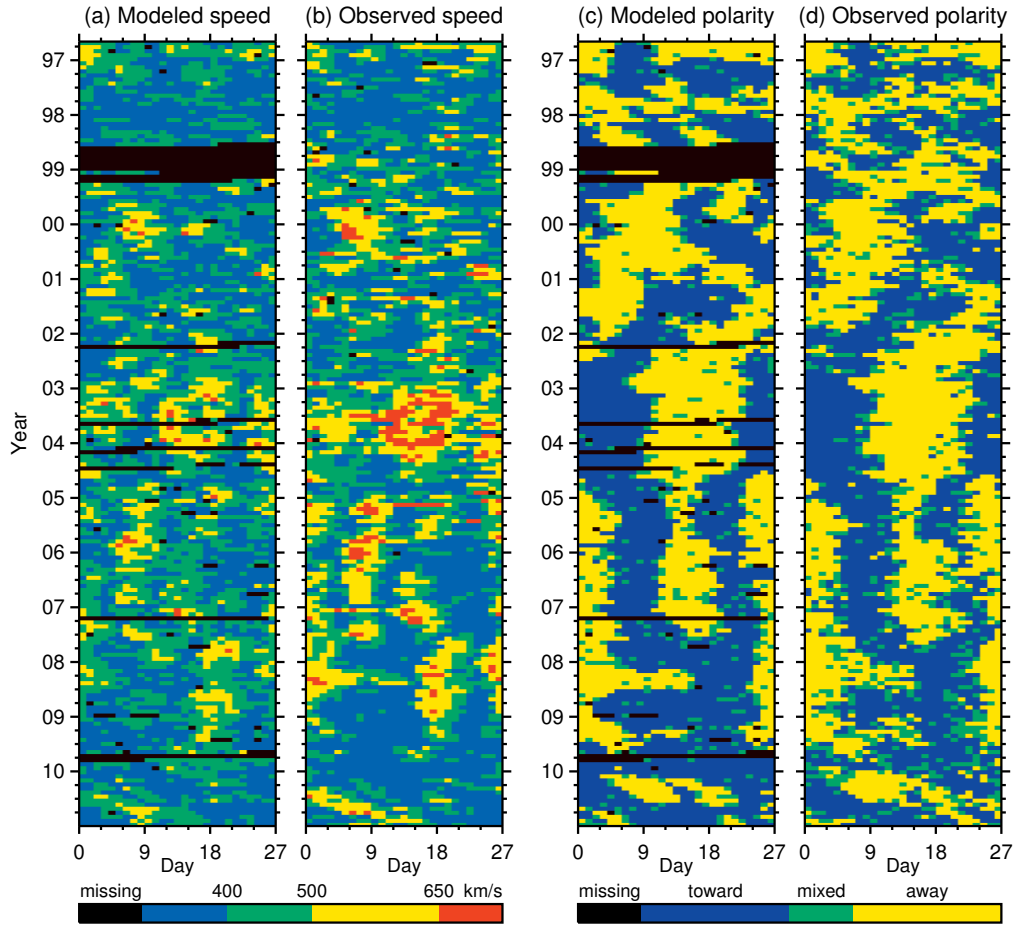


Figure 4.4: SW speed and IMF polarity prediction and observation at L1 in Bartel stack-plot form. (a) Predicted daily-averaged SW speed shown as individual pixels, 27 days per row. Red and yellow indicates high speeds; black is for missing data. (b) Observed SW speed from OMNI data. (c) Predicted IMF polarity structure. Yellow/blue indicates away/toward HCS sector. (d) Observed IMF polarity.

One striking contrast is that the abundance of high speed streams during the recent minimum (e.g. 2006–2009), and the lack of during the past minimum (e.g. 1996–1998). Many large low-latitude CHs appeared as the origin of such fast streams (Abramenko *et al.*, 2010; Wang *et al.*, 2010), as shown in Figure 2.6 and Figures 4.2(f) and (g). This phenomenon has been studied and correlated to the overall decrease in the global dipole field (e.g. Sun, Liu, and Hoeksema, 2008; Lee *et al.*, 2009; Luhmann *et al.*, 2009). Another feature is that the abundance of long-lived fast streams reached its peak during the declining phase (2003–2004). The streams maximum phase (2000–2001) seems to be less organized and short-lived, which illustrates the effect of transient ejecta.

The overall patterns of predicted SW speed structure qualitatively agree with observation. However, it is obvious the peak speed of predicted fast wind is too low. On the other hand, prediction of the slow background wind can sometimes be too high, reflecting the overall “flatness” of the predicted speed. As discussed in Section 2.4 it is partly due to the optimization scheme based on statistical metrics, as suggested by Owens *et al.* (2005).

Figure 4.4(c) and (d) show the HCS sector structure (i.e. intervals with alternating IMF polarity divided by HCS) of solar cycle 23. During the minimum phase 22/23, the sector boundary is not well defined due to the flatness of HCS. Multiple crossovers between the HCS and the ecliptic causes an unstable count of sector numbers, usually 4 or more. A simple 2-sector structure started to form during the late maximum phase (2002) as a result of the large tilt of the HCS. During the long declining phase, a 4-sector structure formed (2004). The warp of the HCS persisted, but the dipole field started to grow and forced to reduce the tilt HCS. As a result, multiple crossovers appeared again. The 4-sector structure persisted till the minimum phase (2007), when the dipole outgrew the higher order field components, but not strong enough to dominate like the previous minimum (e.g. Sun, Liu, and Hoeksema, 2008; Wang, Robbrecht, and Sheeley, 2009). An alternation between 2 and 4 sectors were seen.

The prediction captures most large-scale structures present in observation. The wrong prediction of IMF polarity usually occurs at the sector boundary, i.e., the crossover between the in-situ spacecraft and the HCS. Possible errors may arise from, for example, the polar field estimation, the new flux emerges on the Sun, errors in field extrapolations, etc. Some of them were discussed in Section 2.4. Errors in IMF polarity prediction can also originate from the inaccurate speed prediction that gives the wrong arrival time. However, this cause seems less important. For example, a 20% error in the speed will lead to less than a day’s difference of the arrival time for slow wind (300 km s^{-1}) and ~ 0.5 day’s difference for fast wind (600 km s^{-1}). They cannot fully account for the wrong predictions that last for over a day.

4.4 On the Peculiar Solar Minimum Phase Between Cycles 23-24

4.4.1 Weakened Solar Magnetic Field and Its Consequences

As is evident from Figure 4.3(b), the polar mean field is much weaker during the recent solar minimum phase. In fact, it is the weakest amongst the recent four minima. This is obvious from Figure 4.5(b), which is derived from the WSO synoptic map series from 1976 to 2008. As expected,

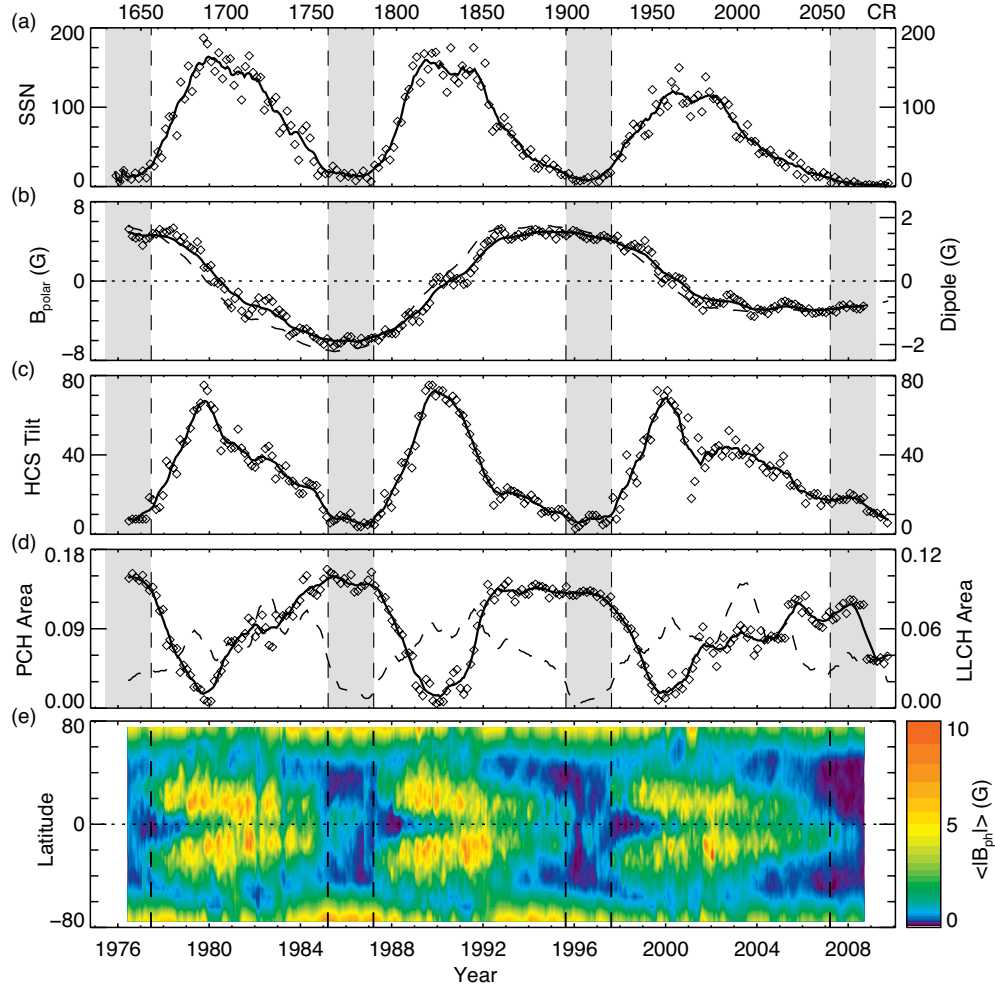


Figure 4.5: Various observation and modeling result on the large scale solar magnetic field from 1976 to 2008 based on WSO synoptic maps. The four minimum activity phases are denoted by straight gray bands, each lasting about 2 years. (a) Averaged sunspot number. Diamonds are monthly mean plotted for every other month; thick line is the yearly running average. (b) Polar field, mean of the north (B_N) and negative south (B_S) value $((B_N - B_S)/2)$ and the axial dipole field strength at the pole. Diamonds are 2 CR average of the polar field (same in panels (c) and (d)). Solid line is the low-pass filtered (20 nHz, or 1.5 year period) polar field; dotted line is the low-pass filtered ddipole field. (c) Modeled maximum heliospheric current sheet tilt angle. Solid line is the yearly running average. (d) Modeled polar (solid line) and mid-low latitude (dashed line) fractional coronal hole area. (e) Zonally averaged photospheric field strength $|B|$.

the tilt of the HCS is the largest (Figure 4.5(c)); the polar CH area is the smallest; the lower-latitude area is the largest (Figure 4.5(d)). A zonal average of the photospheric field shows that the over all photospheric field has been reduced (Figure 4.5(e)). A histogram of the photospheric field distribution clearly shows the trend (Figure 4.6(a)). The strength of IMF measured at L1 is reduced as well (Figure 4.6(b)).

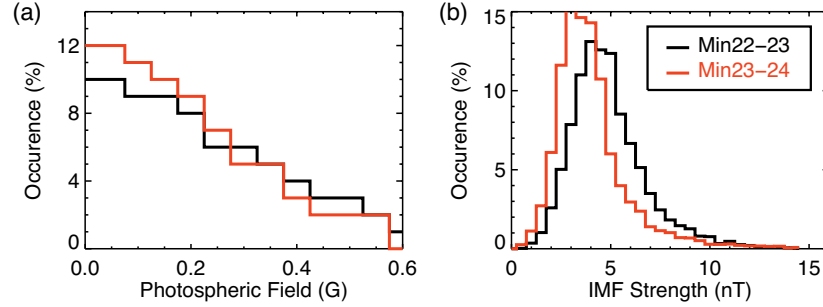


Figure 4.6: A comparison of of the photospheric field and IMF strength for two minima. (a) Histogram of weak photospheric field from WSO magnetic synoptic map with $\sim 5^\circ$ resolution. The red is for minimum between cycles 22 and 23, the red is for minimum 23/24. (b) Histogram of IMF strength at L1 from the OMNI data set.

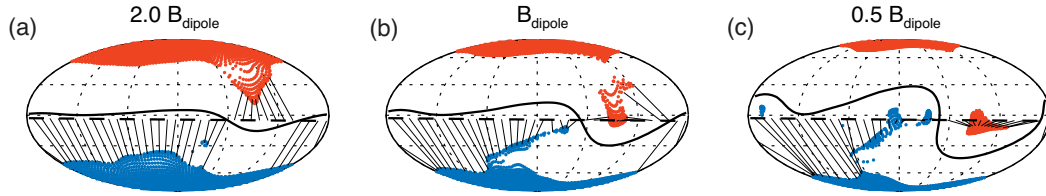


Figure 4.7: Modeled coronal structure of CR2069 with different dipole component. In each panel, the colored regions show the open field footpoints (blue indicating positive polarity, red negative); the thick curve indicate the HCS; the thin lines link the sampled subearth points to their source locations. (a) Result with doubled dipole field. (b) Result from the original map. (c) Result with halved dipole field.

The observed coronal/heliospheric features can be explained by: i) a reduction of the overall magnetic field; ii) a reduction of the relative strength of the axial dipole field. The latter resulted in changes of CH size, SW stream patterns, as well as HCS structures. We demonstrate this by modeling coronal field for CR2069 with inputs that differ only by their dipole field strength. In Figure 4.7(a), the artificial synoptic map from WSO with double the observed dipole strength leads to a much flatter HCS, compared with the real Sun case in panel (b). The polar CH becomes much larger: the northern low-latitude CH in panel (b) merged with the northern polar CH, and the prolonged, southern CH extension disappeared. The in-ecliptic SW now all maps to the polar CHs. On the contrary, the input with half the dipole strength in panel (c) leads to a much more warped HCS. Polar CHs shrink drastically. Low-latitude CHs abound.

4.4.2 Implications for Field Extrapolation Models

The “source surface” concept, first introduced by [Schatten, Wilcox, and Ness \(1969\)](#) and [Altschuler and Newkirk \(1969\)](#), adds a convenient geometrical constraint to the field to simulate observation. The field remains current-free below the source surface, but current is needed above it to maintain the radial direction of the field. The argument was that the energy density of the transverse field falls below that of the outflowing plasma in the higher corona, so no large-scale transverse field could be sustained.

The PFSS model is since then widely used to model a variety of coronal and solar wind phenomena. A $2.5R_{\odot}$ source surface height is commonly used, as it faithfully reproduced the IMF polarity pattern of solar cycle 21/22 ([Hoeksema, 1984](#)), and performed equally well for multiple aspects during cycle 22/23 (e.g. [Neugebauer *et al.*, 1998](#); [Luhmann *et al.*, 2002](#); [Schrijver and DeRosa, 2003](#)). However, as the field in the lower corona evolves over a solar cycle, its strength and structure changes greatly. The source surface height may need to be adjusted accordingly to keep its self-consistency and to closely match different observational facts (e.g. [Schatten, Wilcox, and Ness, 1969](#); [Levine, Altschuler, and Harvey, 1977](#); [Wang and Sheeley, 1988](#)).

In a recent work ([Lee *et al.*, 2011](#)), we compared the open flux derived from the PFSS model of the recent two minima. A smaller R_s is needed for the flux to match the observed value for both time periods. This is in agreement with the result from cycle 21 ([Wang and Sheeley, 1988](#)), showing that the PFSS model tends to significantly underestimate the in-ecliptic IMF during solar minima. Although subsequent studies after the Ulysses mission improved the estimated open flux by using the mean from all latitudes, a latitudinal-dependent scaling factor is still needed to overcome the underestimation ([Wang and Sheeley, 1995](#)).

We pick two time periods during the minimum phase 22/23 and 23/24 for the purpose of a more comprehensive comparison using the MDI data. 20 CRs are chosen from each minimum (CR1911-CR1930, CR2063-CR2083). Note that the first time period is the earliest MDI data we have, though it is actually past the real minimum and is partly on the early ascending phase. We then perform the PFSS model with 11 different R_s ’s, evenly spaced from $1.5R_{\odot}$ to $2.5R_{\odot}$. To prepare the observational data for comparison, we perform the ballistic backward mapping on observations in these time periods ([Neugebauer *et al.*, 2002](#)). We choose this over the default forward WSA mapping partly because it is more straightforward and convenient, partly because the empirical function tuned earlier for $R_s = 2.5R_{\odot}$ may not work as well for other R_s ’s. We now discuss the results.

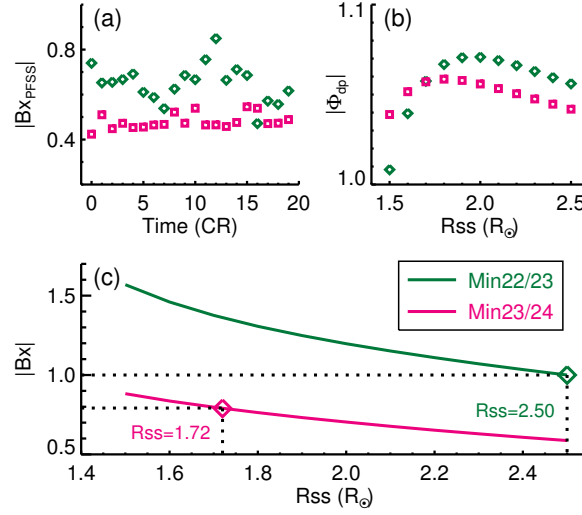


Figure 4.8: Optimal source surface height for minimum phase in terms of total open flux. In all three panels, green represents the mean for CR1911-CR1930 of minimum 22/23; pink shows CR2063-2082 of minimum 23/24. (a) Mean absolute flux density at $2.5R_{\odot}$ scaled to 1AU, normalized by the observed IMF $|B_x|$. A $2.5R_{\odot}$ source surface is used. (b) Ratio of absolute flux density at $2.5R_{\odot}$ derived from vertical dipole field only, and harmonic coefficients truncated at $l = 72$. Various source surface heights are tested. (c) Normalized absolute open flux for two minima derived from different source surface heights. Horizontal dotted lines show the normalized observed IMF $|B_x|$. The recent minimum is about 79% of the last. Vertical dotted lines show the corresponding fitted source surface height.

1. In terms of open flux, a lower source surface at about $1.7R_{\odot}$ is needed to keep the model field strength magnitude at different times *self-consistent*. The inter-instrumental calibration is a pending problem. Different observatories utilize different lines for magnetic field observation, have different instrumental qualities and employ different data reduction schemes. A non-unity scaling factor is common for reconciling magnetograms from two sources, even if they are taken at the same time. In the PFSS model, the coronal field structure won't be affected by this scaling factor. But the inferred value of open flux no longer has an "absolute" meaning. It is more reasonable to require a model to be self-consistent, i.e. keep the scaling factor between the result and the "ground truth" as constant as possible. Following Wang and Sheeley (1995), we use the mean absolute flux density for all solid angles as a proxy of the in-ecliptic IMF strength. The ratio between the modeled open flux with $2.5R_{\odot}$ and observation is plotted in Figure 4.8(a) for each CR. The result differs significantly for two minima, one averages at about 0.6, the other consistently at about 0.4. This obviously deviates from our hope to keep the model "self-consistent" over time. In Figure 4.8(c), we plotted the open flux derived from all trial R_s 's. The IMF of the recent minimum scales to about 79% of the past one for the 20 CRs

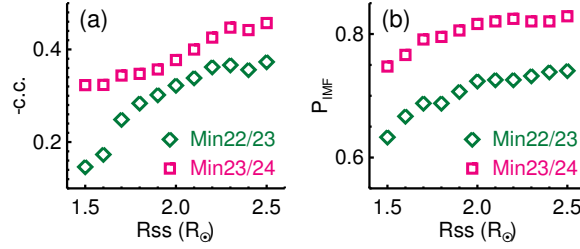


Figure 4.9: Optimal source surface height in terms of SWS and IMF polarity prediction. The same 20-CR time series as Figure 4.8 are used. The observation is mapped back to the source surface. (a) Negative correlation coefficient between computed logarithm of FTE $\log_{10} f_s$ and the logarithm of the observed SWS $\log_{10} v$ mapped back to source surface. Resolution is about 4.5 hours. (b) Success rate of IMF prediction from using different source surface height. Resolution is about 1 day.

we choose. This requires a source surface at about $1.7R_{\odot}$, if $2.5R_{\odot}$ is to be used for the past minimum. On a side note, because the open flux is dominated by the dipole component, we may estimate R_s more conveniently. In Figure 4.8(b) we plot the ratio between open flux from vertical dipole only, and from all 72 orders of harmonic decomposition. The overall open flux estimated from vertical dipole is always within 8% for all trial R_s 's. This allows us to use the dipole component (D) decomposed from the photospheric field directly. As the PFSS dipole open flux proportional to D and approximate inversely proportional to R_s , the stipulation that it should also be proportional to IMF strength (B_x) gives:

$$R'_s = R_s(D'/D)/(B'_x/B_x) \quad (4.1)$$

where the variables with primes are the values in question, and all numbers should be taken as the mean of absolute values. For the time periods we choose, the averaged vertical dipole component gives $D'/D = 0.58$ where the prime denotes the current minimum. With $B'_x/B_x = 0.79$ and $R_s = 2.5$, a new source surface of about $1.84R_{\odot}$ can be estimated.

2. To produce the correct CH configurations, a lower source surface is generally needed. More flux becomes open when a lower source surface is chosen. Subsequently, more flux gets mapped to lower latitude, resulting in more larger mid- and low-latitude modeled CHs. We do not show the plots here, but previous studies (Sun, Liu, and Hoeksema, 2008; Lee *et al.*, 2011) show that a $2.5R_{\odot}$ source surface indeed fails to reproduce some of the low latitude coronal features. Smaller R_s usually improves the result, but the optimal value seem to vary from rotation to rotation and the result is hard to quantify.

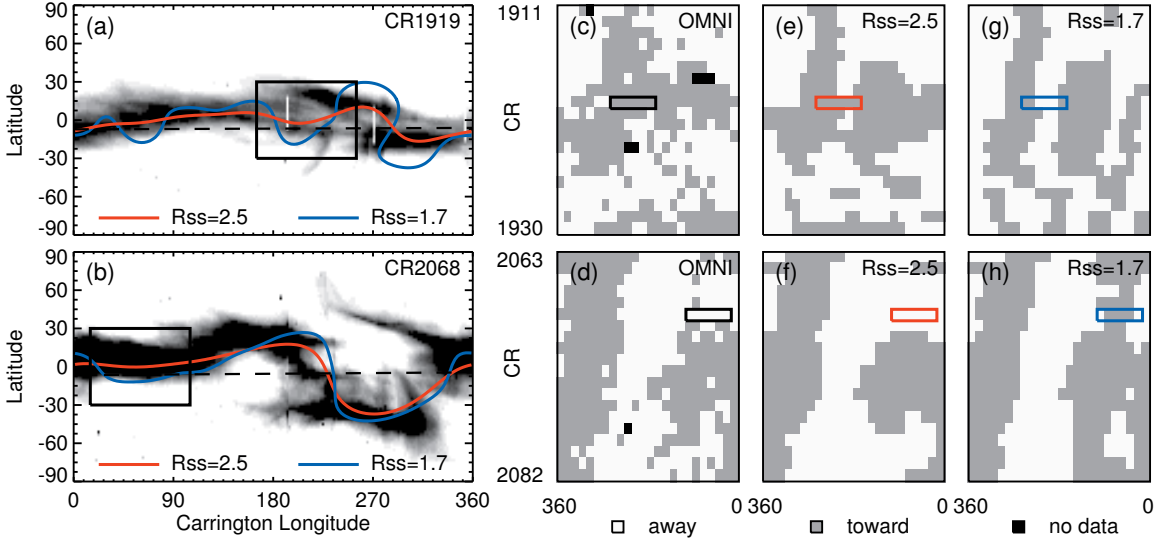


Figure 4.10: Optimal source surface height in terms of HCS shape and IMF polarity prediction. Note in the stack plots time runs from left to right in each row, reverse of the synoptic map. (a) (b) Negative synoptic map of C2 east limb observation at $2.5R_{\odot}$. Overplotted are the modeled HCS location at $2.5R_{\odot}$ with red for $2.5R_{\odot}$ source surface, blue for $1.7R_{\odot}$. The horizontal dashed line is the sub-earth line. The box shows a time period when significance discrepancy is found. (c) (d) Stack plot for IMF polarity, similar to Figure 4.4(c). The parameters are mapped to $2.5R_{\odot}$. The box denotes the same region of discrepancy. (e) (f) Same as (c) (d), for model with $2.5R_{\odot}$ source surface (g) (h) For model with $1.7R_{\odot}$ source surface.

3. In terms of WSA speed prediction, no strong evidence supports a lower source surface. After we map the observed speed v ballistically back to R_s , we perform the PFSS computation to get the corresponding f_s at each sample point. This procedure is done for all 11 trial R_s 's, and the negative value of the correlation coefficient between $\log_{10} v$ and $\log_{10} f_s$ is plotted in Figure 4.9(a). Because v and f_s are inversely correlated, a source surface that produces a negative coefficient with large absolute value is likely a good choice. We note, however, that the correlation increases almost monotonically with R_s for both time periods. The previously chosen $1.7R_{\odot}$ produces a significantly worse correlation than $2.5R_{\odot}$, even for the recent minimum.
4. In terms of the HCS modeling and IMF polarity prediction, no strong evidence supports a lower source surface. In Figure 4.10(a) and (b), we show the negative image of synoptic maps compiled from C2 east-limb observation at the radius of $2.5R_{\odot}$. The dark bands suggest the location of the HCS. We overlay the computed HCS from the $2.5R_{\odot}$ and $1.7R_{\odot}$ source surface as well. For CR1919 (minimum 22/23), result from the $1.7R_{\odot}$ source surface shows too much spatial variation, especially near longitude 270° . For CR2069 (minimum 23/24),

discrepancy can be seen between longitude 0° and 90° for $1.7R_\odot$ too. Stack plots of IMF polarity similar to Figure 4.4(c) are shown in Figure 4.10(c)-(h). A backward mapping of observation is performed before they are compiled into the stack plot. The sign of observed B_x is simply preserved during the ballistic mapping, a simplified approach for the in-ecliptic data than the full Parker spiral solution in Neugebauer *et al.* (2002). The polarity of most sample points within each sector is unlikely to be affected. The box in each stack plot denotes the same region in panel (a) or (b), where discrepancy between model and observation is found. It is obvious that for minimum 22/23, the modeled IMF polarity pattern from a $2.5R_\odot$ source surface resembles observation much better than $1.7R_\odot$. For minimum 23/24, neither excels: they either fail to reproduce the four sector topology ($2.5R_\odot$ for the later half) or mistakenly infer two extra sectors ($1.7R_\odot$ for the early half). A quantitative evaluation of prediction success rate is shown in Figure 4.9(b) for all trial R_s 's. For the previous minimum, $2.5R_\odot$ works best. Several values above $2.0R_\odot$ performs similarly for the recent minimum, and are clearly better than the values below $2.0R_\odot$.

* The content of this Chapter is partly based on Sun, Liu, and Hoeksema (2008) and Sun and Hoeksema (2009). I adapted the extrapolation code, performed the modeling and all the analysis. Dr. X. Zhao provided the original PFSS extrapolation code. Dr. C. N. Arge provided the kinetic solar wind propagation code.

Chapter 5

Evolution of Magnetic Field and Energy in a Major Eruptive Active Region

5.1 Introduction

5.1.1 Energy Storage and Release

Extreme solar activity is powered by magnetic energy (e.g. [Forbes, 2000](#)). Flux emergence and shearing motion introduce strong electric currents and inject energy to the AR corona. Coronal fields are subsequently reconfigured, accumulating large amounts of magnetic free energy. When the overly energetic field gets destabilized, part of its excess energy is released rapidly, with power enough to drive explosive phenomena such as flares and CMEs. During this process, fast, irreversible changes of the photospheric field have been observed as the possible imprint of the coronal activity, including transverse field and magnetic shear increase (e.g. [Wang *et al.*, 1994](#); [Cameron and Sammis, 1999](#); [Wang, 2006](#)) and longitudinal field decrease ([Sudol and Harvey, 2005](#)). [Hudson \(2000\)](#) suggested that the energy loss during the explosion causes “implosion” of the coronal field, which is supported by recent observations ([Ji, Huang, and Wang, 2007](#); [Liu *et al.*, 2009](#); [Liu and Wang, 2010](#)).

This “storage-release” picture provides a scenario successful in explaining many observed phenomena (e.g. [Schrijver, 2009](#)). However, detailed knowledge of the process is still lacking, especially in a quantitative spatially and temporally resolved manner (e.g. [Hudson, 2011](#)). In this sense, uninterrupted, frequent photospheric vector field observation may be crucial to directly monitor the AR’s evolution and provide information on its non-potential nature (e.g. [Schrijver *et al.*, 2005](#)). In addition, field extrapolation models based on the vector boundary may provide valuable diagnostics of the changing coronal field (e.g. [R gnier and Canfield, 2006](#); [Thalmann and Wiegelmann, 2008](#); [Jing *et al.*, 2009](#)). The recently launched *SDO*/HMI therefore presents a unique opportunity to

better understand the AR energetics with its full disk, high resolution and high cadence vector magnetograms.

In this Chapter, we report the evolution of magnetic field and energy in NOAA AR 11158 from 2012 February 12 to 15 using a series of HMI vector magnetograms and a non-linear force-free field (NLFFF) extrapolation (Wiegelmann, 2004). This 5-day uninterrupted, 12-minute cadence data set allows us to study in detail both the *long-term, gradual* evolution (Section 5.2), as well as the *rapid* changes during an X-class flare and CME eruption (Section 5.3). In addition to the HMI data, we employ coronal and chromosphere images taken by the Atmospheric Imaging Assembly (AIA; Lemen *et al.*, 2012) on *SDO* for context and validation of the results.

5.1.2 Data and Modeling

The extrapolation algorithms of NLFFF and PF are described in Chapter 1.3. The magnetic free energy (E_f) can be inferred by subtracting the PF energy (E_P) from the NLFFF energy (E_N), where the energy is computed from the field strength within a certain volume V :

$$E_f = \int_V \frac{B_N^2}{8\pi} dV - \int_V \frac{B_P^2}{8\pi} dV. \quad (5.1)$$

Here the subscripts N and P denote NLFFF and PF respectively. We note that the VFISV inversion scheme for HMI has the magnetic filling factor held at unity, so the reported “magnetic field strength” is essentially area-averaged flux density. In the context of this work, we do not distinguish these two and use the unit Gauss (G) throughout.

We use 600 vector magnetograms of NOAA AR 11158 with a cadence of 12 min, from 2011 February 12 to 16. The images are de-rotated to the disk center and remapped using Lambert equal area projection (Calabretta and Greisen, 2002; Thompson, 2006). The field vectors are transformed to Heliographic coordinates with projection effect removed (Gary and Hagyard, 1990). For direct analysis of the photospheric field, we use full resolution data at about 360 km pix^{-1} (equivalent to $0.5''$ at disk center). For extrapolation, we bin the data to 720 km pix^{-1} (about $1''$) and adopt a computation domain of $216 \times 216 \times 184 \text{ Mm}^3$ ($300 \times 300 \times 256$).

Because the preprocessed bottom boundary emulates the magnetic field in the chromosphere, we assign a uniform altitude of 720 km (1 pixel) to this layer where the field should have become largely force-free (Metcalf *et al.*, 1995) and use it throughout the study. In general, we limit the field of view (FOV) for analysis to the center $184 \times 144 \times 115 \text{ Mm}^3$, covering most of the strong field region. Uncertainties are reported as mean \pm standard deviation unless specified otherwise.

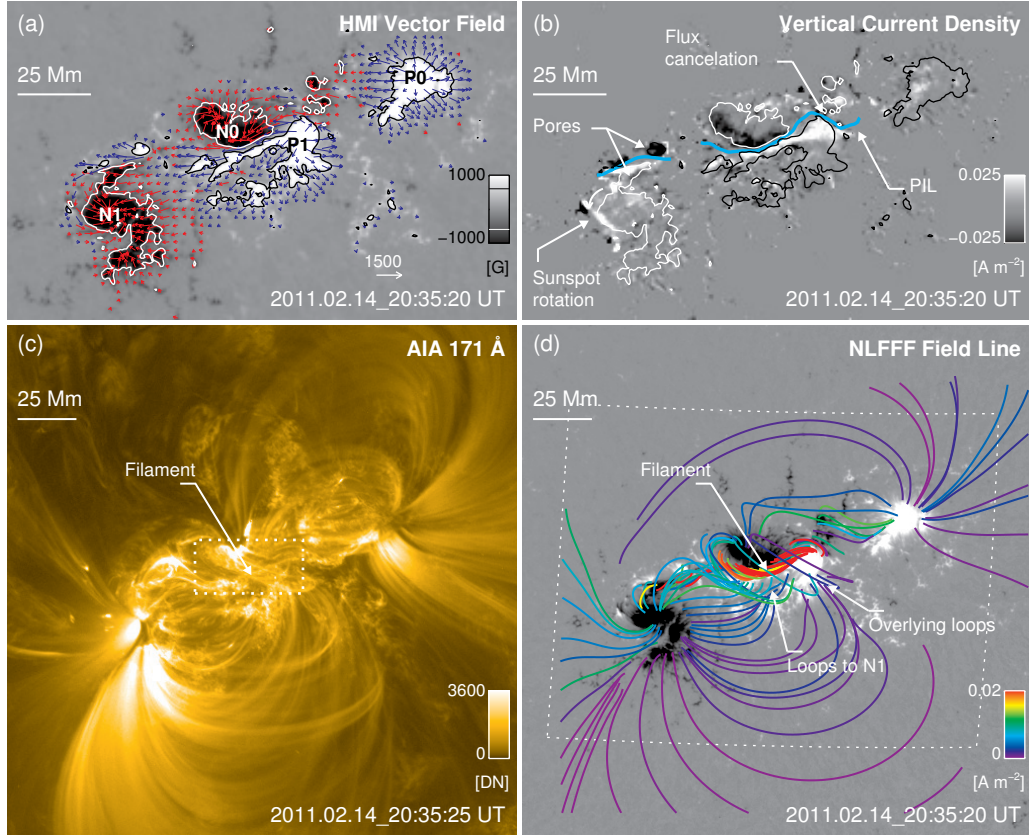


Figure 5.1: Observations and modeling results for 2011 February 14 20:35 UT, about 5 hours before the X-class flare. (a) Remapped HMI vector magnetogram for the center region of AR 11158 as viewed from overhead. Vertical field (B_z) is plotted in the background; blue (red) arrows indicate horizontal field (B_h) with positive (negative) vertical component. Contours are plotted at ± 600 G. (b) Vertical current density (J_z) derived from 5-pixel Gaussian-smoothed vector magnetogram. Contours are for B_z and are identical to (a). Part of the polarity inversion line (PIL) is plotted as thick cyan curve. (c) Image from AIA 171 Å band showing the corona magnetic structures. The dotted box in the center indicates the FOV of Figure 5.2(a). (d) Selected field lines from the NLFFF extrapolation plotted over a cutout from the vertical field map. The lines are color-coded by the vertical current density at their footpoints (see the color bar); red field lines correspond to strong current density. The white dotted box indicate the FOV of (a) and (b). The FOVs of (c) and (d) are identical, about 218×218 Mm², or $302'' \times 302''$.

The extrapolation is performed at 1-h cadence. For the 9 h around the X-class flare the full 12-min cadence is utilized. For convenience, we choose February 15 00:00 UT as time 0 ($T = 0$ h) and use this convention when needed. The AR passed central meridian on early February 14 (-22.2 h). The X2.2 flare (W21S21) started at 1.7 h (February 15 01:44 UT) and peaked at 1.9 h (01:56 UT) in the *GOES* soft X-ray (SXR) flux and was accompanied by a front-side halo CME (Schrijver *et al.*, 2011).

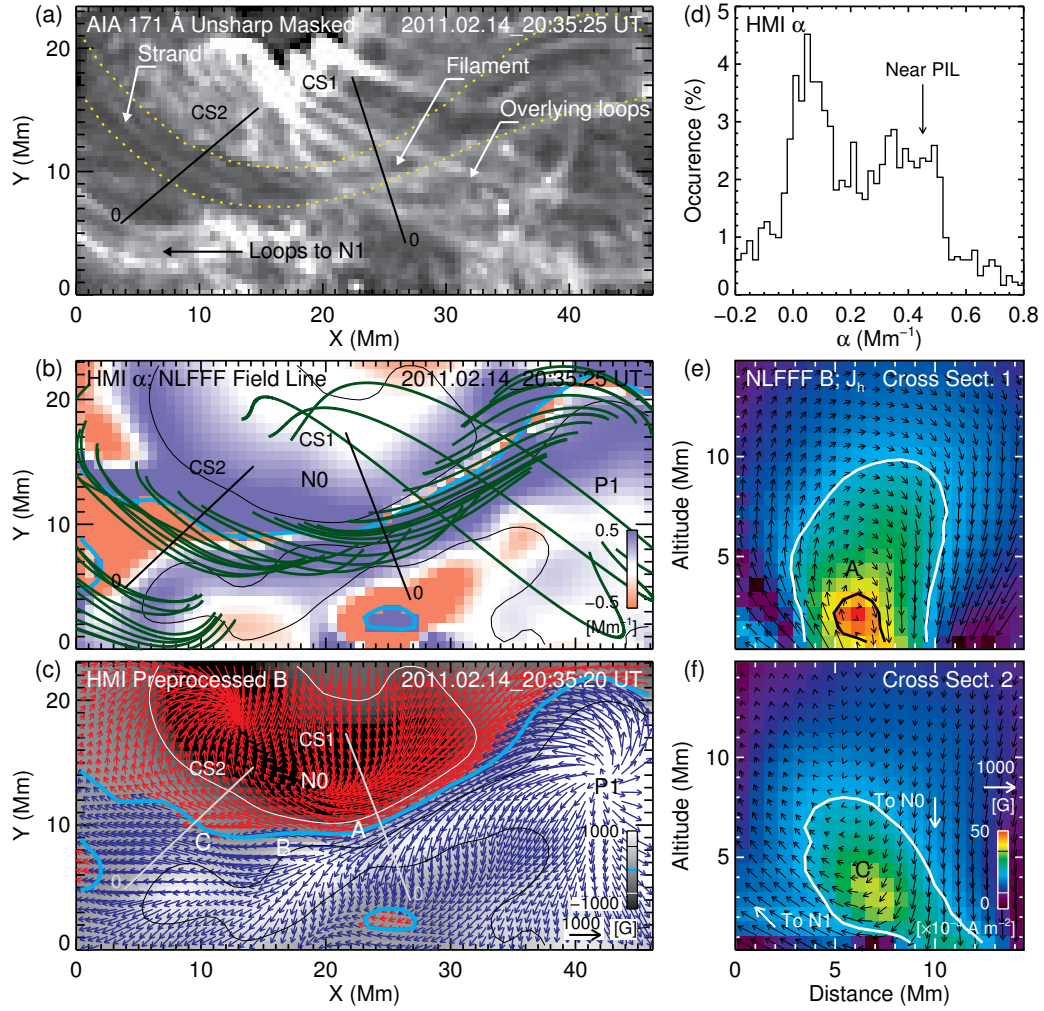


Figure 5.2: Close-up view of the AR core field structure. (a) Unsharp masked AIA 171 Å image. The FOV is denoted by the dotted box in Figure 5.1(c). Two straight lines show the baselines of the vertical cross sections (CS1 and CS2) through the computation domain plotted in panels (e) and (f). Yellow dotted lines are manually drawn to outline the dark S -shaped filament plasma. (b) Selected NLFFF field lines. The torsional parameter, α , derived from preprocessed magnetogram is shown as background. Contours are for $B_z = \pm 600$ G; the cyan line is for the PIL. (c) Preprocessed, remapped HMI vector magnetogram showing the emulated chromospheric field. A, B, and C mark features of interest near the PIL. (d) Histogram of α distribution in the FOV of panel (b). (e) Horizontal current density (J_h) distribution on a vertical cross section (CS1) with projected NLFFF field vectors. The white and black contours are for 10 and 36 mA m^{-2} J_h , respectively. (f) Similar to (e), showing inverse-polarity configuration (CS2).

5.2 Long-Term Evolution

5.2.1 An Illustrative Snapshot

We use a snapshot taken at 20:35 UT on February 14, about 5 h before the X-class flare, to illustrate the magnetic field structures in AR 11158 when it is well developed. It mainly consists of two bipoles (P0/N0 and P1/N1 in Figure 5.1(a), P denoting positive and N negative) that form a complex quadrupolar structure (Schrijver *et al.*, 2011). The total unsigned magnetic flux ($|\Phi|$) is about 2.7×10^{22} Mx and the flux is balanced to within 1%. Vertical field (B_z) in the center of umbra can be as strong as 2600 G. Strong shearing motion exists between P1/N0 as well as amongst a few newly emerged pores. The horizontal field (B_h) in the AR center is largely parallel to the major polarity inversion line (PIL; Figure 5.1(a)), near which strong vertical electric currents (J_z) are present (Figure 5.1(b)). On the south side of the PIL, an elongated strip of positive flux following P1 forms a so-called “magnetic tongue” (e.g. Luoni *et al.*, 2011). Fast sunspot rotation and flux cancellation are also observed.

AIA 171 Å observations of the extreme-ultraviolet (EUV) light emitting plasma roughly outline the coronal magnetic field (Figure 5.1(c)). As a validation of our field extrapolation, we plot selected field lines for comparison and color-code them according to $|J_z|$ at their footpoints (Figure 5.1(d)). Brighter color, such as red, corresponds to stronger $|J_z|$. The modeled field lines with strong currents indicate non-potential structures, and are qualitatively in good agreement with observation. In particular, field lines rooted in the core region (regions near the major PIL) morphologically resemble the observed EUV filament. In contrast, potential-like loops (with weaker current) further away from the center are not well recovered, especially on the north side. A more detailed discussion of the extrapolation can be found in Section 5.4.

A closer look at the core region, summarized in Figure 5.2, reveals a close match between the shape of the filament and the photospheric PIL. There seem to be a few faint strands in the dark filament: NLFFF extrapolation suggests that an ensemble of highly sheared loops thread the plasma. These loops are rooted in P1/N0 inside a narrow strip of strong-current, high- α distribution along the PIL. These loops are typically low-lying, with apexes well below 10 Mm. The broad distribution of photospheric α , mainly from 0 to 0.5 Mm^{-1} (Figure 5.2(d)) necessitates the non-linear treatment for any realistic modeling attempts.

Figure 5.2(e) shows in the colored background the computed horizontal current density (J_h) in a vertical plane perpendicular to the PIL (near “A” in panel c). The projected magnetic field vectors on this cross section rotate around an axis at about 3 Mm altitude; J_h peaks at the same height.

Table 5.1: Estimated field parameters in the filament channel

Parameter ^a	Unit	Cross section ^b	Near axis ^c
A	Mm ²	59.9	4.2
Φ_a	10 ²⁰ Mx	4.87	0.49
$\langle B \rangle$	10 ³ G	0.97 ± 0.27	1.20 ± 0.05
$\langle \gamma \rangle$	degree	26 ± 16	11 ± 8
$\langle J_h \rangle$	mA m ⁻²	19 ± 9	43 ± 5
$\langle \alpha \rangle$	Mm ⁻¹	0.27 ± 0.15	0.46 ± 0.05
$\langle L \rangle$	Mm	29 ± 5	24 ± 3
$\langle \phi \rangle$	Turns	0.64 ± 0.17	0.92 ± 0.17

^a All parameters are estimated from uniformly sampled points on a vertical cross section through the NLFFF extrapolation domain, marked as “CS1” in Figure 5.2. Angle brackets refers to the mean value. The notations are as follows: cross section area A , axial flux Φ_a , field strength B , inclination angle γ , horizontal current density J_h , torsional parameter α , loop length L , twist angle ϕ . The inclination angle is measured with regard to the photosphere, ranging from -90° to 90° with 0° for horizontal field and sign consistent with polarity of B_z . ϕ is divided by 2π to show the estimated number of turns.

^b Values are calculated within the $J_h > 10 \text{ mA m}^{-2}$ contour in Figure 5.2(e) and reported as mean ± standard deviation when applicable.

^c Values are calculated within the $J_h > 36 \text{ mA m}^{-2}$ contour; the centroid is near 3 Mm in height.

Signatures of twisted flux ropes, such as an X-point or a hollow core J_h distribution around its axis (e.g. Bobra, van Ballegoijen, and DeLuca, 2008; Su *et al.*, 2011) are not obvious.

Using AIA 304 Å images (Figure 5.3) where the filament plasma is best defined, we estimate the width of the EUV filament to be about 6 Mm, slightly wider than it appears in the 171 Å band. The apparent length is at least 90 Mm. We choose the 10 mA m^{-2} J_h contour (Figure 5.2(e)) as a proxy for the filament cross section as it encloses a region comparable to the observed filament width. A summary of the estimated field parameters in this region (filament channel) are listed in Table 5.1. In particular, the field strength (B) near the J_h maximum is about 1200 G. This inferred kilogauss field is strong compared with previously modeled plage filaments (e.g. Aulanier and Démoulin, 2003; Guo *et al.*, 2008; Jing *et al.*, 2010) and recent observations (e.g. Kuckein *et al.*, 2009). We estimate the field twist angle as $\phi = \alpha L/2$ (Longcope, Fisher, and Pevtsov, 1998) with L being the loop length and find an average of 0.6 turn, with about 0.9 turn near the J_h maximum.

The field line mapping appears to “bifurcate” near the PIL on the east side (“B” in Figure 5.2(c)). Some EUV loops that originate from the P1 magnetic tongue connect back to N0; others deviate

from the PIL and connect to N1 more than 50 Mm away (Figure 5.1(c) and 5.2(a)). The photospheric α changes sign here as well.

In addition, an interesting “inverse-polarity” configuration (e.g. Mackay *et al.*, 2010, and references therein) exists nearby too, where horizontal field on the photosphere points from the negative vertical polarity side to the positive (near “C” in Figure 5.2(c)). On the vertical cross section shown in Figure 5.2(f), projected field vectors form a “concave-up” configuration. Loops turn upward here or become nearly parallel to the photosphere.

5.2.2 Long-term Evolution of Magnetic Field

We show five representative snapshots of the evolving AR in Figure 5.3. The left and middle columns show B_z and negative AIA 304 Å images, respectively. The right column shows the vertical integration of absolute current density (J) over the lowest 10 Mm as derived from the NLFFF extrapolation. Patterns of strong current concentration may serve as a proxy for non-potential coronal structures (e.g. Schrijver *et al.*, 2008).

Here we highlight a few key features of the magnetic field evolution. For reference, the total unsigned flux $|\Phi|$ and its change rate ($d|\Phi|/dt$) are plotted in Figure 5.4(a); the photospheric unsigned current ($|I|$) in Figure 5.4(b); and the *GOES* soft X-ray (SXR) flux in Figure 5.4(g). An animation of the figure can be found in the online version of Sun *et al.* (2012a).

- The early stage of the AR development (top two rows of Figure 5.3) features fast flux emergence that coincides with the appearance of a pronounced filament. Such fast emergence continues for about 1 day (Figure 5.4(a)) with a rate of several 10^{20} Mx h⁻¹, mainly in the aforementioned two bipoles P0/N0 and P1/N1 (Schrijver *et al.*, 2011). Note that N0 consists of two sunspots, the western one emerges much later. AIA images show frequent brightening as P1 and N0 converge and collide; new magnetic connectivities are being established rapidly in the corona. A filament becomes visible along the PIL within a few hours. Along the PIL, significant electric current injection appears to take place (Figures 5.3(b) and 5.4(b)). During this interval, the net (unbalanced) current in each magnetic polarity also increases drastically, hinting that the newly emerged flux is highly non-potential (Schrijver, 2009).
- After the initial fast flux emergence (third row of Figure 5.3), the sunspot complex develops further with slower flux emergence but lasting strong shearing motion between P1 and N0. The injection of current through the photosphere clearly slows down (Figure 5.4(b)). However, the vertically integrated $|J|$ still increases by about 25% over a period of 40 h, suggesting a net

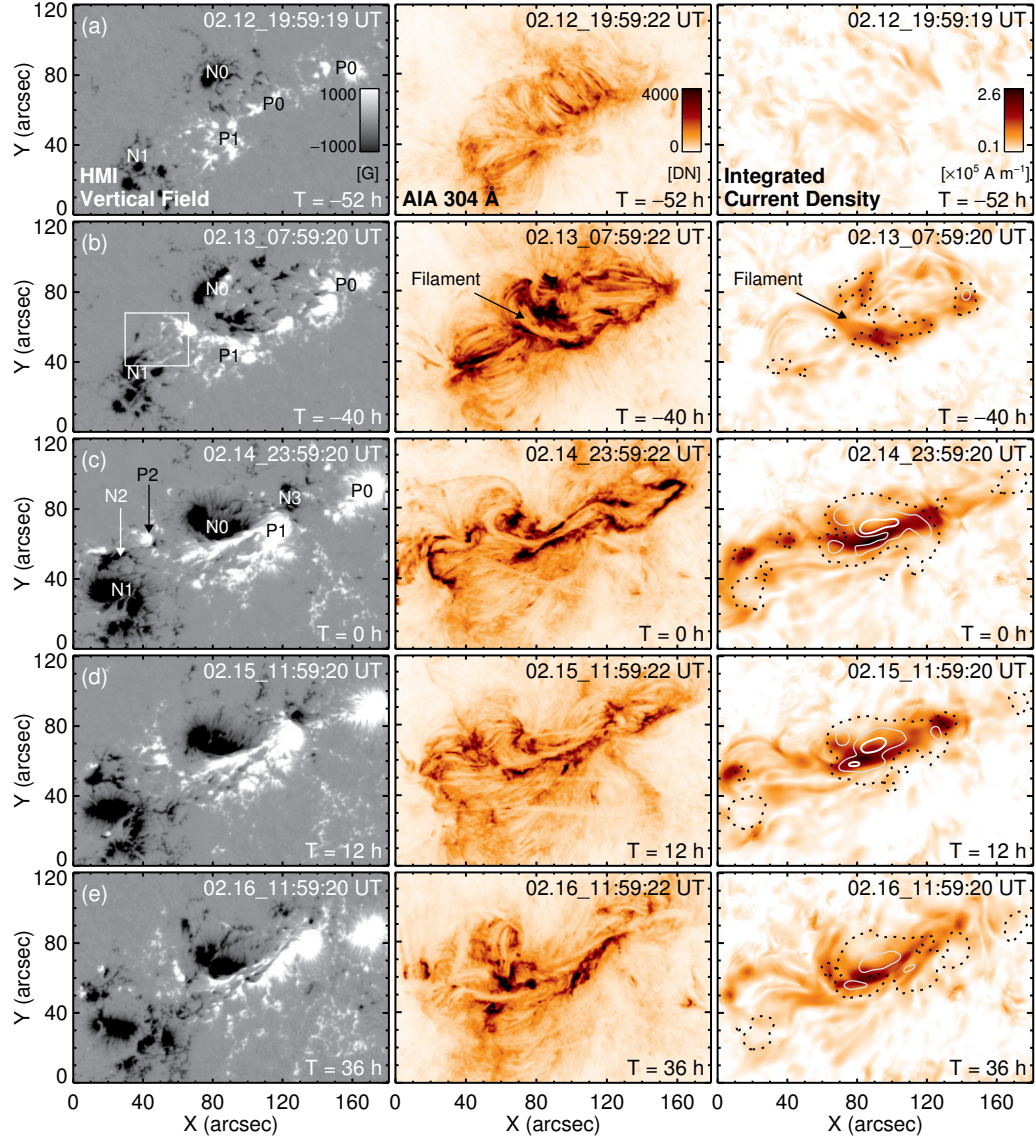


Figure 5.3: Five snapshots of the evolving AR11158. They are taken at about $T = -52$ h, -40 h, 0 h, 12 h, and 36 h, with February 15 00:00 UT as time 0. Left column: HMI B_z as in native coordinate (as recorded by camera). Middle column: negative AIA 304 Å image showing chromosphere and transition region structures in which the AR filament is best discernible. Right column: vertically integrated current density from NLFFF extrapolation over the lowest 10 Mm. The thick solid, thin solid, and dotted contours are for similarly integrated free energy density at 80%, 50%, and 20% of the peak value for frame $T = 0$ h. Images are remapped back to the native coordinate for direct comparison of HMI and AIA observations. The box in (b) indicates the field-of-view of Figure 5.5 for a flux-emerging region.

build-up process in the corona. A pair of newly emerged pores (P2/N2 in Figure 5.3(c)) with a few 10^{20} Mx flux undergo fast shearing on the northeastern side and substantially reconfigure

the coronal field. Smaller recurrent eruptions take place above these pores throughout the next two days. At the same time, the filament appears to be stretched. It increases in length, becomes somewhat warped (perhaps elevated) on the western end and extends further west to P0 (Figure 5.3(c)). Simultaneous flux cancellation is observed between P1 and N3, which may act favorably to the subsequent eruptions.

- Toward the end of the 5-day period (bottom two rows of Figure 5.3), flux emergence becomes episodic, sometimes overtaken by flux cancellation (Figure 5.4(a)). Nevertheless, the shearing between N0 and P1 continues. The integrated $|J|$ in the AR core region shows little sign of decreasing, and is fluctuating within 10% of the pre-flare value. A similar trend is present in $|I|$ as well (Figure 5.4(b)). Over time, the converging motion between sunspots of the same polarity starts to simplify the region toward a more bipolar structure. The filament seems to survive multiple eruptions and is still visible at the end of the 5 days.

5.2.3 Long-term Evolution of Magnetic Energy

We now consider the distribution of the magnetic free energy based on the NLFFF extrapolation. Spatially, the low-lying, current-carrying core field demonstrates strong concentration of free energy in the AR core, from the chromosphere to the lower corona. The free energy density (ϵ_f) appears largely co-spatial with the current distribution (Figure 5.3 right column). At $T = 0$ h, the 20% level contour of the peak ϵ_f (vertically integrated) accounts for only 9% of the AR area (Figure 5.3(c)), but 77% of the overall free energy. The height profile of ϵ_f plotted in Figure 5.4(f) shows that about 50% of all free energy is stored below 6 Mm, and 75% below 11 Mm. We note that the maximum free energy density occurs at about 3 Mm altitude, corresponding to the height of the peak in J_h (Figure 5.2(e)). These distribution patterns remain relatively stable after the filament becomes well defined in AIA images around -36 h.

The temporal profiles of the total NLFFF and PF magnetic energy (E_N and E_P) in Figure 5.4(c) roughly scale with the unsigned flux. On the other hand, the estimated magnetic free energy E_f in Figure 5.4(d) shows interesting variations in time and appears sensitive to AR activity, as one would expect. We plot the ratio E_N/E_P in Figure 5.4(e) as an additional measurement of the AR's non-potentiality. Uncertainties reported in this section only represent the effect of spectropolarimetric noise and are obtained from a pseudo Monte-Carlo method (see Section 5.2.4). Systematic uncertainties from the extrapolation algorithm may be greater. Again, several key features are highlighted below.

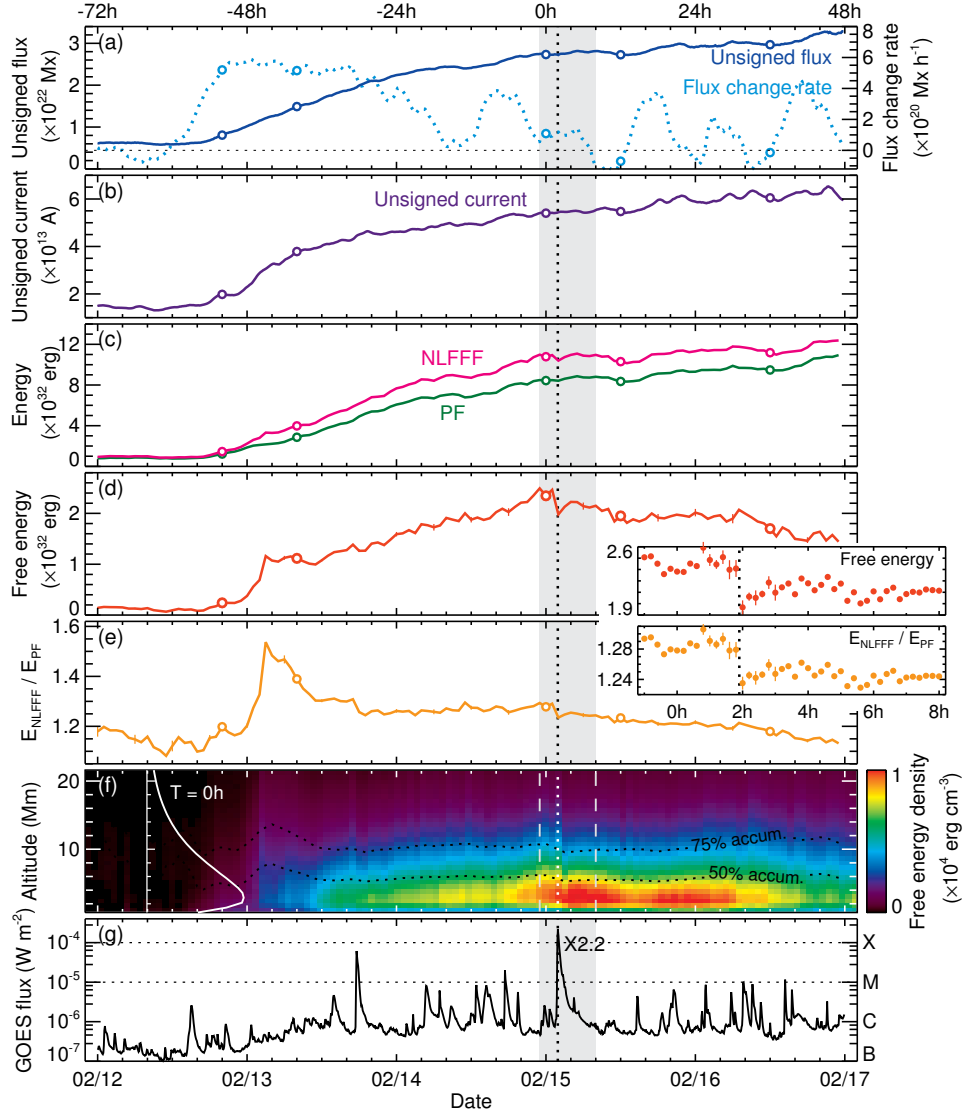


Figure 5.4: Evolution of magnetic energy and related quantities of AR 11158 over 5 days. (a) Total unsigned magnetic flux ($|\Phi|$) and 6-h smoothed flux change rate ($d|\Phi|/dt$). (b) Total unsigned current ($|I|$). (c) Magnetic energy derived from the NLFFF and PF extrapolation (E_N and E_P). (d) Estimated magnetic free energy (E_f). (e) Ratio between the NLFFF and PF energy (E_N/E_P). (f) Time-altitude diagram of mean magnetic free energy density in the AR center (FOV of Figure 5.7(f)). Dotted lines indicate the height below which the accumulated values reach 50% and 75% of the total. Curve on the left shows the height profile for $T = 0$ h. (g) *GOES* soft-X ray flux (1–8 Å channel). The 5 frames in Figure 5.3 are marked as circles. Insets of (d) and (e) show results with a 12 minute cadence from -1 h to 8 h (shaded grey band). The vertical dotted lines indicate the peak time of the X-class flare at 1.9 h.

- *Rapid free-energy injection during flux emergence.* E_f increases drastically following the flux emergence (Figures 5.4(a) and (b)). Free energy concentration is seen in the vicinity of the

filament (Figure 5.3(b)), and ϵ_f at all altitudes increases significantly (Figure 5.4(f)). In particular, E_f shows a twelve-fold increase from -55 h to -45 h, reaching 1.07×10^{32} erg and amounting to 43% of the final maximum E_f two days later. The ratio of E_N/E_P peaks at about 1.57 at -45 h. Significant changes in the coronal structures ensue, as conveyed by the AIA images (Figure 5.3). Flux change rate and E_f then plateau for a few hours, and E_N/E_P drops back to about 1.30. Careful inspections of the vector magnetogram reveals signatures of emerging flux tubes, which we discuss in Section 5.2.4.

- *Gradual energy build-up and decay.* After the initial fast increase, E_f accumulates at a slower rate (Figure 5.4(d)). The AR has attained a well-developed quadrupolar topology. The growth rate of E_f and the ratio E_N/E_P are both nearly constant. Similar trends can be found for the post X-flare stage, except now E_f starts to decrease and the region relaxes to a more potential state (Figures 5.4(d) and (e)). The energy dissipation rate in the corona probably has exceeded the growth rate from the photosphere as the flux emergence slows down (Figure 5.4(a)).
- *Step-wise energy loss during the X-class flare.* E_f reaches $(2.47 \pm 0.03) \times 10^{32}$ erg prior to the X-class flare, accounting for about 23% of the total energy. During the flare, E_f displays a step-wise sudden decrease (Figure 5.4(d) and inset). The 1 h average of E_f before and after the flare differ by about $(0.34 \pm 0.04) \times 10^{32}$ erg, 14% of the pre-flare E_f . This value situates at the lower end of what is adequate to power a typical X-class flare (e.g. Hudson, 2011, and references therein) and may be intrinsically an underestimation, as discussed in Section 5.2.4. A clear discontinuity also appears in the E_N/E_P and ϵ_f height profile. Sudden energy decrease is also found during the earlier M-6.6 flare (-30.4 h) with a smaller magnitude.

The continuous monitoring of the AR free energy with relatively high temporal/spatial resolution is made possible, for the first time, by the HMI vector field observations. This is especially useful for the study of major eruptive events. Due to the nature of the extrapolation method, changes in E_f here are determined by the boundary conditions. Therefore, the step-wise energy loss found during the X-class flare must be related to rapid and significant field changes on the photosphere. We consider this change in detail in Section 5.3.

5.2.4 On Energy Estimation

As discussed in Section 5.2.3, early flux emergence brings along a large amount of electric current and free energy. We show one of the flux emergence sites in Figure 5.5. Highly inclined fields

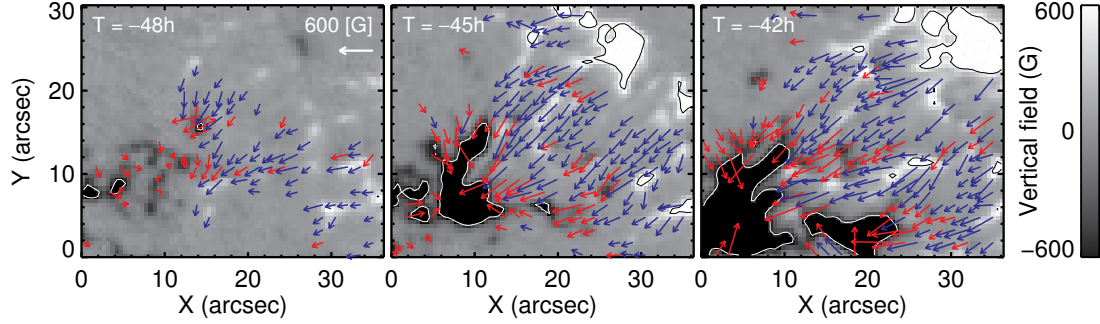


Figure 5.5: Three snapshots of a flux emergence site. The snapshots are 3 h apart. The FOV corresponds to the boxed region in Figure 5.3(b). B_z is plotted in the background; contours are for ± 600 G. Arrows indicate highly inclined B_h . For clarity, arrows are drawn only on every third pixel, for field strength $200 \text{ G} < B < 800 \text{ G}$, and for inclination $|\gamma| > 70^\circ$ with respect to the vertical. Images are in native coordinates.

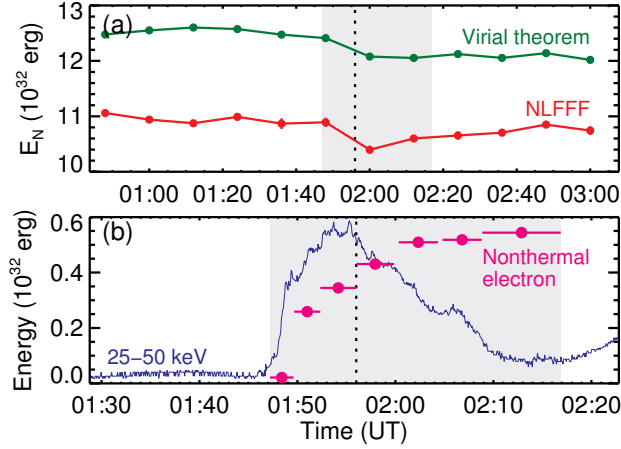


Figure 5.6: Estimation of flare energy release. (a) Magnetic energy estimated from the NLFFF extrapolation (same as Figure 5.4) and the magnetic virial theorem. The magnetic virial theorem is applied on preprocessed lower boundary; the uncertainty is derived from a Monte-Carlo approach. Most error bars are too small to be seen. The grey background indicates the period during which the nonthermal electron energy is fitted in the next panel. (b) Accumulated nonthermal electron energy derived from *RHESSI* HXR spectra using the thick-target model. Spectra for seven individual time intervals covering 01:44 UT to 02:17 UT (grey background) are fitted, the time range of each is noted by the horizontal bars. The HRX light curve in the 25–50 keV band is plotted in the background on a logarithmic scale. The vertical dotted line (01:56 UT) shows the SXR peak in GOES light curve.

(inclination angle γ measured from the vertical direction greater than 20°) appear within a widening patch, separating two vertical flux concentrations of opposite polarity that themselves grow in size and field strength in time. These patterns appear consistent with an emerging flux-tube at its initial stage of rising into the solar atmosphere.

Before -45 h (February 13 03:00 UT), E_N increases rapidly with the current injection from the increasing B_h . These highly inclined fields do not cause vertical flux to increase proportionally. Since the extrapolated potential field solely depends on B_z , the growth of E_P lags behind. This may explain the early peak in E_N/E_P shown in Figure 5.4(e). The decrease of E_N/E_P can in turn be explained by the subsequent fast increase in vertical flux relative to the horizontal counterpart when the axis of the flux tube approaches the photosphere.

We estimate the effect of spectropolarimetric noise on the energy estimation by conducting a pseudo Monte-Carlo experiment. In general, the noise level for the inverted HMI longitudinal field is below 10 G; it is about an order higher for the transverse component (Hoeksema *et al.*, 2012). For each frame, we create 10 extra-noisy Stokes profiles by adding to them a HMI-characteristic level of photon noise (on the order of 0.1% of quiet Sun intensity). Inversion, disambiguation and modeling are subsequently performed on these 10 inputs, and the standard deviation is adopted. The estimated noise-related uncertainty in E_N is typically around 0.6%, accounting for 2%–4% of E_f (Figure 5.4). This result is consistent with earlier tests on analytical field configurations and synthetic spectra with larger run numbers (Tiwari *et al.*, 2009). The relatively small effect is probably owing to the preprocessing procedure, which ensures force-freeness by smoothing away the spurious components. We nevertheless caution that the percentage uncertainty may be above 10% for E_f during the early stage of AR development, when the field is weaker and the measurement signal-to-noise (S/N) is lower.

To corroborate the result from the NLFFF extrapolation, we apply the magnetic virial theorem to the preprocessed lower boundary (e.g. Metcalf, Leka, and Mickey, 2005, and references therein). For the lower boundary ($z = z_0$) in a Cartesian coordinate, the energy of the force-free field E is

$$E = \frac{1}{4\pi} \int_{z=z_0} (xB_x + yB_y) B_z dx dy. \quad (5.2)$$

If the boundary is force-free enough and the region is largely isolated, as is the case for this HMI time series (see Section 5.4), the free energy in the volume is expected to be well recovered (Metcalf *et al.*, 2008). Around the X-class flare, the evolution of E_N computed from the virial theorem shows a similar trend to that from the NLFFF extrapolation, as shown in Figure 5.6(a); the energy decreases during the flare are similar as well. E_N derived from the virial theorem is about 14% higher.

For the energetics during the flare, we independently estimate the nonthermal electron energy using the hard X-ray (HXR) spectra from the *Ramaty High Energy Solar Spectroscopic Imager* (RHESSI; Lin *et al.*, 2002) under the classical thick-target model (e.g. Holmann *et al.*, 2003, and

references therein). The nonthermal electron flux spectra can be well fitted by a very steep power law with the index $\delta \sim 5\text{--}10$ and a low energy cutoff $E_c \sim 20\text{--}30$ keV. The total nonthermal energy integrated from 01:44 UT to 02:17 UT is estimated to be $\sim 0.54 \times 10^{32}$ erg, as shown in Figure 5.6(b). Since the energy needed for thermal plasma heating, CME lift-off, and flare radiation are expected to be on the same order of magnitude, if not greater than the nonthermal electron energy (Emslie *et al.*, 2004), the estimated total energy budget has to be on the order of 10^{32} erg.

Based on this analysis, the computed pre-flare E_f (2.47×10^{32} erg) is actually adequate to power this flare and accompanying CME eruption. On the other hand, the *difference* between the pre- and post-flare E_f (0.34×10^{32} erg), which we used as the estimate for energy loss, appears too small. One speculation is that the post-eruption coronal field is extremely dynamic and possibly deviates from the force-free condition, thus cannot be well described by a static force-free snapshot. If the field is locally (immediately above AR core) less energetic than what the NLFFF extrapolation indicates, then the discrepancy in the energy estimation will be alleviated. Another speculation involves the preprocessing scheme where a certain amount of smoothing is applied to the photospheric data to ensure the force-freeness of the boundary. Smoothing generally reduces the electric current inferred from the boundary, thus tending to lower the energy in the volume. Coordinated chromospheric magnetic field measurement from other observatories may help to constrain this procedure. A third possibility involves the photospheric field measurement itself. Small-scale field structures (sub-arc second) with high field gradients may carry strong electric current and a non-negligible amount of free energy, but will be unresolved with the moderate spatial resolution of HMI ($1''$), and thus overlooked in the modeling result.

5.3 Rapid, Irreversible Field Changes During Major Flares

5.3.1 Field Change During the X-class Flare

Figure 5.7 illustrates the rapid magnetic field changes during this X-class flare. Strong and permanent enhancement of B_h in the AR core was reported by Wang *et al.* (2012) based on the HMI linear polarization signal, and is confirmed here by full Stokes inversion. From 01:35 UT to 02:11 UT, the mean B_h along PIL (Figures 5.7(c) and (d)) increases from about 1200 G to over 1500 G, 28% within 0.6 h. Changes in B_z appear less significant (Figures 5.7(e) and (f)): mean $|B_z|$ decreases by about 5%. We skip the two frames in between (01:47 and 01:59 UT) to avoid artifacts from flare emission.

Shown in Figure 5.8, the difference image of pre- and post-flare B_h bears a striking resemblance

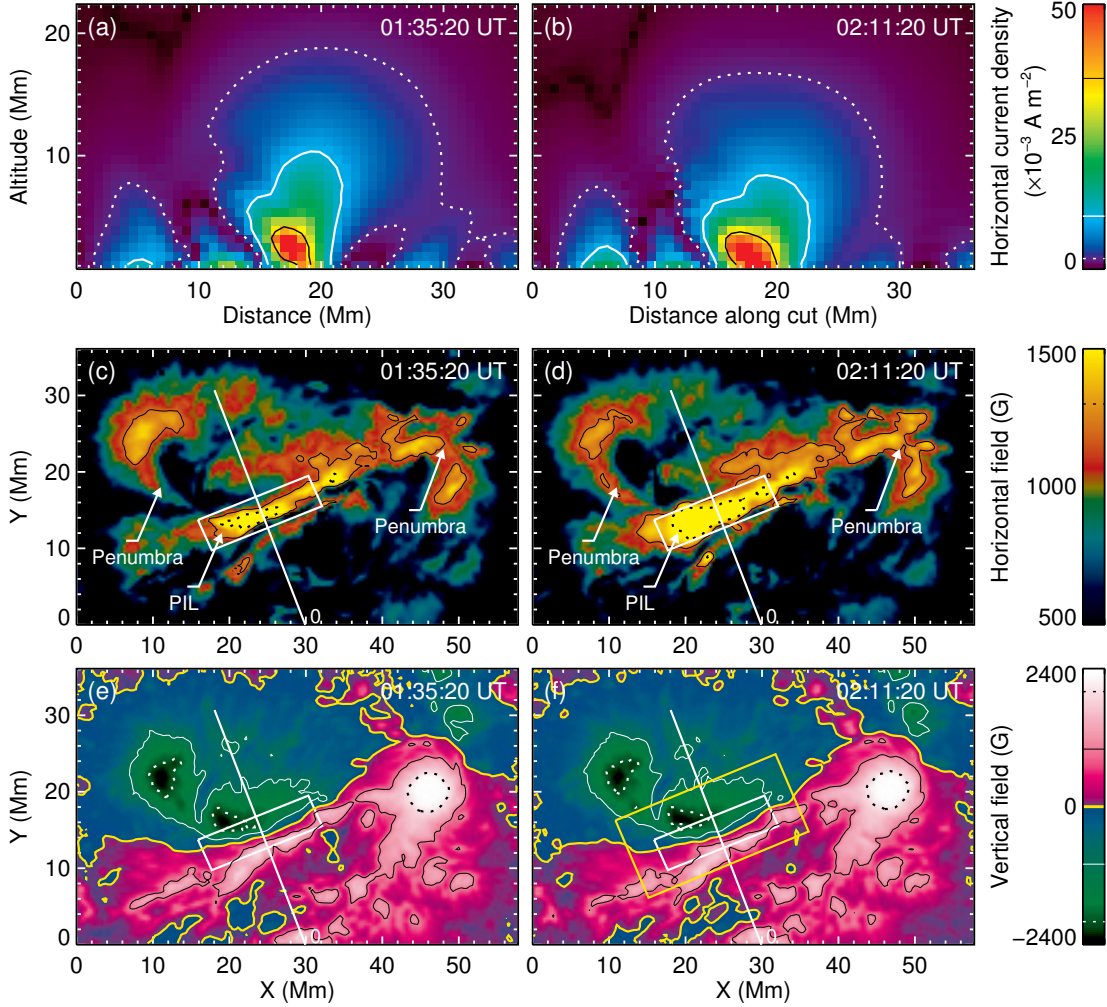


Figure 5.7: Rapid field changes at the photosphere and in the corona during the 2011 February 15 X-class flare. (a) J_h distribution on a vertical cross section as derived from NLFFF extrapolation, before the flare at 01:35:20 UT. Only the component perpendicular to the cross section is included. The location of the cross section is indicated in panels (c)-(f) as a long straight line. The dotted, dashed and solid contours indicate values of 2, 10, and 36 mA m^{-2} respectively. (b) Same as (a), for 02:11:20 UT after the flare. (c) Remapped B_h observed by HMI for 01:35:20 UT as viewed from overhead. The dotted (solid) lines show contour for 1600 G (1200 G). Places with significant field change are marked by arrows and boxes. (d) Same as (c), for 02:11:20 UT. (e) Remapped B_z at 01:35:20 UT. The dotted (solid) contours are for $\pm 2000 \text{ G}$ ($\pm 1000 \text{ G}$). (f) Same as (e), for 02:11:20 UT. The large yellow box indicates the region evaluated in Figure 5.11(d).

to the $\text{H}\alpha$ flare ribbons observed by the Solar Optical Telescope (SOT; [Tsuneta et al., 2008](#)) on the *Hinode* satellite ([Kosugi et al., 2007](#)). The elongated regions that are swept by the evolving ribbons or lying in between show significant B_h enhancement, whereas patches with decayed B_h appear on both the north and south sides. In the narrow region along the PIL, distribution of B_h shifts by

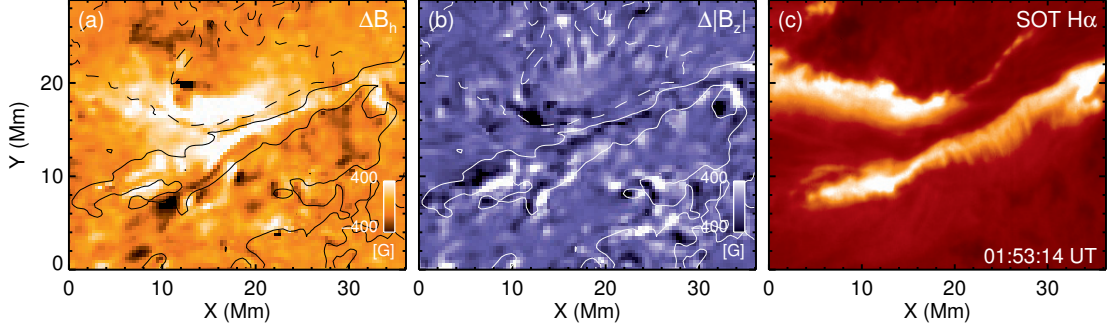


Figure 5.8: Difference images of pre- and post-flare magnetic field. (a) Difference of B_h between 02:11:20 UT and 01:35:20 UT. The two frames are kept in the native coordinates without remapping, but are co-aligned with Carrington rotation rate to the nearest full pixel. Contours are for the mean B_z of the two frames, at ± 600 G. (b) Difference image of $|B_z|$. (c) $H\alpha$ flare ribbons observed by *Hinode*/SOT at 01:53:14 UT, near flare peak and roughly midway between the two HMI frames.

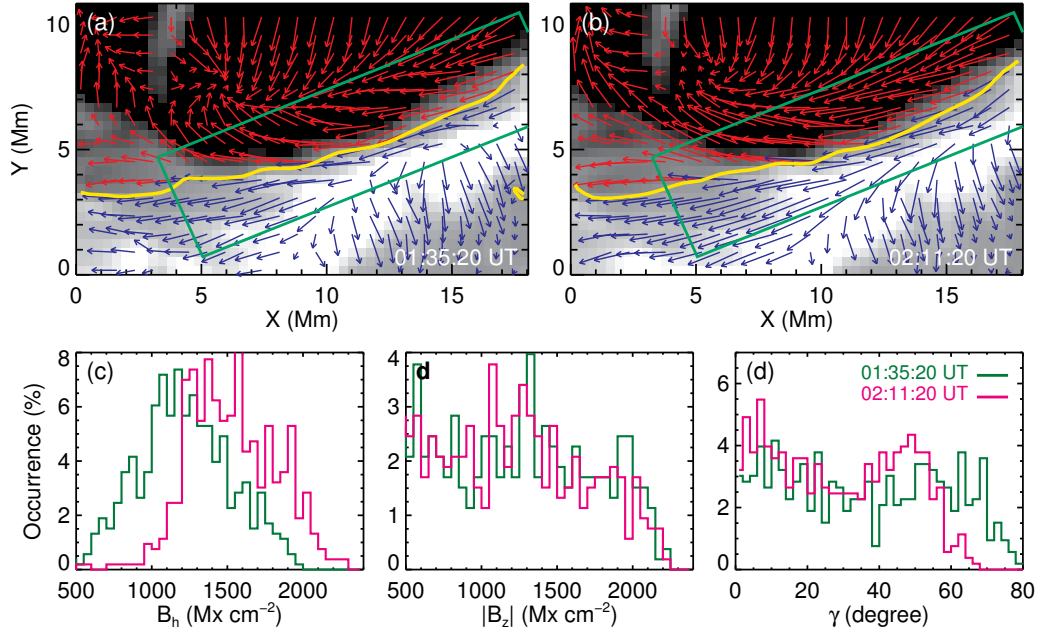


Figure 5.9: Close-up view of the pre- and post-flare vector field in the AR core region. (a) Remapped vector magnetogram for 01:35:20 UT. The yellow contour is the PIL; the boxed region is identical to Figure 5.7(c). (b) Same as (a), for 02:11:20 UT. (c) Histograms of B_h at two different times, in the boxed region in panel (a). (d) Histograms for $|B_z|$. (e) Histograms for inclination angle $|\gamma|$.

Table 5.2: Flare-related change in magnetic energy and photospheric field

Parameter ^a	Unit	Pre-flare ^b	Post-flare ^b	Difference ^c
E_f	10^{32}erg	2.47 ± 0.03	2.13 ± 0.03	-0.34 ± 0.04
E_N/E_P	-	1.29 ± 0.00	1.25 ± 0.00	-0.04 ± 0.01
$\langle B_h \rangle$	10^3 G	1.20 ± 0.02	1.53 ± 0.01	+28%
$\langle B_z \rangle$	10^3 G	0.96 ± 0.03	0.91 ± 0.03	-5%
$\langle B \rangle$	10^3 G	1.66 ± 0.01	1.87 ± 0.01	+13%
$\langle \gamma \rangle$	degree	36 ± 1	29 ± 1	-19%
$\langle J_z \rangle$	mA m^{-2}	36 ± 2	27 ± 1	-25%
$\langle \alpha \rangle$	Mm^{-1}	0.48 ± 0.03	0.30 ± 0.02	-37%

^a E_f and the ratio E_N/E_P are computed using the center region ($184 \times 144 \times 115 \text{ Mm}^3$) of the extrapolation domain. Other parameters are for the AR core photospheric field within the boxed region in Figure 5.7(c). Notations are same as Table 5.1.

^b For E_f and E_N/E_P , pre-flare values are calculated from the average of 5 frames between 00:47 to 01:35; post-flare between 02:11 and 02:59. Uncertainties are estimated effect from noise. For all others, pre-flare values are calculated for the 01:35 frame; post-flare for 02:11. Values are reported as mean \pm standard error for comparison.

^c Difference for E_f or E_N/E_P is the absolute value, others are percentage differences.

about 300 G in the histogram (Figure 5.9(c)), displaying a strong boost in the kilogauss range. On the other hand, $|B_z|$ often decreases where B_h increases, but the signals are weaker and appear to be mixed with the opposite. The distribution of $|B_z|$ gently decays in the strongest part, but otherwise remains similar (Figure 5.9(d)).

The combined effect is that the field becomes overall stronger and more inclined in the AR core (Figure 5.9(e)). In addition, the azimuth of B_h appear to change in a fashion such that they become better aligned and more parallel to the PIL in its vicinity (Figures 5.9(a) and (b)), consistent with previous reports (e.g. Wang *et al.*, 1994). After the flare, α appears to be smaller, suggesting the field is perhaps less twisted. A summary of the pre- and post-flare field parameters is provided in Table 5.2.

These fast changes suggest a scenario in which the change of coronal connectivity, probably induced by reconnection, feeds back to the photosphere. In particular, newly reconnected loops with footpoints located in the flare ribbons, both shorter and more parallel to the PIL, are *a priori* consistent with the observations. We discuss the topic further in Section 5.3.2. Morphologically, the changes are in line with the conjectured magnetic “implosion” (Hudson, 2000): a decrease in coronal magnetic energy during explosive events should lead the coronal field to contract, resulting

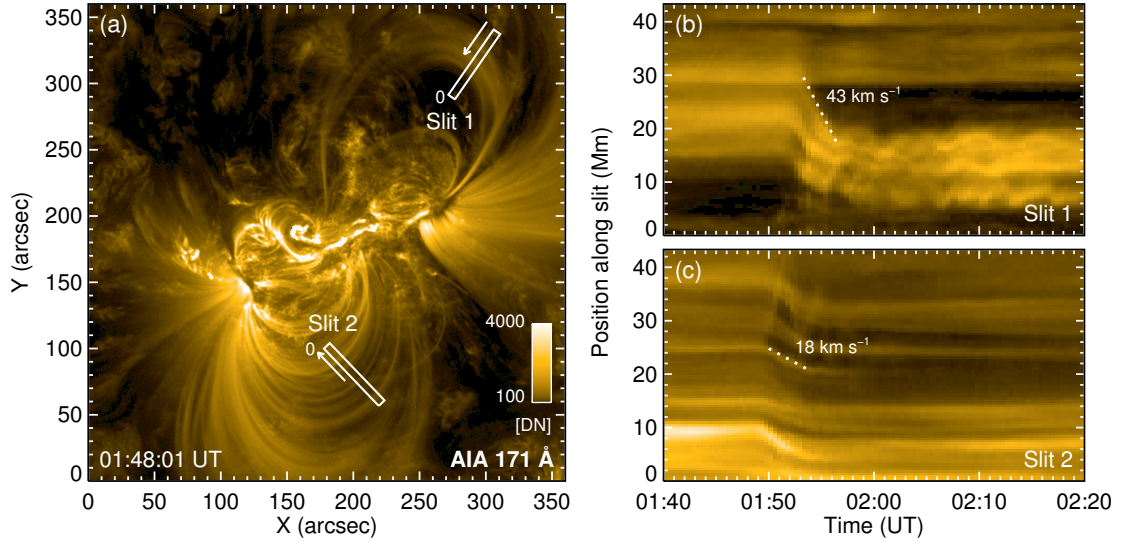


Figure 5.10: Observed EUV coronal loop retractions. (a) AIA 171 Å image at 01:48:01 UT on February 15, after the onset of flare. Two slits that are largely perpendicular to the loops are used to obtain the time-position diagrams in the following panels. Arrows along the slits indicate the approximate direction of the transverse motion. (b) Time-position diagram for slit 1 constructed by stacking a time sequence of coaligned image slices from left to right. Only the images with the normal exposure time are used, resulting in a 24 s cadence. Images are coaligned to sub-pixel accuracy. The dotted line shows an inward loop contraction pattern with a transverse speed of 43 km s^{-1} . The horizontal patterns in the upper half are from the features in the background. Loop oscillations are visible. (c) Same as (b), for slit 2. Dotted line shows a transverse speed of 18 km s^{-1} . Patterns of expanding loops also appear around 01:50 UT, moving from position 20 Mm toward 40 Mm.

in a “more horizontal” photospheric field (Hudson, Fisher, and Welsch, 2008). Here we analyze a series of NLFFF snapshots and monitor the J_h distribution on a vertical cross section through the computation domain (Figures 5.7(a) and (b)). The patterns show an apparent contracting motion at flaring time owing to the altered boundary condition. The apex of the outermost J_h contour descends by about 3 Mm in Figure 5.7(b).

Motions of coronal loops farther away from the AR core provide corroborating evidence for the conjecture. During flares and CMEs, a depletion of magnetic energy leads to smaller magnetic pressure gradient, and loops must contract to reach a new balance (e.g. Liu and Wang, 2010). We show AIA 171 Å observation for this event in Figure 5.10. Expansion of the coronal structure and faint circular propagating fronts are visible starting around 01:48 UT, probably linked to CME initiation (Schrijver *et al.*, 2011). At about 01:50 UT, the southern potential-like loops suddenly move inward; the northern loops follow immediately. The retraction proceeds for about 5 minutes, mostly during the flare impulsive phase. We place two vertical slits near the loop apexes to construct

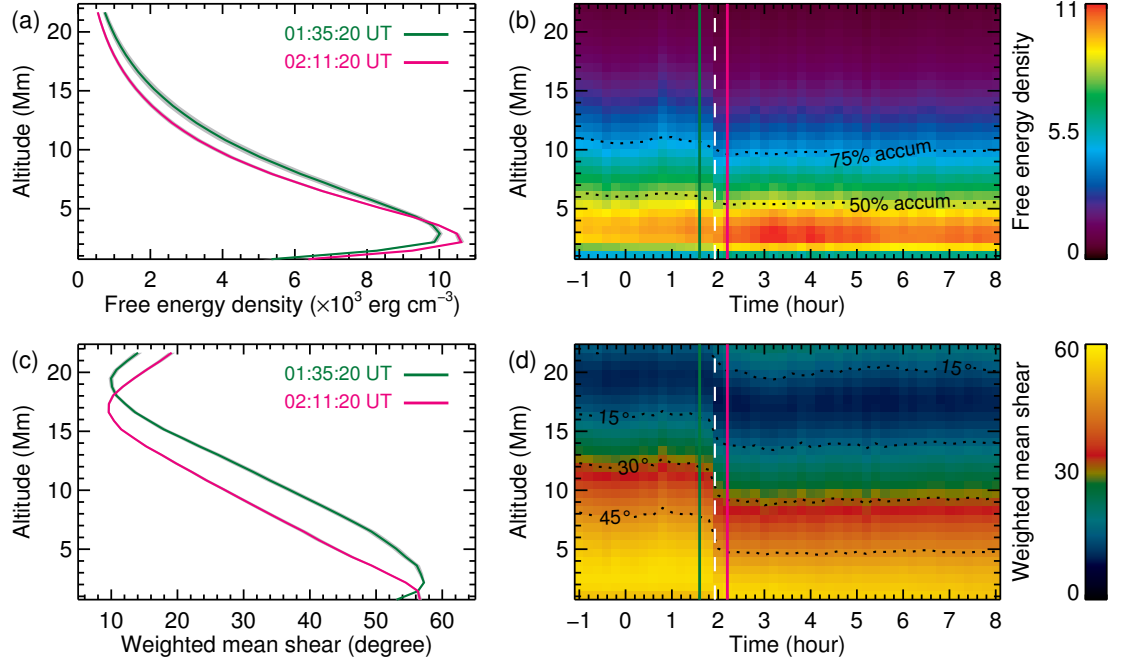


Figure 5.11: Altitude profile for extrapolated field around the time of the X-class flare. (a) Profiles of average magnetic free energy density in the AR core region (FOV of Figure 5.7(f)) at February 15 01:35:20 UT and 02:11:20 UT. Shaded grey band indicates the uncertainty due to noise, and is usually too narrow to be seen. (b) Time-altitude diagram for free energy density during the 9 h around the X-class flare, similar to Figure 5.4(f). The vertical dashed line indicates the flare peak time at 1.9 h. Green and pink vertical lines indicate the two profiles shown in panel (a). (c) Profiles of weighted mean shear (θ_w) near the PIL (yellow box in Figure 5.7(f)), at February 15 01:35:20 UT and 02:11:20 UT. (d) Time-altitude diagram for θ_w . Dotted lines show the heights at which the shear reaches 15°, 30°, and 45° respectively. PF becomes mostly east-west directed at about 20 Mm, a height much lower than that of NLFFF, thus resulting in the θ_w increase above 20 Mm.

time-position diagrams (Figures 5.10(b) and (c)). The inward motion shows a projected speed on the order of tens of kilometers per second, some with apparent oscillations. The transverse displacement can be as large as 15 Mm. The possible ambiguities in these observations are discussed and resolved in Section 5.3.2.

According to NLFFF extrapolation, such contraction yields a more “compact” energy distribution and a coronal field that relaxes more rapidly with height. We show in Figure 5.11(a) two altitude profiles of the mean free energy density before and after the flare. While the total magnetic free energy decreases after the flare, a larger percentage gets stored in the lower altitudes. Higher overlying field thus becomes even less energetic. Similar trends can be found in the field-weighted mean shear θ_w . Let \mathbf{B}_N and \mathbf{B}_P denote the NLFFF and PF vector, $B_N = |\mathbf{B}_N|$, $B_P = |\mathbf{B}_P|$, the

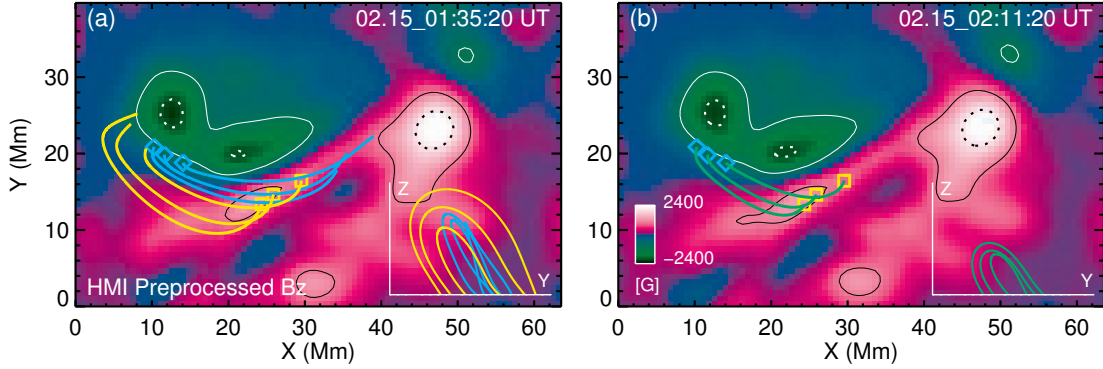


Figure 5.12: *Schematic* illustration of the field connectivity as possible results from reconnection in the AR core region. (a) Selected NLFFF field lines prior to the flare, plotted on preprocessed vertical field. The contours are drawn at ± 1000 and ± 2000 G. The eastern set of loops (yellow) are expected to reconnect with the central set (cyan) and exchange footpoints. Side view of the loops from the left (east) is plotted as inset. (b) Selected post-flare loops (green) with footpoints that belonged to the two different sets of pre-flare loops in the previous panel. The loops become much shorter. These snapshots demonstrate that the reconnection scenario is consistent with the observed photospheric field. They are *not* intended for identifying individual reconnecting loop pairs, nor modeling the reconnection process.

mean shear angle θ at each point is defined as:

$$\theta = \cos^{-1} \frac{\mathbf{B}_N \cdot \mathbf{B}_P}{B_N B_P}. \quad (5.3)$$

The weighted mean shear θ_w is computed by summing over all pixels in the domain (Wang *et al.*, 1994):

$$\theta_w = \frac{\sum \theta B_N}{\sum B_N}. \quad (5.4)$$

This quantity measures the field-weighted direction difference between the NLFFF and PF field, thus providing a quantitative description of the non-potentiality of the magnetic field. As shown in Figure 5.11(c), the whole profile moves downwards by about 2 Mm, equivalent to a shear decrease at almost all heights. The bottom layer, as an exception, becomes slightly more sheared because B_h is now more parallel to the PIL (cf. Wang *et al.*, 1994). The time-height diagrams covering 9 h around the flare with 12 m cadence more clearly convey the sudden and permanent nature of the changes (Figure 5.11(b) and (d)).

5.3.2 Possible Causes and Consequences

The rapid (~ 10 min) field change at the flare time likely has a coronal driver, as the photospheric Alfvén timescale is too long to be compatible (e.g. Hudson, 2011). Reconnection, in particular,

may change the coronal field connectivity fast enough to result in large-scale field variation at the “line-tied” loop footpoints. We illustrate one of the *consequences* in Figure 5.12 using the NLFFF extrapolation. Before the flare, highly sheared field lines (Figure 5.12(a)) cross over each other near their footpoints, creating a configuration in favor of tether-cutting reconnection. Sigmoidal core loops “are sheared past each other so that they overlap and are crossed low above the neutral line” (Moore *et al.*, 2001). These loops exchange footpoints during the reconnection, and the inner footpoints indeed appear to be well linked in the post-flare field in the NLFFF extrapolation (Figure 5.12(b)). New loops become shorter, consistent with the enhanced B_h on the boundary. We note that the illustration is purely *schematic* without any reference to the reconnection process itself. Moreover, loops on the north and south sides, further away from the PIL, may become connected after the flare, resulting in a more vertical configuration where B_h decreases (Figure 5.8(a)), similar to the effect of δ -spot umbral darkening reported in Liu *et al.* (2005). This scenario has been indirectly probed through the contraction of HXR sources (Ji, Huang, and Wang, 2007) and the unshearing motion of flare ribbons (Ji *et al.*, 2006; Su, Golub, and Van Ballegooijen, 2007). Direct imaging can be difficult as EUV or SXR images are usually saturated during major flares. The complicated temperature structures of the flaring atmosphere may also prevent a straightforward interpretation of the observations.

Besides the short loops near the PIL, tether-cutting reconnection also produces a flux-rope that connects the two far ends of the sigmoid after the exchange of the footpoints (Moore *et al.*, 2001). In a detailed account of the coronal activities in this event, Schrijver *et al.* (2011) use MHD modeling (Aulanier *et al.*, 2010) to interpret the observations and find that the flux-rope formed by reconnection eventually erupts as part of the CME structure. Interesting evidence also arises from the “sunquake” observation reported by Zharkov *et al.* (2011) following an initial report by Kosovichev (2011). Two distinctive photospheric seismic sources are found at the two far ends of the sigmoid and their initiations closely match the flare/CME onset time. Because the signals appear before the HXR emission peak time and do not spatially match the HXR sources, they cannot be explained by particle precipitation as many earlier events are. Instead, flux-rope eruption appears to be the trigger, and magnetic variation is proposed as one of the possible mechanisms. The coronal fields rapidly reconstruct after the eruption and the overall effect may be a strong downward impulse into the photosphere (Hudson, Fisher, and Welsch, 2008). Nevertheless, it is pointed out that the seismic sources do not appear to be co-spatial with the strongest magnetic field or the strongest field variations (Kosovichev, 2011). The exact excitation mechanism remains to be explained.

Regarding the possible ambiguity in the loop retraction observed in AIA 171 Å (Figure 5.10), we can rule out the scenario where loops remain steady but only cool sequentially into the EUV temperature sensitive passband. Such an explanation cannot account for the sudden start and stop of the motion, or the apparent loop oscillations. To rule out the projection effect, we inspect the coronal image sequences taken by SECCHI EUVI (Howard *et al.*, 2008) on the twin *STEREO* spacecraft that are both near quadrature from the Sun-Earth line. The coronal loops, when viewed from the side, appear to become “flattened” and in general pressed down toward the solar surface during the eruption. The apparent loop length, if unchanged, should increase instead. Therefore the retraction is likely to be real, its amplitude and speed underestimated from overhead AIA observation. Detailed analysis of EUV loop motion may provide quantitative diagnostics of the coronal field (e.g. Aschwanden and Schrijver, 2011), but is out of the scope of this work.

We note that the field change discussed here must be distinguished from the apparent transient variations in the longitudinal field (Kosovichev, 2011). The latter last only a couple of tens of minutes and is likely an artifact caused by flare-related emissions. HMI spectra at these abnormal pixels briefly deviate from the usual absorption profile, showing an enhanced line center as expected (Maurya, Reddy, and Ambastha, 2012).

5.4 Discussion on Field Extrapolation

Previous studies of coronal field extrapolation have shown the importance of appropriate input boundary conditions (e.g. Metcalf *et al.*, 2008; DeRosa *et al.*, 2009). It is suggested that the input magnetograms should: i) have a large FOV with sufficient information on the horizontal component even in the weak field region; ii) have balanced magnetic flux; and iii) have balanced Lorentz force and torque. The HMI vector magnetograms used in this study appear to be a good candidate. For the February 14 20:35 UT frame, the region of interest with strong field ($|B_z| > 100$ G) covers the center 11% area of the FOV (a total of 216×216 Mm²) and is isolated from the side boundaries. There are no extended plage regions or ARs nearby, and the large outskirts included correspond to a coronal volume that contains most of the observed EUV loops. The net magnetic flux accounts for only 0.3% of the total unsigned flux for the strong field region, thus the flux is well balanced. In particular, the surface integrated Lorentz force and torque are 5–15 times lower than the several data sets used in earlier studies (from different instruments, for different ARs) (Wiegmann *et al.*, 2012). We note that such low Lorentz force/torque may be a special case, as the photospheric field is generally not expected to be force-free (Metcalf *et al.*, 1995). For the preprocessing scheme

(Wiegmann, Inhester, and Sakurai, 2006) applied before the extrapolation, we test and adopt the following parameter set: $\mu_1 = \mu_2 = 1$, $\mu_3 = 0.001$, and $\mu_4 = 0.01$. Here μ_1 and μ_2 control the net force and torque on the boundary respectively; μ_3 controls the relative influence of the observed data, and μ_4 the level of smoothing.

We evaluate the quality of the extrapolation by computing three metrics: the mean Lorentz force L_f , the mean field divergence L_d , and the current weighted mean angle between the magnetic field and electric current σ_j :

$$L_f = \left\langle \frac{|\nabla \times (\nabla \times \mathbf{B})|^2}{B^2} \right\rangle, \quad (5.5)$$

$$L_d = \langle |\nabla \cdot \mathbf{B}|^2 \rangle, \quad (5.6)$$

$$\sigma_j = \sin^{-1} \left(\left\langle \frac{|\mathbf{J} \times \mathbf{B}|}{B} \right\rangle / \langle J \rangle \right), \quad (5.7)$$

where \mathbf{B} is the NLFFF field vector, $B = |\mathbf{B}|$, $J = |\mathbf{J}|$, and angle brackets denote the mean value within the domain. Following literature, we normalize L_f , L_d to a unit volume and normalize L_d further by 1 G^2 . Ideally all should vanish. For a total of 120 hourly frames computed in this study, we find $L_f = 6.4 \pm 2.2$, $L_d = 3.1 \pm 1.2$, and $\sigma_j = 18.0^\circ \pm 1.2^\circ$. These values are typical for this optimization-based algorithm and are comparable to previously reported results based on other solar data sets (e.g. Schrijver *et al.*, 2008).

It has been pointed out that even after preprocessing, the observed field, with its uncertainties, is still incompatible with a strictly force-free field (DeRosa *et al.*, 2009). The fact that a better suited input does not lead to noticeable improvement in this case may suggest an internal limit to the current algorithms when dealing with realistic, imperfect boundary conditions. In light of this, a new implementation of the optimization scheme (Wiegmann and Inhester, 2010) has been developed and tested for HMI data. After including information on the horizontal field measurement uncertainties, the solution proves to satisfy the force-free condition significantly better (Wiegmann *et al.*, 2012). For the 20:35 UT frame, σ_j is reduced from 16.6° to 5.7° .

Problems may also arise when we adopt a large computation domain but still assume a planar boundary. A magnetogram spanning about 18° in Heliographic longitude, as used in this study, will then have its edge elevated by $(\sec 9^\circ - 1)R_\odot$ (8.7 Mm, or 12 pixels) above the solar surface. This may be a reason that we fail to faithfully reproduce the long loops on the north side. These loops extend far away from the AR center and appear to be low-lying judged from the *STEREO*/EUVI observations. They are thus more subject to inconsistencies in the boundary condition. We note that the free energy estimation may be less effected in this case, as these loops are largely potential-like.

Nevertheless, as multiple ARs are often magnetically connected in a global scale, implementation of the model in spherical geometry (e.g. Tadesse *et al.*, 2012) becomes necessary.

5.5 Summary

We have studied the magnetic field and its energy of AR 11158 over a period of 5 days using a series of HMI vector magnetograms. A NLFFF extrapolation, coupled with coronal imaging, provides information of the coronal magnetic structure, electric currents and free energy. From its early flux emergence to recurrent major flares and CME eruptions, the AR displays distinctive stages of energy build-up and release, driven by or resulting in gradual or sudden magnetic field changes. We summarize the major results as follows:

- The quadrupolar AR primarily consists of two interacting bipoles. The trailing polarity of the leading pair and the leading polarity of the trailing pair undergo significant shearing. A pronounced filament appears over the major PIL early and its main part persists through multiple eruptions, including the X-2.2 class flare and halo CME on 2011 February 15. NLFFF extrapolation suggests that the field in the filament channel carries strong current, and is highly sheared with about 0.9 turn near the axis.
- NLFFF extrapolation indicates significant electric current and free energy injection during early flux emergence, about 10^{32} erg over a mere 10 h. Current and energy mostly concentrate in or near the filament channel in the low atmosphere: over 50% is stored below 6 Mm. The computed peak free energy reaches about 2.59×10^{32} erg. A 0.34×10^{32} erg decrease is found within 1 hour after the X-class flare. We show that the effect of random noise is small, but the systematic uncertainties can be large. The energy loss is most likely underestimated.
- Rapid and irreversible enhancement of the horizontal field takes place along the PIL during the X-class flare. The increase in B_h is 28% on average; only a 5% decrease is found for $|B_z|$ and the signal is mixed. The observed photospheric field becomes overall stronger, more inclined and better aligned with the PIL. The short time scale indicates a coronal driver. Shorter loops created by tether-cutting type reconnection are *a priori* consistent with the photospheric signatures. The reconnection picture is supported by the fact that the change largely happens in the area that are either swept by the flare ribbons or lying in between.
- NLFFF extrapolation demonstrates that the change in the photospheric and coronal field is morphologically consistent with the “magnetic implosion” conjecture. Energy loss during the

explosions cause the coronal field to contract to reach a new balance. This scenario is supported by the EUV loop retractions observed from AIA. The extrapolated field appears to be more “compact” after the flare, the lowest layer is more sheared but it relaxes faster with height and is overall less energetic.

Regular quantitative study and statistical surveys of a large ensemble of AR vector magnetic fields now become possible with HMI observing the full solar disk at high spatial and temporal resolution. Although problems still abound in both data reduction and modeling procedures, we anticipate more in-depth studies using the newly available data will eventually lead to better understanding of the AR magnetic fields and energetics.

* The content of this Chapter is based on [Sun *et al.* \(2012a\)](#). All figures and a major part of the text are reproduced by permission of the AAS. I adapted the extrapolation code, performed the modeling and most of the analysis. Q. Chen analyzed the hard X-ray data. Dr. T. Wiegmann provided the original extrapolation code. Dr. J. Thalmann tested and determined the coefficients used in magnetogram preprocessing.

Chapter 6

Non-Radial Eruptions Modulated By Magnetic Field Topology

6.1 Introduction

6.1.1 Solar Eruption and Magnetic Topology

Solar eruptive events derive their energy from the non-potential coronal magnetic field ([Forbes, 2000](#); [Hudson, 2011](#)). Reconnection takes place locally where the field gradient is large, but can alter the larger-scale field topology rapidly. The dissipated energy from the relaxing field accelerates particles, produces radiation, and heats and ejects plasma into the interplanetary space as a coronal mass ejection (CME).

Prior to eruption, energy builds up in the corona through flux emergence and displacement, which may take up to a couple of days (e.g. [Schrijver, 2009](#)). The slow evolution can be approximated by a series of quasi-stationary, force-free states in the low plasma- β coronal environment. This allows the estimation of AR energetics in non-flaring states, thanks to recent advances in photospheric field measurement and field extrapolation algorithms ([R gnier and Canfield, 2006](#); [Thalmann and Wiegmann, 2008](#); [Jing *et al.*, 2009](#); [Sun *et al.*, 2012a](#)).

Besides the gross energy budget, the detailed magnetic configuration also proves important to the initiation, geometry, and scale of eruptions. In the case of a coronal jet, the direction of the ambient field (horizontal or oblique) directly determines the direction of the jet and its distinct emission features (two-sided or “anemone” type, [Shibata *et al.*, 1997](#)). Observation and modeling demonstrate that the overlying field provides a critical constraint on CME speed and trajectory ([Liu, 2007](#); [Gopalswamy *et al.*, 2009](#); [Wang *et al.*, 2011](#)).

Theoretical studies have extensively explored the role of topological features in reconnection

(Démoulin *et al.*, 1996; Priest and Forbes, 2000; Longcope, 2005). Their applications to solar events usually involved the results of potential or linear force-free field extrapolation (Aulanier *et al.*, 2000; Fletcher *et al.*, 2001; Mandrini *et al.*, 2006), or magnetohydrodynamic (MHD) simulations that qualitatively reproduce the observed phenomena (Moreno-Insertis, Galsgaard, and Ugarte-Urra, 2008; Pariat, Antiochos, and DeVore, 2009; Masson *et al.*, 2009; Török *et al.*, 2011).

In this Chapter, we study one of several similar non-radial eruptions that are strongly modulated by the local magnetic field as observed with the *Solar Dynamic Observatory* (*SDO*). Using vector magnetograms from the Helioseismic and Magnetic Imager (HMI) (Schou *et al.*, 2012; Hoeksema *et al.*, 2012) aboard *SDO* and a non-linear force-free field (NLFFF) extrapolation, we monitor the AR evolution and explain the magnetic topology that leads to the curious features during the eruption. The Atmospheric Imaging Assembly (AIA; Lemen *et al.*, 2012) and other observatories recorded these features and provide guidance for our interpretation.

We first present observations of the eruption in Section 6.2, and then come back in Section 6.3 to explain the magnetic field and energy evolution leading to the event. In Section 6.4, we interpret this curious event based on the magnetic field topology. We discuss the interpretation in Section 6.5 and summarize in Section 6.6.

6.1.2 Data and Modeling

Sunspot complex AR 11158 produced the first X-class flare of cycle 24 near its center on 2012 February 15 (Schrijver *et al.*, 2011). Before and after that flare, there were a series of smaller eruptions from its northeastern periphery, our region of interest (ROI), where a small new bipole emerged. Five of them assumed very similar structures and were accompanied by C or M-class flares within a 20-hr interval (06:58, 12:47, 17:26, and 19:30 UT on February 14, and 00:38 UT on February 15; see Figure 6.4(d)). In all cases the ejecta followed a similar, non-radial trajectory towards the northeast.

We focus here on the event around 17:26 UT on February 14 associated with an M-2.2 class flare. The eruption site was near central meridian (W04S20). For context, we study the AR field evolution during a 36-hr interval leading to and shortly after the event, from February 13 12:00 UT to February 15 00:00 UT.

The HMI vector data reduction and the modeling procedures are identical to those used in Chapter 5, where we described and evaluated the algorithm in detail.

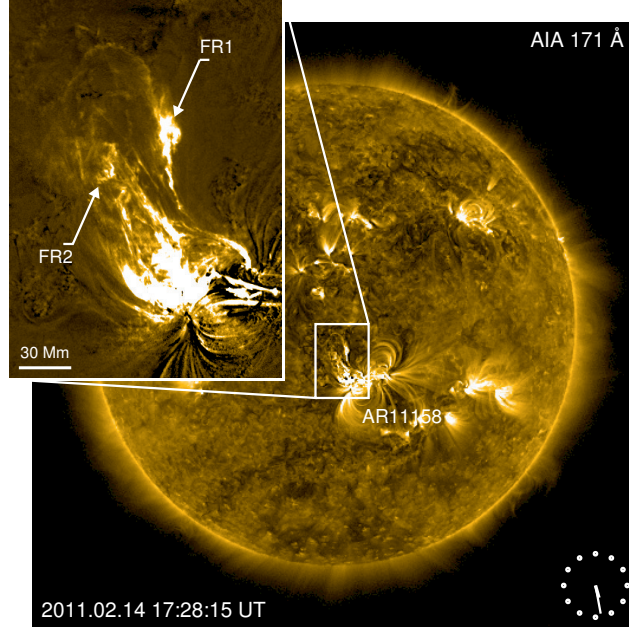


Figure 6.1: Full-disk, unsharp masked AIA 171 Å image at 17:28:15 UT on February 14, 2011 showing the non-radial eruption. Inset shows the enhanced image of the ejecta. The two flux-rope-like structures with a shared eastern footpoint are marked as FR1 and FR2. Animation of a 20-hr interval shows at least five similar eruptions.

6.2 Non-Radial Eruption

Observed in the AIA extreme-ultraviolet (EUV) bands, a small AR filament situated above the polarity inversion line (PIL) of a newly emerged bipole started its slow rise around 17 UT. The M-class flare peaked at 17:26 UT in soft X-ray (SXR) flux, when the filament rapidly erupted towards the northeast. The ejecta appeared to consist of two rope-like features (FR1 and FR2 in Figure 6.1) with a shared eastern footpoint. By inspecting AIA image sequences in various bands and HMI magnetograms, we think that they originated from the same filament structure.

The *STEREO-A* spacecraft was then near quadrature with the Sun-Earth line (87° ahead). Its SECCHI EUVI instrument (Howard *et al.*, 2008) caught a glimpse of the ejecta in the 195 Å channel (Figures 6.2(a)), where the erupted filament appeared to follow a straight trajectory viewed from west. Using the simultaneous image from the AIA 193 Å channel (Figures 6.2(b)), we are able to estimate its three-dimensional (3D) geometry.

Figure 6.2(c) illustrates the triangulation procedure. We manually select the eruption site O and the frontmost point P of the inner flux rope FR2 (as projected on the plane of sky) in the AIA image. We select the corresponding points O' and Q in the EUVI image, such that 1) O and O' have

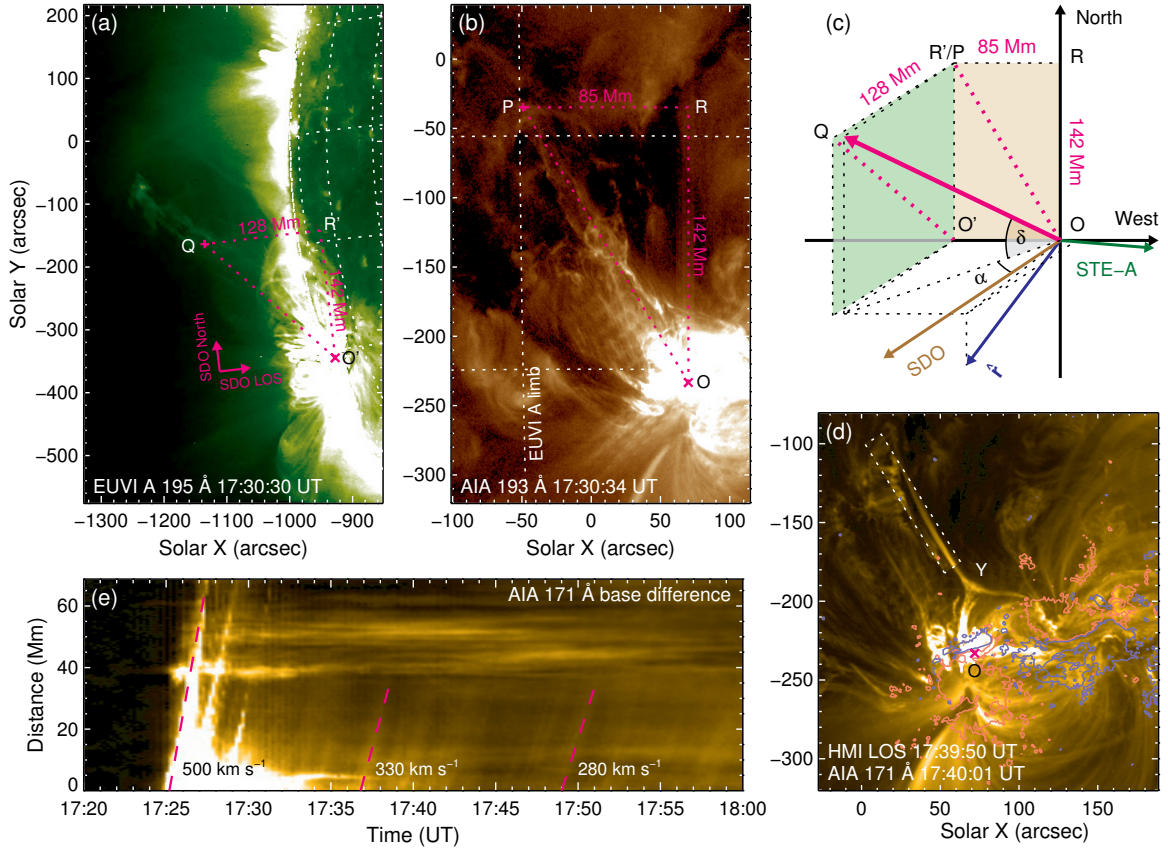


Figure 6.2: Geometry of the non-radial eruption. O and O' mark the eruption site. (a) SECCHI EUVI 195 Å image from *STEREO-A*, about 87° ahead of *SDO*. Due to the tilt of the solar rotational axis, the *SDO* and *STEREO* north are offset by 6.8° . (b) AIA 193 Å image of the same ejecta, taken 4 s later than (a). The projected N-S length of the ejecta ($|OR|$) is identical to that in (a) ($|O'R'|$), where OR and O'R' represent the projection of line segments OP and OQ in the N-S direction in *SDO*'s plane-of-sky, respectively. The scales of (a) and (b) are different in order to better show the features of interest. (c) Schematic diagram explaining the determination of the ejecta's geometry. *SDO*'s west, north, and LOS directions are taken as x , y , and z axis. The pink arrow represents the ejecta, its projected shape viewed from EUVI and AIA are shown as pink dashed lines on green and brown planes. The local radial vector is about W13S04 to LOS. The inclination δ is about 43° ; azimuth α about 34° . See Section 6.2 for details. (d) AIA 171 Å image of the post-eruption AR; Y marks the top of the cusp and the base of the jet. The boxed region is used to construct panel (e). Purple/pink contours are for HMI LOS field at ± 200 G. (e) Space-time diagram showing the speed of ejecta and jet. Three dashed lines (starting near 17:25, 17:36, and 17:49 UT) indicate a projected speed of 500, 330 and 280 km s^{-1} , respectively. Panels (a), (b), and (d) are displayed in a square-root scale.

the same Carrington coordinate; 2) the ejecta's N-S extent in two images satisfies $|OR| = |O'R'|$, where OR and O'R' represent the projection of line segments OP and OQ in the N-S direction in *SDO*'s plane-of-sky, respectively.

Assuming the ejecta follows a straight trajectory, we can solve for its inclination δ and azimuth α

with respect to the line-of-sight (LOS). We find that $\delta=43^\circ$, $\alpha=34^\circ$. By repeating the point selection process we estimate the uncertainty to be $\sim 3^\circ$ under the current scheme. The trajectory is highly inclined, about 66° with respect to the local radial direction.

A bright, inverted-Y shaped structure formed in the wake of the eruption. It consisted of a thin spire on top of a cusp-shaped loop (Figure 6.2(d)); both lasted over 1 hr. The cusp appeared almost two-dimensional and had both “legs” rooted in negative polarity flux (see Section 6.4 and Figure 6.5(b)). There were propagating brightness disturbances along the cusp legs and the spire (Thompson *et al.*, 2011b), which have been interpreted as episodic plasma flows (see the coronal seismic and Doppler analyses in Su, Shen, and Liu, 2012; Tian *et al.*, 2012). These observed features outline a magnetic arrangement that resembles a coronal jet (e.g. Shibata *et al.*, 1997). Nevertheless, the structure appeared only *after the eruption*. Various observed features appear to require alternative explanations other than the standard jetting model or its variations (see a brief discussion in Section 6.5.3).

By placing a cut along the thin spire in the AIA 171 Å image sequence, we construct a space-time diagram to illustrate the relevant speeds in this event (Figure 6.2(d) and (e)). The projected speed of the ejecta is about 500 km s^{-1} ; the brightness disturbance is around 300 km s^{-1} . Considering the inclined trajectory, we estimate the real speed about 30% higher, i.e. 650 and 390 km s^{-1} , respectively.

6.3 Emerging Bipole As Energy Source

We study the underlying photospheric field that led to this eruption. Figure 6.3(a) shows a snapshot of the radial field taken 25 minutes before the event as derived from the vector magnetogram. The AR mainly consists of two interacting bipoles. A large amount of magnetic free energy was stored near the major PIL between the shearing sunspots at center of the field of view (FOV), where the X-class flare took place (Sun *et al.*, 2012a).

The eruption studied here is related to a newly emerged, smaller bipole (boxed region in Figure 6.3(a)). The bipole appeared on February 13 in the northeastern part of the AR. Starting from 12 UT on February 14, the positive component advanced rapidly westward with strong rotational motion and shearing with respect to its negative counterpart, leaving behind a fragmented stripe of flux mimicking a long-tailed tadpole (Figure 6.3).

The new bipole had strong horizontal photospheric field that lay parallel to the PIL (Figure 6.3(b)). NLFFF extrapolation suggests a highly twisted core field and strong radial current

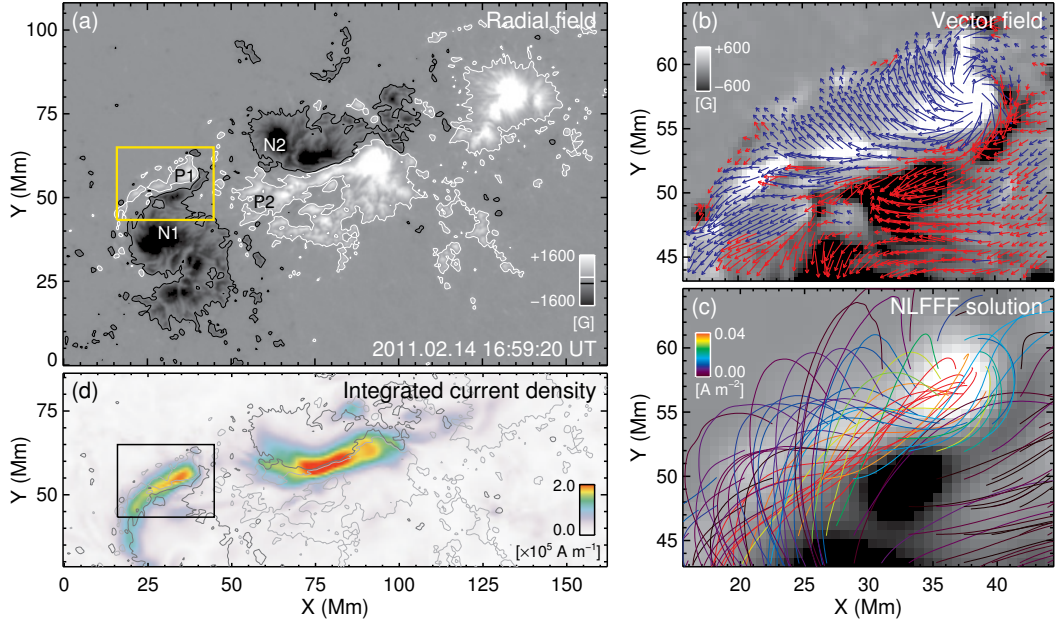


Figure 6.3: Snapshot of magnetic field of AR 11158, 25 minutes before the eruption. (a) Radial magnetic field (B_r) map as derived from the vector magnetogram. The contours are for ± 200 G. P1, N1, P2, and N2 mark four components of the quadrupolar flux system. The yellow box indicates the FOV for (b) and (c) and is identical to that in (d). (b) Photospheric vector magnetic field map. Gray-scale background shows B_r . The blue/red arrows indicate the horizontal component (\mathbf{B}_h) with positive/negative radial counterpart, where field strength $B > 200$ G. Their lengths correspond to the magnitude (B_h); their directions show the azimuth. (c) Selective extrapolated field lines plotted on B_z map. The color shows the amount of radial current at the field line footpoint. (d) Map of current density ($|J|$) integrated over the lowest 10 Mm in extrapolated field. The light/dark gray contours are for $B_r = \pm 200$ G. All data are deprojected and remapped using the Lambert equal area projection.

(Figure 6.3(c)), which correspond to the observed AR filament that eventually erupted.

We summarize in Figure 6.4 the bipole's temporal evolution. By evaluating the area within the ROI (boxed region in Figure 6.3(a)), we estimate its unsigned flux to be only about 5% of the AR's total around the eruption time. However, the surface unsigned radial current within the ROI accounts for 12% of the AR's total, much higher than the corresponding flux fraction. We integrate the free energy in the volume above the ROI and find it to be over 10% of that in the whole volume. For the ROI, the ratio between the NLFFF energy and the PF energy is about 1.60. This indicates the bipole is very non-potential and energetic. There is a strong concentration of current near the PIL in the lower corona, similar to the major PIL near the center of the AR (Figure 6.3(d)).

Unfortunately, we do not find a clear, step-wise change in free energy during the flare that can be used as a proxy of the energy budget (Figure 6.4(c)). Our earlier work on the ensuing X-class flare (Sun *et al.*, 2012a) suggests the energy budget tends to be underestimated by the extrapolation

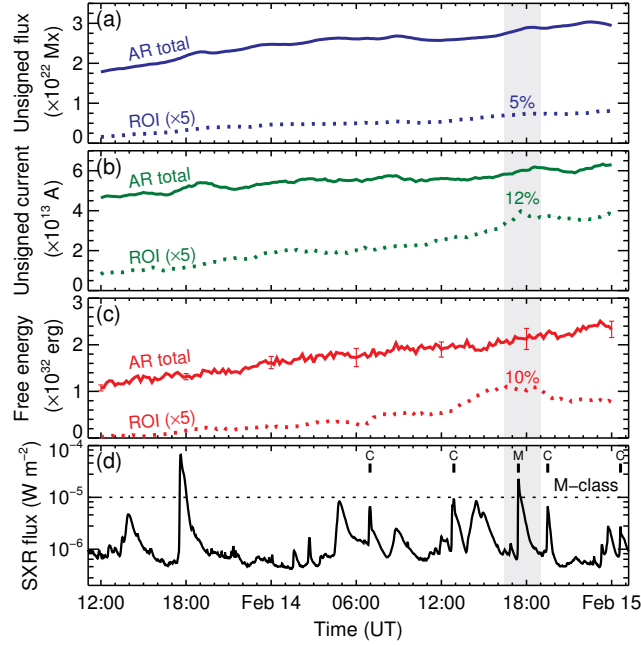


Figure 6.4: Evolution of the entire AR and the region of interest (ROI). (a) Unsigned magnetic flux. (b) Unsigned photospheric electric current. (c) Magnetic free energy evaluated in the volume above the ROI. (d) *GOES* soft X-ray flux. The homologous flares are marked with “M” and “C” according to their *GOES* X-ray class. In panels (a)-(c), solid line represents the whole AR. Dotted line is for the bipole (boxed region in Figure 6.3(a)); bipole values are multiplied by 5 for clarity. The gray vertical band indicates a 2.6-hr period that brackets the eruption, whose means are compared with the AR means. For (a) (b) only pixels with $B > 200$ G are included. Errors in (a) (b) derived from spectropolarimetry inversion are small. Errors (3σ) in panel (c) are evaluated using a pseudo Monte-Carlo method (Sun *et al.*, 2012a) which show the effect of spectropolarimetric noise.

method. This is partly because the flaring field is dynamic and likely not force-free (e.g. Gary, 2001); thus it cannot be reliably described by the NLFFF model. Limited resolution and uncertainties in the field measurement and modeling may also be a factor. The free energy for the ROI gradually decreased after 20 UT when the positive flux fragmented and the current decreased.

The emergence of the bipole led to a local enhancement of free energy with a series of ensuing eruptions from this relatively small region. Its very existence changed the original magnetic configuration and converted it into an asymmetrical (the new bipole is relatively small) quadrupolar flux system. The change of the photospheric flux distribution altered the coronal magnetic connectivity in a fundamental way, and may have contributed to the destabilization of the system. For clarity, we label the four quadrupolar components P1, N1 (including the old sunspot and the negative part of the new bipole), P2, and N2 (Figure 6.3(a)).

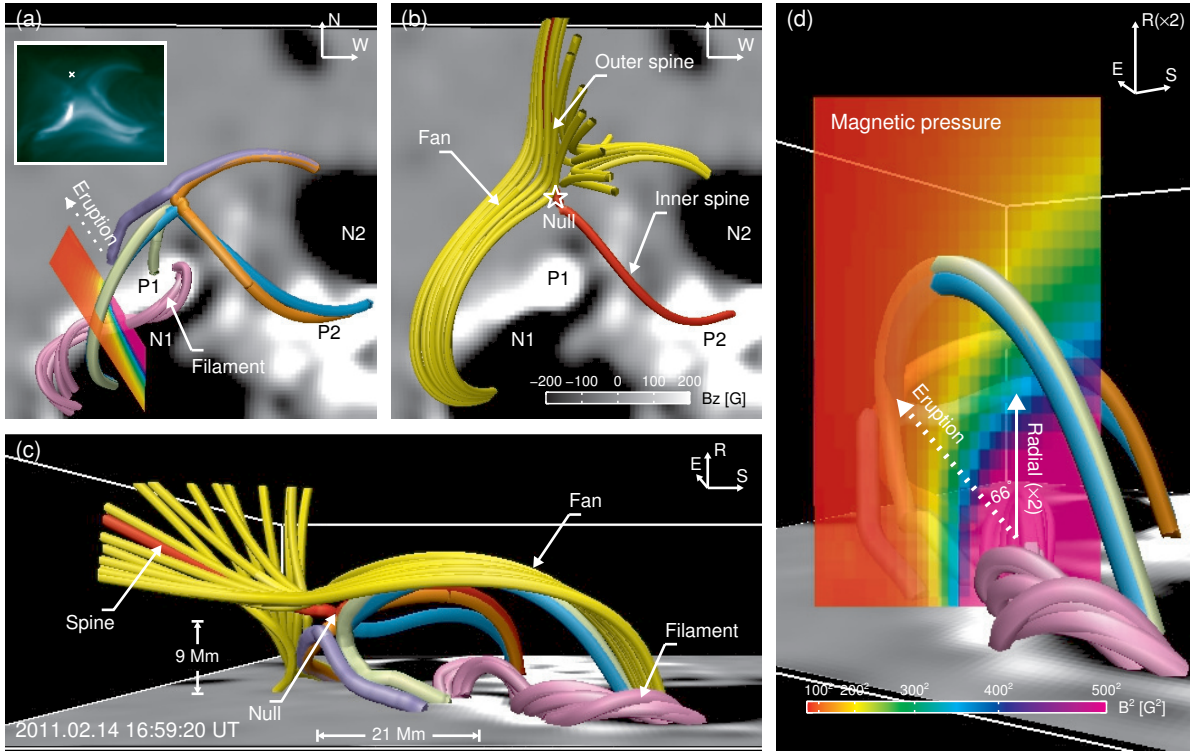


Figure 6.5: Magnetic topology based on NLFFF extrapolation for the pre-eruption state. (a) SDO view of four sets of loops connecting the four quadrupolar flux components pairwise, as well as twisted field lines below representing the AR filament. The cross section is identical to that in (d). Inset shows the corresponding AIA 94 Å image, which is the same as Figure 6.6(a). The inferred coronal null point, marked by “X”, appears slightly above the observed loops. (b) Magnetic null point, spine field line, and open field lines that outline the separatrix (fan) surface. (c) Side view of the region (from east). (d) Side view with z -axis (radial direction) stretched by 2. Magnetic pressure is imaged on a vertical cross section to illustrate its anisotropy. The cross section is roughly aligned with the direction of eruption, and is in front of the null from this viewing angle.

6.4 Interpretation Based on Magnetic Field Topology

6.4.1 Coronal Null and the Inclined Trajectory

What is the coronal magnetic field topology that led to the highly non-radial eruption? Field lines computed from the pre-flare NLFFF solution (16:59 UT) reveal connectivity between each pair of the opposite polarity flux (P1/N1, P2/N1, P2/N2, and P1/N2) in this quadrupolar system (Figure 6.5(a)). Such connectivity is apparent in the AIA observations.

One striking feature, however, is the large gradient in field line mapping. For example, loops connecting P2/N1 (cyan) and P2/N2 (orange) are at first parallel, but diverge drastically near their

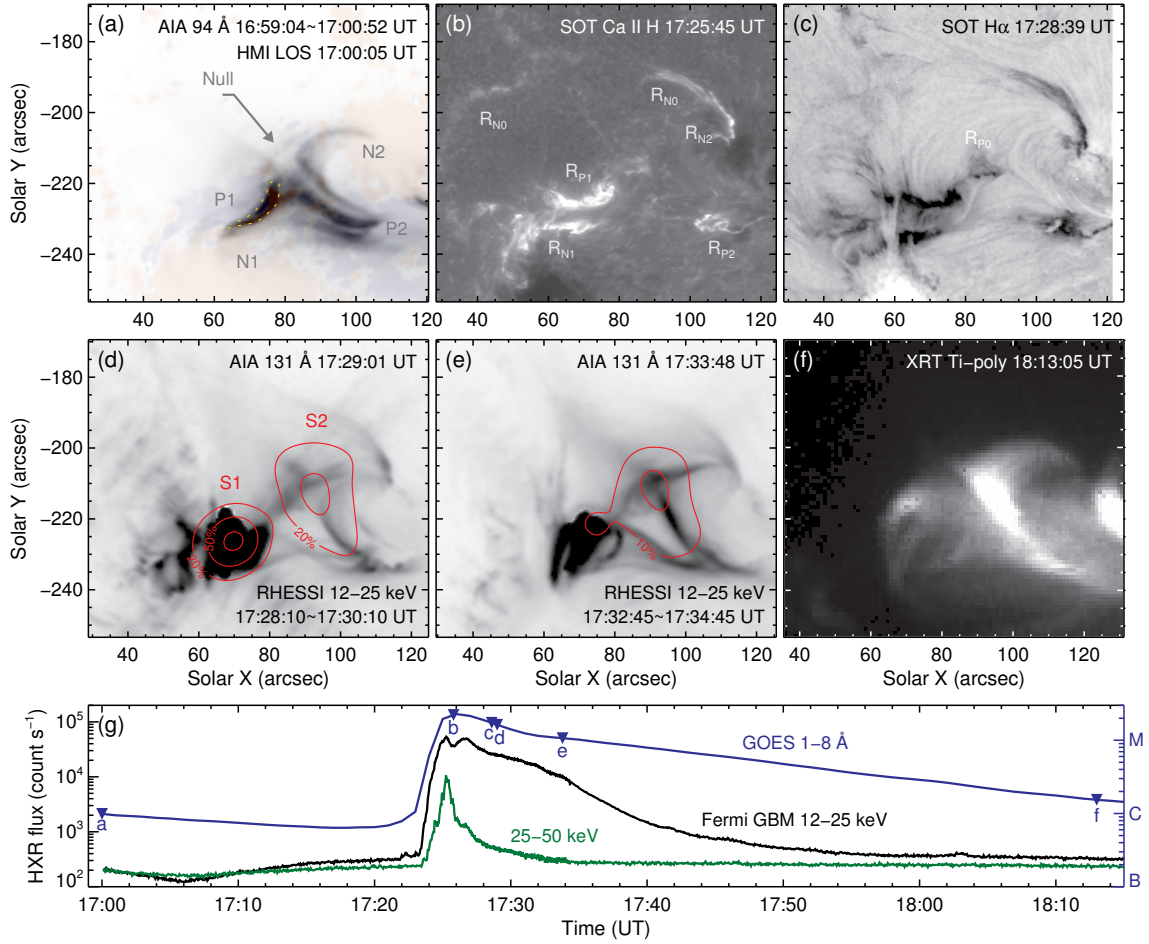


Figure 6.6: Various flare emission observations. The time of each image is marked in (g). (a) Composite of negative AIA 94 Å image (~ 6 MK, 2-minute average) and HMI LOS magnetogram showing the possible coronal null point. The AR filament is manually outlined with dotted line. The null is at $(77'', -209'')$ on the plane of sky. See also Figure 6.5(a). (b) *Hinode*/SOT Ca II H band showing flare ribbons (R_{P1} , R_{P2} , R_{N1} , R_{N2}) and the underlying photosphere. Half-ring-like secondary ribbon (R_{N0}) is also visible. (c) Unsharp masked, negative SOT H α image showing flare ribbons and magnetic connectivity. An additional, weak brightening is marked as R_{P0} . The erupting plasma is visible in the foreground from about $(60'', -250'')$ upward; the tip of the cusp is near $(45'', -160'')$. (d) *RHESSI* 12–25 keV HXR image as contours on negative AIA 131 Å image (~ 10 MK), showing a footpoint source (S1) and coronal source (S2). The two ribbons R_{P1} and R_{N1} are spatially unresolved in HXR. Contours are drawn at 20%, 50%, and 90% of maximum. (e) Same as (d), for 4 minutes later. Contours are for 10% and 25% of the maximum of (d). (f) *Hinode*/XRT SXR image, showing the cusp-like structure. (g) *GOES* SXR flux, *Fermi*/GBM 12–15 keV, and 25–50 keV HXR flux. *RHESSI* coverage of the flare started from 17:27:44 UT, and is not shown here. Panels (b)–(e) are displayed using square-root scale. All images are tracked with solar rotation and co-aligned to an accuracy better than $0.6''$.

apexes, becoming almost antiparallel with each other. These modeled field lines closely resemble

the observed loops (inset of Figure 6.5(a) or Figure 6.6(a)). The cusp-like P2/N2 and the diverging field lines strongly suggest the existence of a coronal null point, where field strength becomes zero. For example, see *TRACE* observation of AR 9147/9149 (<http://trace.lmsal.com/POD/TRACEpodarchive4.html>).

Using a trilinear method (Haynes and Parnell, 2007), we indeed find a null point situated at ~ 9 Mm height (Figure 6.5(b)) right above the modeled loop apexes (see Appendix B). From that null, closed loops “turn away” with a sharp angle. Seen from side (Figure 6.5(c)), these loops are low-lying; they incline towards the northeast, the direction of the eruption. This configuration persisted over the next few hours (see Section 6.5.1).

This inclined geometry is perhaps a natural consequence of the asymmetrical photospheric flux distribution. We infer that this field configuration may have facilitated the non-radial eruption in the following ways. First, reconnection may take place near the null point, removing the overlying flux above P1/N1 and preferentially reducing the confinement from the northeast direction. Second, the ambient, confining magnetic pressure ($p_B = \frac{B^2}{8\pi}$) is anisotropic: it drops off much faster horizontally than it does in the radial direction (Figure 6.5(d)). When the anisotropy is strong enough, it can guide the ejecta towards a direction with large negative pressure gradient by deflecting its trajectory. It effectively creates a non-radial “channel” for the plasma to escape.

6.4.2 The Inverted-Y Structure

We further analyze the magnetic topology of the pre-eruption state for insight into the observed inverted-Y shaped structure. By analyzing the Jacobian field matrix ($M_{ij} = \partial B_i / \partial x_j$) at the inferred null point, we are able to find the spine and the fan, which are special field lines that define the magnetic configuration near the singularity (e.g. Parnell *et al.*, 1996). Regular field lines passing by the immediate vicinity of the null point generally outline the separatrix (fan) surface (Figure 6.5(b)(c)). In this case they separate the closed flux inside and the open flux outside. We describe the analysis method in Appendix B.

Owing to the local excess of negative flux, open field lines from N1 and N2 flow along the separatrix and converge around the outer spine. These field lines naturally form an inverted-Y structure (Figure 6.5(b)). Its morphology resembles the observed loops, although less inclined towards the northeast. Their detailed geometry took shape during the the dynamic eruption, which the static extrapolation is unable to model.

6.4.3 Observational Evidence

Because field line mapping diverges and links the whole quadrupolar system, we expect electrons accelerated during the flare near the null point to precipitate along different loop paths, resulting in multiple pairs of flare ribbons brightening simultaneously (Shibata *et al.*, 1995). Taken by the Solar Optical Telescope (SOT; Tsuneta *et al.*, 2008) on the *Hinode* satellite, Ca II H band images (Figure 6.6(b)) indeed show such phenomena. The typical double ribbons (R_{P1}/R_{N1}) are related to the erupting filament, whereas R_{P2} and R_{N2} are likely related to the reconnecting P2/N2 loop. $H\alpha$ images (Figure 6.6(c)) provide additional information on the magnetic connectivity between R_{P1}/R_{N2} and R_{P2}/R_{N1} . In particular, the ribbon R_{P2} appears to be co-spatial with the inferred spine field line footpoint (Figure 6.5(b)), which moved with time as seen in the Ca II H and $H\alpha$ image sequences.

The *Ramaty High Energy Solar Spectroscopic Imager* (RHESSI; Lin *et al.*, 2002) missed the impulsive phase but captured what appeared to be a coronal hard X-ray (HXR) source (S2 in Figure 6.6(d)) in the flare’s early decaying phase. The source’s proximity to the inferred coronal null gives strong support to our interpretation. From the loop top, energetic electrons followed highly inclined paths towards the footpoints in P1/N1, which created the footpoint source (S1) corresponding to the R_{P1}/R_{N1} ribbons. This coronal source lasted well into the decaying phase (Figure 6.6(e)).

6.5 Discussion

6.5.1 On the Coronal Field Topology

How common is the magnetic topology determined here? A previous study focused on the quadrupolar configuration of AR 10486 during the 2003 X-17 flare (Mandrini *et al.*, 2006). The major eruption was found to involve reconnection at the quasi-separatrix layers (QSL; Démoulin *et al.*, 1996), while a smaller brightening was associated with a similar coronal null point determined using a linear force-free extrapolation. In another quadrupolar region AR 11183, similar cusp and jet structures existed at a much larger scale (Filippov, Koutchmy, and Tavabi, 2012). The white-light jet extended over multiple solar radii.

We analyze the entire 36-hr series, searching for consistency in time. The coronal null at 9 Mm appeared in a few frames early on February 14, distinct from all other candidates which were mostly below 4 Mm in weak field regions. Starting from 15:35 UT, it appeared at a nearly constant

location (within 3 Mm of the first detected null) in over half the frames afterwards (22/42, until February 15 00:00 UT), while the near-surface nulls rarely repeated in two consecutive time steps. We have applied a different null-searching method based on the Poincaré index theorem (Greene, 1992) and found similar results (23/42, 20 identical to the trilinear method, with 3 additional and 2 missed detections). The repeated detection of null points and the observed homologous eruptions (Figure 6.4(d)) suggest the aforementioned topology is characteristic for this quadrupolar system.

We compute at 1-hr cadence the “squashing factor” Q that describes the field mapping gradient (Titov, Hornig, and Démoulin, 2002) by tracing individual field lines and measuring the differences between the two footpoint locations. High- Q isosurface corresponds to QSLs. By inspecting the contour of Q at different heights, we find that multiple QSL’s tend to converge and intersect at about 9 Mm. Near the intersection, the field strength is weak, and the field line mapping gradient is invariably large, with or without a null point. This illustrates the robustness of our interpretation despite the uncertainties in the extrapolation algorithm (e.g. DeRosa *et al.*, 2009) and the field measurement. (The uncertainties nevertheless can indeed affect the detailed fan-spine configuration, as discussed in Appendix B.)

We note that our PF extrapolation, with radial field as boundary condition and the Green’s function method, does not detect any nulls above 5 Mm. Instead, we find a low-lying null at about 4 Mm in 13 frames, southwest to the NLFFF solution. The field configuration is less realistic, presumably because the current-free assumption does not agree with observation.

6.5.2 On the Flare Emissions

Owing to the LOS projection, the altitude of an on-disk HXR source cannot be unambiguously determined. We think S2 is a coronal source mainly because it appeared near the apex of cusp-shaped loops (P2/N2) which is typical for reconnecting field lines (e.g. Tsuneta, 1996). In addition, its strong HXR emission (peak at $\sim 60\%$ of the maximum) does not correspond to any bright flare ribbon. The closest chromospheric emission enhancement is a small patch (R_{P0} in Figure 6.6(c)) within a fragmented positive flux about $5''$ to the east and south, whose intensity is much weaker than the R_{P1}/R_{N1} ribbons. This argues against the footpoint source interpretation.

We notice a dimmer, half-ring-like ribbon (R_{N0}) farther north in the weak field area (Figure 6.6(b)); both $H\alpha$ (Figure 6.6(c)) and EUV images show its connection to P1. This structure is related to flux emerging into an encircling unipolar region (“anemone” AR; Shibata *et al.*, 1994). Because the brightening R_{N0} region possesses flux only a few percent of P1 (c.f. Reardon *et al.*,

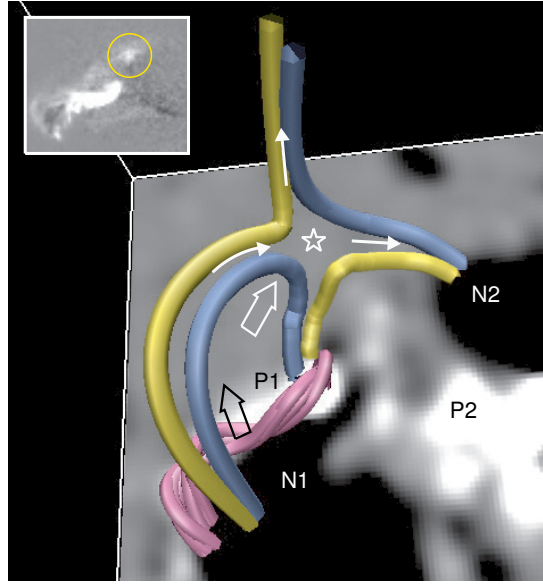


Figure 6.7: Schematic illustration of the magnetic configuration and dynamics that may have led to the eruption. The structure resembles that of a blowout jet. The arcade (blue field lines above P1/N1) from the newly emerged bipole expands, reconnects with the pre-existing field (blue field lines from N2), becomes open (yellow field lines from N1), and the low-lying sheared/twisted core field (pink field lines between P1/N1) subsequently erupts. A possible initial reconnection site nearby is marked by the star; possible motions of the loops are denoted by thick arrows. Pre- and post- reconnection field lines are colored blue and yellow, respectively. The directions of the observed, *post-eruption* flow (Figure 6.2, see also Thompson *et al.* (2011b); Su, Shen, and Liu (2012)) are denoted by thin arrows. The inset shows the SXR difference image between 17:22:32 and 17:19:56 UT from *Hinode* XRT Ti Poly filter (FOV $72'' \times 60''$). The brightening P1/N2 loop is marked by a yellow circle; the brightening filament is visible in the foreground.

2011), we consider this structure secondary. It does not affect our conclusions on the AR topology.

Because no HXR source was detected at the P2/N2 footpoints and the R_{P2}/R_{N2} ribbons were fainter than R_{P1}/R_{N1} , we think the electrons primarily precipitated along the shorter P1/N1 loop during the flare. On the other hand, the P2/N2 loop produced much stronger SXR and EUV emission during the flare’s late decaying phase. Almost 30 minutes later, SXR images (Figure 6.6(f)) from the *Hinode* X-Ray Telescope (XRT; Golub *et al.*, 2007) still showed a bright cusp structure above P2/N2.

6.5.3 On the Eruption Mechanism

When a bipole emerges, one leg of the new loop may reconnect with the oppositely directed, pre-existing open field. The released magnetic energy heats the plasma and produces field-collimated outward flows, known as the “standard” jet phenomenon (Shibata *et al.*, 1997). When the emerging

field is sheared or twisted, its core may subsequently erupt. Events in this sub-class have recently been described as “blowout” jets (Moore *et al.*, 2010).

Can this event be explained by the jet models? We find the inferred magnetic structure here resembles the blowout type. Illustrated in Figure 6.7, the newly emerged bipole (P1 and the north part of N1) hosts a twisted core field. We speculate that the increasing flux leads to the expansion of the arcade loops above, which reconnect with the open, negative-polarity field from N2. This process opens up the arcade loops and acts to promote the eventual eruption of the core field below. The jet model predicts the brightening of the reconnected P1/N2 loop, which is indeed observed in the SXR images (inset of Figure 6.7). However, different from the expected jet behavior, no outward flows are observed during this stage. The jet-like, inverted-Y structure appeared only *after* the core field eruption and the accompanying M-class flare.

Propagating brightness disturbances in the post-eruption inverted-Y structure have been interpreted as pulsed plasma flow (Su, Shen, and Liu, 2012; Tian *et al.*, 2012). The upflow from the left leg diverges and flows in opposite directions, upward in the thin spire and downward in the right leg (Figure 6.7 and Animation of Figure 6.2). The flow is most pronounced in cooler EUV wavebands (e.g. 171 Å, ~ 0.6 MK) and is absent in SXR images. In the standard jet model, these collimated flows are produced and heated by reconnection. The relatively low temperature observed here suggests a low-altitude reconnection site with cooler plasma supply (c.f. Su, Shen, and Liu, 2012), rather than the one near the base of the spire higher in the corona. The detailed dynamics of this event require further investigation which is out of the scope of this Chapter.

6.6 Summary

We summarize our findings as follows.

- Bipole emergence and shearing in a pre-existing sunspot complex introduced a large amount of free energy, despite its small flux. The new flux powered a series of homologous, non-radial eruptions.
- One typical eruption had an inclined trajectory about 66° with respect to the radial direction. An inverted-Y structure consisted of cusp and jet formed in the wake of the eruption.
- The bipole emergence created an asymmetrical quadrupolar flux system. Field extrapolation suggests that the consequent, inclined overlying loops and the anisotropic magnetic pressure are responsible for the non-radial eruption.

- Extrapolation suggests a coronal null point at about 9 Mm, slightly below the apexes of the cusp-like loops. Its location is favorable for reconnection between different flux components in the quadrupolar system. The observed inverted-Y structure is likely related to the open negative field lines in part outlining the separatrix surface.
- Multiple flare ribbons brightened simultaneously during the accompanying flare. A coronal HXR source appeared near the inferred null point. These observations support our interpretation.
- The inferred magnetic structure resembles that of a blowout-type jet. Some observed features fit in the jet model, while others remain difficult to explain.

The event studied here demonstrates the importance of detailed magnetic field topology during solar eruptions. Flux emergence in suitable environment can lead to fundamental changes in the coronal field geometry, which then place strong constraints on the plasma dynamics.

* The content of this Chapter is based on [Sun *et al.* \(2012b\)](#). All figures and a major part of the text are reproduced by permission of the AAS. I adapted the extrapolation code, performed the modeling and most of the analysis. Q. Chen analyzed the hard X-ray data. Dr. T. Wiegmann provided the original extrapolation code.

Chapter 7

Concluding Remarks

The work presented in this dissertation covers a few areas on the interpretation and modeling of the solar photospheric and coronal magnetic field, and the application of these measurements data to the space weather forecasting. The archival synoptic data enables the study of the large scale magnetic field over a solar cycle, while the newest, state-of-the-art vector field measurements make the continuous monitoring of active regions possible for the first time. During the process of data reduction, several new tools and improvements on the existing were implemented and evaluated. I summarize the major results as follows.

- The space weather forecasting scheme on solar wind (SW) speed and interplanetary magnetic field (IMF) polarity, using the Wang-Sheeley-Argue (WSA) model and the potential-field source-surface (PFSS) extrapolation, have been retrospectively optimized for the MDI archival data for solar cycle 23.
- The 3-day advanced, 4.5-h resolution SW speed prediction has a $\sim 16\%$ error over cycle 23. The IMF polarity prediction accuracy is roughly 81%. The accuracy is dependent on the detailed solar features during different activity cycle phases so the confidence level of certain predictions can be anticipated. An extrapolation algorithm that does not require the field to become radial at source surface is likely not suitable for WSA space weather prediction.
- The large-scale magnetic field in the polar region is important for global-scale modeling. A newly developed method that utilizes the best observed polar field time sequence to interpolate for missing data are tested with MDI data archive and proves to improve the modeling results.
- The large-scale coronal field inferred from the PFSS extrapolation captures many major evolution features from the observation during cycle 23. It shows that the recent quiet minimum

phase is related to a reduction of the solar magnetic field, as well as the relative strength of the dipole component. The source surface height as a free parameter in the PFSS model might need to be lowered to better match the observation during this interval.

- The new photospheric vector magnetic field sequence from HMI records the evolution history of the first major eruptive active region (AR 11158) of Cycle 24. Based on a series of non-linear force-free field (NLFFF) extrapolations, the evolving 3D distribution of the magnetic energy and current distribution are mapped. A large amount of free energy was ingested during the early flux emergence and stored in the low corona above the polarity inversion line (PIL). The computed free energy decreases by a few times 10^{31} erg during the X-class flare. The flare energy is probably intrinsically underestimated in our analysis.
- The high-cadence HMI vector field confirms rapid, irreversible photospheric magnetic field changes during flares. In the case studied, the horizontal field near the PIL increased by $\sim 30\%$. The changed lower boundary is consistent with the “magnetic implosion” scenario in which the coronal structure contracts inward. This is in line with the extrapolation as well as coronal extreme-ultraviolet (EUV) loop observation.
- Modeling of an asymmetrical quadrupolar AR reveals a clear coronal null point, which is also evident in coronal imaging in various wavelengths. A series of homologous eruptions took place in the region. They can be naturally explained by the inclined magnetic geometry: reconnection at the null point may preferentially remove the overlying flux from one direction, and the anisotropic magnetic pressure may guide the ejecta during the initial stage of the eruption.

As the current solar activity cycle moves towards its maximum phase, strong magnetic fields appear frequently. We are starting to gather a statistically significant sample of vector field measurements. Their evolution in three dimensions can now be studied consistently. Realistic solar models with vector input can now be tested with suitable input that will help us learn more about the dynamic events on the Sun. Several topics as the natural extension of this dissertation may be pursued in the near future.

- *A more accurate description of polar magnetic field polarity reversal.* The process of the polar field reversal is of great importance to solar cycle variation. It has been extensively explored using the time sequence of LOS field measurements (e.g. [Hoeksema, 1984](#); [Wang, Nash, and](#)

Sheeley, 1989a; Liu and Zhao, 2009), flux-transport modeling (e.g. Wang, Nash, and Sheeley, 1989b), or a small number of vector measurements (e.g. Shiota *et al.*, 2012). With the ongoing reversal of cycle 24 and the newly available HMI vector data stream, we may be able to study this process in a realistic and consistent fashion.

- *Statistical survey of AR magnetic energy, topology, and their relation to explosive events.* Developing an empirical correlations between an AR’s magnetic structure and its capability to host major explosive events requires a large sample for reliable statistics. Such work has been done for the LOS field using the complete MDI data archive for the last solar cycle (Leka and Barnes, 2003; Leka and Barnes, 2007; Falconer, Moore, and Gary, 2006; Mason and Hoeksema, 2010), and is now possible for cycle 24, with more accurate LOS and vector measurements, from the HMI instrument.
- *Improved magnetic modeling algorithms.* It is now clear that most of the major ARs deviate far from the potential or linear force-free state, thus require a more realistic NLFFF modeling. Nevertheless, the existing algorithms suffer some intrinsic problems (DeRosa *et al.*, 2009). Ongoing efforts to improve the model includes: more realistic treatment of the boundary condition (Yamamoto and Kusano, 2012); incorporating error estimation in the extrapolation to minimize the negative effect from noise (Wiegelmann *et al.*, 2012; Gilchrist, Wheatland, and Leka, 2012); magneto-friction model with evolving boundary condition that utilizes the electric field derived from the measured vector magnetic field with Doppler velocity constraint (Fisher, Welsch, and Abbett, 2012; DeRosa and Cheung, 2012; Welsch and Fisher, 2012); implementation of the algorithm in spherical coordinate so it can be applied to a large region of interest with correct geometry (Tadesse *et al.*, 2012). Improvements are likely as we gain more experience.

Appendix A

Global Potential-like Magnetic Field Extrapolation

A.1 Basic Equations

A commonly used version of PFSS model ([Hoeksema, 1984](#); [Wang and Sheeley, 1992](#)) takes global radial Carrington synoptic maps as input. In these maps, photospheric fields are sampled on a heliographic coordinate, evenly spaced either in latitude or sine-latitude steps. If the field is purely potential, we have

$$\vec{B} = -\nabla\Psi, \quad (\text{A.1})$$

where

$$\nabla^2\Psi = 0. \quad (\text{A.2})$$

We assume the existence of a spherical “source surface” at a radius of R_s (usually at $2.5R_\odot$), beyond which all field lines are open and radius. The potential arises from both inside the inner boundary R_0 (photosphere, or R_\odot) and outside the outer boundary, or the source surface:

$$\Psi = \Psi_I + \Psi_O, \quad (\text{A.3})$$

with

$$\Psi_I = \sum_{l=0}^{\infty} r^{-(l+1)} \sum_{m=-l}^l f_{I_{lm}} Y_{lm}(\theta, \phi), \quad (\text{A.4})$$

$$\Psi_O = \sum_{l=0}^{\infty} r^l \sum_{m=-l}^l f_{O_{lm}} Y_{lm}(\theta, \phi). \quad (\text{A.5})$$

Scale r in terms R_\odot for Ψ_I and in terms of R_s for Ψ_O . Use the fact that

$$Y_{lm}(\theta, \phi) = k_{lm} P_l^m(\cos \theta) e^{im\phi}. \quad (\text{A.6})$$

The real part of Ψ can be generalized from Equations A.3 through A.6:

$$\begin{aligned} \Psi = R_0 \sum_{l=0}^{\infty} \sum_{m=0}^l P_l^m(\cos \theta) & \left\{ g'_{lm} \cos m\phi \left[\left(\frac{R_0}{r} \right)^{l+1} + \frac{R_s}{R_0} \left(\frac{r}{R_s} \right)^l c_{lm} \right] \right. \\ & \left. + h'_{lm} \sin m\phi \left[\left(\frac{R_0}{r} \right)^{l+1} + \frac{R_s}{R_0} \left(\frac{r}{R_s} \right)^l d_{lm} \right] \right\}, \end{aligned} \quad (\text{A.7})$$

where g'_{lm} , h'_{lm} , c_{lm} and d_{lm} are the unknown coefficients. Note that the normalization of the spherical harmonics and associated Legendre functions can be tricky. We will simply present the normalization we adopted here and leave the detailed description to Section A.2.

By definition, the field lines turn radial at the source surface. This means the field vector is purely radial at R_s , or rather, the potential is a constant on the source surface. Since we are only interested in the field as the first derivative of this potential, we set this potential to 0. We then have

$$c_{lm} = d_{lm} = - \left(\frac{R_0}{R_s} \right)^{l+2} = c_l. \quad (\text{A.8})$$

Now our sole task is to determine g'_{lm} and h'_{lm} , using the inner boundary condition (photospheric field). Write B_r from Equation A.1 specifically:

$$\begin{aligned} B_r(r, \theta, \phi) = -\frac{\partial \Psi}{\partial r} = \sum_{lm} P_l^m(\cos \theta) (g'_{lm} \cos m\phi + h'_{lm} \sin m\phi) \\ \left[(l+1) \left(\frac{R_0}{r} \right)^{l+2} - l \left(\frac{r}{R_s} \right)^{l-1} c_l \right]. \end{aligned} \quad (\text{A.9})$$

At inner boundary, we have

$$B_r(R_0, \theta, \phi) = \sum_{l=0}^{\infty} \sum_{m=0}^l P_l^m(\cos \theta) (g_{lm} \cos m\phi + h_{lm} \sin m\phi), \quad (\text{A.10})$$

where

$$g_{lm} = g'_{lm} \left[l + 1 + l \left(\frac{R_0}{R_s} \right)^{2l+1} \right], \quad (\text{A.11})$$

$$h_{lm} = h'_{lm} \left[l + 1 + l \left(\frac{R_0}{R_s} \right)^{2l+1} \right]. \quad (\text{A.12})$$

Now we make use of the orthogonal property of the associated Legendre function (in our convention)

$$\int_0^{2\pi} d\phi \int_0^\pi \sin \theta d\theta P_l^m(\cos \theta) \frac{\cos}{\sin} m\phi P_{l'}^{m'}(\cos \theta) \frac{\cos}{\sin} m'\phi = \frac{4\pi}{2l+1} \delta_{ll'} \delta_{mm'}. \quad (\text{A.13})$$

Note when $m = 0$ Equation A.13 holds for the $\cos m\phi$ case, while the $\sin m\phi$ case simply yields 0.

An integration of Equation A.10 then shows us how to obtain g and h . Here, h_{l0} is obviously 0.

$$\int_0^{2\pi} d\phi \int_0^\pi \sin \theta d\theta B_r(R_0, \theta, \phi) P_l^m(\cos \theta) \frac{\cos}{\sin} m\phi = \frac{4\pi}{2l+1} \frac{g_{lm}}{h_{lm}}. \quad (\text{A.14})$$

For a synoptic map ($X \times Y$) in sine-latitude format, the Equation A.14 becomes

$$\begin{pmatrix} g_{lm} \\ h_{lm} \end{pmatrix} = \frac{2l+1}{XY} \sum_{i=1}^X \sum_{j=1}^Y B_r(R_0, \theta_i, \phi_j) P_l^m(\cos \theta_i) \frac{\cos}{\sin} m\phi_j. \quad (\text{A.15})$$

Thus the potential is solved. There are other ways to compute g and h , as we will see in Section A.3.

To conclude, we have the solutions in the following form.

$$B_r(r, \theta, \phi) = -\frac{\partial \Psi}{\partial r} = \sum_{l=0}^{\infty} \sum_{m=0}^l P_l^m(\cos \theta) (g_{lm} \cos m\phi + h_{lm} \sin m\phi) \times \left(\frac{R_0}{r} \right)^{l+2} \left[l + 1 + l \left(\frac{r}{R_s} \right)^{2l+1} \right] \bigg/ \left[l + 1 + l \left(\frac{R_0}{R_s} \right)^{2l+1} \right], \quad (\text{A.16})$$

$$B_\theta(r, \theta, \phi) = -\frac{1}{r} \frac{\partial \Psi}{\partial \theta} = -\sum_{l=0}^{\infty} \sum_{m=0}^l \frac{\partial P_l^m(\cos \theta)}{\partial \theta} (g_{lm} \cos m\phi + h_{lm} \sin m\phi) \times \left(\frac{R_0}{r} \right)^{l+2} \left[1 - \left(\frac{r}{R_s} \right)^{2l+1} \right] \bigg/ \left[l + 1 + l \left(\frac{R_0}{R_s} \right)^{2l+1} \right], \quad (\text{A.17})$$

$$B_\phi(r, \theta, \phi) = -\frac{1}{r \sin \theta} \frac{\partial \Psi}{\partial \phi} = \sum_{l=0}^{\infty} \sum_{m=0}^l P_l^m(\cos \theta) (g_{lm} \sin m\phi - h_{lm} \cos m\phi) \times \left(\frac{R_0}{r} \right)^{l+2} \left[1 - \left(\frac{r}{R_s} \right)^{2l+1} \right] \Bigg/ \left[l + 1 + l \left(\frac{R_0}{R_s} \right)^{2l+1} \right], \quad (\text{A.18})$$

where g and h are determined by Equation A.15.

A.2 Issues on Normalization

The associated Legendre functions may have different normalization conventions in different cases. From Equation A.13, in our scheme we have

$$\int_{-1}^1 |P_l^m(x)|^2 dx = \frac{2}{2l+1} (2 - d_0), \quad d_0 = \begin{cases} 1, & m = 0 \\ 0, & m \neq 0 \end{cases}. \quad (\text{A.19})$$

A more widely used form is

$$\int_{-1}^1 |\tilde{P}_l^m(x)|^2 dx = \frac{2(l+m)!}{(2l+1)(l-m)!}, \quad 0 \leq m \leq l, \quad (\text{A.20})$$

with the following properties

$$\tilde{P}_l^{-m}(x) = (-1)^m \frac{(l-m)!}{(l+m)!} \tilde{P}_l^m(x), \quad (\text{A.21})$$

$$\tilde{P}_l^l(x) = (-1)^l (2l-1)!! (1-x^2)^{l/2}, \quad (\text{A.22})$$

$$(l-m+1)\tilde{P}_{l+1}^m(x) = (2l+1)x\tilde{P}_l^m(x) - (l+m)\tilde{P}_{l-1}^m(x). \quad (\text{A.23})$$

Two sets of Legendre functions are related by

$$P_l^m(x) = (-1)^m \sqrt{\frac{(l-m)!}{(l+m)!}} \sqrt{2-d_0} \tilde{P}_l^m(x). \quad (\text{A.24})$$

So in our convention Equations A.21 through A.23 become

$$P_l^{-m}(x) = (-1)^m P_l^m(x), \quad (\text{A.25})$$

$$P_l^l(x) = \sqrt{\frac{(2l-1)!!}{(2l)!!}} \sqrt{2-d_0} (1-x^2)^{l/2}, \quad (\text{A.26})$$

$$\sqrt{(l+1)^2 - m^2} P_{l+1}^m(x) = (2l+1)x P_l^m(x) - \sqrt{l^2 - m^2} P_{l-1}^m(x). \quad (\text{A.27})$$

Equation A.24 can be used to convert standard Legendre functions for our use. Equations A.25 through A.27 can be used recursively to generate our own set of Legendre functions.

A.3 Alternative Method for Computing g and h

We may alternatively utilize the a different normalization (e.g. Schou and Brown, 1994). If the signal on the photosphere at a particular moment is $f(\theta, \phi)$, then

$$f(\theta, \phi) = \sum_{l=0}^{\infty} \sum_{m=-l}^l f_l^m Y_l^m(\theta, \phi), \quad f_l^m \in \mathcal{C}, \quad (\text{A.28})$$

with the following normalization

$$\int_0^{2\pi} d\phi \int_0^{\pi} \sin \theta d\theta Y_l^m(\theta, \phi) Y_{l'}^{m'*}(\theta, \phi) = 4\pi \delta_{ll'} \delta_{mm'}. \quad (\text{A.29})$$

In the most common version,

$$Y_l^{-m} = (-1)^m Y_l^{m*}. \quad (\text{A.30})$$

Consider Equations A.6, A.20, A.29 and A.30, we have

$$Y_l^m(\theta, \phi) = \sqrt{(2l+1) \frac{(l-m)!}{(l+m)!}} \tilde{P}_l^m(\theta) e^{im\phi}, \quad (\text{A.31})$$

where \tilde{P}_l^m is defined in Equation A.20. So we have the following expansion:

$$\begin{aligned} f_l^m &= \frac{1}{4\pi} \int_0^{2\pi} d\phi \int_0^{\pi} \sin \theta f(\theta, \phi) Y_l^{m*}(\theta, \phi) \\ &= \frac{1}{4\pi} \int_0^{2\pi} d\phi \int_0^{\pi} \sin \theta f(\theta, \phi) \sqrt{(2l+1) \frac{(l-m)!}{(l+m)!}} \tilde{P}_l^m(\theta) e^{-im\phi} \\ &= \frac{(-1)^m}{4\pi} \sqrt{\frac{2l+1}{2-d_0}} \int_0^{2\pi} d\phi \int_0^{\pi} \sin \theta f(\theta, \phi) P_l^m(\theta) e^{-im\phi}. \end{aligned} \quad (\text{A.32})$$

Compare this with Equation A.15, we find the connection

$$g_{lm} = (-1)^m \sqrt{(2l+1)(2-d_0)} \Re(f_l^m), \quad (\text{A.33})$$

$$h_{lm} = -(-1)^m \sqrt{(2l+1)(2-d_0)} \Im(f_l^m). \quad (\text{A.34})$$

A.4 PFSS-Like Models

A thin layer of current may exist near the zero radial polarity inversion surface, creating a jump in B_r without greatly altering the global field topology. Schatten (1971) proposed a model called potential-field current-sheet (PFCS) that includes the effect of the current sheets in streamers. Zhao and Hoeksema (1994) provided a modified horizontal-current current-sheet model (HCCS) that introduces the effect of horizontal current, based on a solution of the magneto-hydrostatic equations (Bogdan and Low, 1986). Later, Zhao and Hoeksema (1995) revised the HCCS model, adding a source surface at a higher altitude. This new model is called horizontal-current current-sheet source-surface (HCCSSS) model.

A brief summary on their characteristics:

- Generally, these PFSS-like models divide the solar atmosphere into different regions.
- Below a certain altitude (denoted by R_c from here on), the field does not contain the current sheet. Above R_c , the current sheet comes in. R_c is usually taken to be $2.5R_\odot$.
- Models have different boundary conditions on R_c . The PFCS model requires the field to be radial there, similar to the PFSS model on the source surface. The HCCS and HCCSSS does not have such constraint. On the other hand, the HCCSSS model introduces another source surface higher up (R_{ss}) near the Alfvén critical point, where the field is required to be radial. R_{ss} is usually taken to be about $20R_\odot$.
- Both the HCCS and HCCSSS models include a parameterized, volume-filling horizontal current.

We generalize the algorithm by a uniform presentation, following Zhao and Hoeksema (1994, 1995). The field away from the current sheet can always be expressed by from a potential function

Table A.1: Various forms of $R_l(r)$ in different models for Equation A.36

Model	Lower Region ^a	Upper Region ^b
PFSS	$R_0 \frac{(\frac{R_0}{r})^{l+1} [1 - (\frac{r}{R_s})^{2l+1}]}{l + 1 + l(\frac{R_0}{R_s})^{2l+1}}$	N.A.
PFCS	$R_0 \frac{(\frac{R_0}{r})^{l+1} [1 - (\frac{r}{R_s})^{2l+1}]}{l + 1 + l(\frac{R_0}{R_s})^{2l+1}}$	$R_s^2 \frac{R_s^l}{(l+1)r^{l+1}}$
HCCS	$R_0^2 \frac{(R_0 + a)^l}{(l+1)(r+a)^{l+1}}$	$R_c^2 \frac{(R_c + a)^l}{(l+1)(r+a)^{l+1}}$
HCCSSS	$R_0^2 \frac{(R_0 + a)^l}{(l+1)(r+a)^{l+1}}$	$R_c^2 \frac{\frac{1}{(r+a)^{l+1}} - \frac{(r+a)^l}{(R_s+a)^{2l+1}}}{\frac{l+1}{(R_c+a)^l} + \frac{l(R_c+a)^{l+1}}{(R_s+a)^{2l+1}}}$

^a The lower boundary for this region is at the solar surface, $r = R_\odot$. The upper boundary is at a certain radius, which is usually taken to be $r = 2.5R_\odot$. It is termed “source surface” for the PFSS and PFCS models and is denoted as R_s in the table. It is termed “cusp surface” for the HCCS and HCCSSS models. The field is required to be radial at the upper boundary R_c for the first two models. It is free for the other two (see discussion in Section 2.5).

^b The lower boundary for this region is just upper boundary of the lower region, usually take to be $r = 2.5R_\odot$. For the PFCS and HCCS model, there is no upper boundary. For the HCCSSS model, there is an upper boundary at $r = R_s$, which is termed source surface here, and is usually taken to be around $20R_\odot$. The field is required to be radial there outward. Field in this region is obtained using Schatten’s least-square fitting technique (Schatten, 1971), except for the PFSS model in which the field is simply radial.

Ψ , even when a volume current is present:

$$\Psi(r, \theta, \phi) = \sum_{l=0}^{\infty} \sum_{m=0}^l R_l(r) P_l^m(\cos \theta) (g_{lm} \cos m\phi + h_{lm} \sin m\phi). \quad (\text{A.35})$$

Note only the function $R_l(r)$ varies in form in different models.

The expression of the magnetic field is:

$$\vec{B} = -\eta(r) \frac{\partial \Psi}{\partial r} \hat{r} - \frac{1}{r} \frac{\partial \Psi}{\partial \theta} \hat{\theta} - \frac{1}{r \sin \theta} \frac{\partial \Psi}{\partial \phi} \hat{\phi}, \quad (\text{A.36})$$

where

$$\eta(r) = \left(1 + \frac{a}{r}\right)^2, \quad (\text{A.37})$$

in which a parameterizes the length scale of horizontal electric current in the corona. Note when $a = 0$ it simply returns to a model without horizontal current, i.e. PFSS.

The potential function Ψ is determined by boundary conditions on R_\odot , R_c , and R_{ss} . In the region without current sheet, Ψ can be calculated in a similar fashion as for the PFSS model. For the region with current sheet, we use Schattens least-square technique (Schatten, 1971) to obtain the solution. Field with negative polarity on the source surface (or cusp surface) is reversed, and Laplace's equation is solved to determine the field outside. Finally, the original polarity is restored. A least square matching procedure is employed while computing the field outside R_s , so the discontinuity of the tangential field on the boundary is minimized. These procedures introduce a finite layer of current sheet between regions of opposite polarity beyond R_s . We summarize the function R_l in Ψ for each method in Table A.1. The boundary conditions for each model is described in the notes of the table. A comparative study of these models when used for space weather forecasting can be found in Section 2.5.

Appendix B

Magnetic Field Topology Near A Null Point

Here we describe the procedures for analyzing the magnetic field topology near a null point. The procedures are based on the works of [Parnell *et al.* \(1996\)](#), [Haynes and Parnell \(2007\)](#), and [Haynes and Parnell \(2010\)](#). We present only the case that is relevant to Chapter 6 and numerically evaluate for the null point studied there.

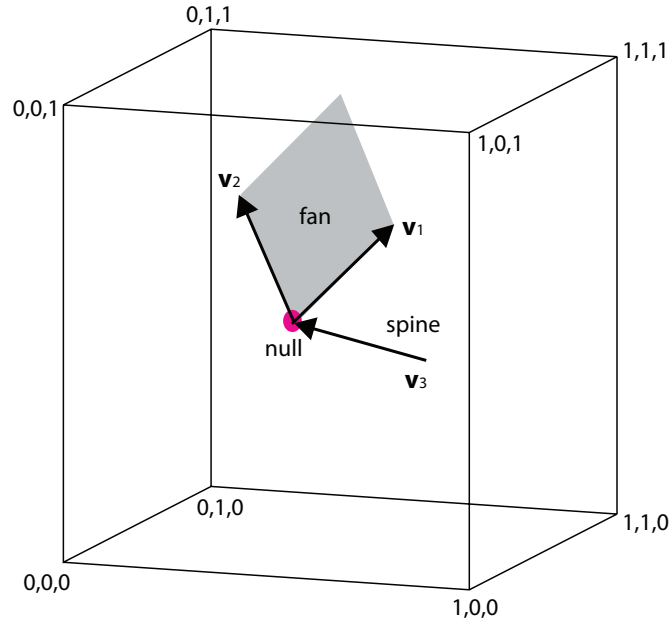


Figure B.1: Diagram illustrating the spine field line and the fan plane for a type- B null point.

B.1 Searching for Null Points

At a magnetic null point, field strength becomes 0, and singularity arises. We assume the computation resolution is high enough that the sub-grid structure is trilinear. The 3D field $\mathbf{B} = (B_1, B_2, B_3)^T$ and its derivatives $(\partial B_i / \partial x_j, i, j = 1, 2, 3)$ within each cell $(0 \leq x_i \leq 1)$ is then completely determined by the values on its eight vertices. That is,

$$B_i(x_1, x_2, x_3) = a + b x_1 + c x_2 + d x_3 + e x_1 x_2 + f x_2 x_3 + g x_3 x_1 + h x_1 x_2 x_3. \quad (\text{B.1})$$

The coefficients (a, b, \dots, h) are completely determined by the 8 values at the vertices of the cell (Figure B.1), i.e.,

$$\begin{aligned} a &= B_i^{000}, \\ b &= B_i^{100} - B_i^{000}, \\ c &= B_i^{010} - B_i^{000}, \\ d &= B_i^{001} - B_i^{000}, \\ e &= B_i^{110} - B_i^{100} - B_i^{010} + B_i^{000}, \\ f &= B_i^{011} - B_i^{010} - B_i^{001} + B_i^{000}, \\ g &= B_i^{101} - B_i^{001} - B_i^{100} + B_i^{000}, \\ h &= B_i^{111} - B_i^{110} - B_i^{011} - B_i^{101} + B_i^{100} + B_i^{010} + B_i^{001} - B_i^{000}, \end{aligned} \quad (\text{B.2})$$

where $B_i^{000} = B_i(0, 0, 0)$, etc.

To search for possible null points, we first scan over each cell in the domain: if any B_i 's have the same sign on all the vertices, the cell cannot host a null point and will be ignored.

Secondly, the null point must lie on all of the following curves: $B_x = B_y = 0$, $B_y = B_z = 0$, $B_z = B_x = 0$. Generally, these curves have to pierce the cell walls in pairs. We thus look on the six walls for points that satisfy $B_x = B_y = 0$, etc., and eliminate those cells with fewer than two such points.

For each remaining cell, we use a Newton-Raphson scheme to iteratively solve for $\mathbf{x} = (x_1, x_2, x_3)^T$ that satisfies $B_i(\mathbf{x}) = 0$:

$$\mathbf{x}^{n+1} = \mathbf{x}^n - \left(\frac{\partial \mathbf{B}(\mathbf{x}^n)}{\partial \mathbf{x}^n} \right)^{-1} \mathbf{B}(\mathbf{x}^n), \quad (\text{B.3})$$

where n and $n+1$ denote two consecutive iteration steps, and the repeated index j means summing of all j 's.

For the 2011 February 14 16:59 UT frame of AR 11158, we find a null point at $\mathbf{x} = (89.2425, 173.8625, 12.7667)^T$ in the $(300 \times 300 \times 256)$ domain. At a 720 km resolution, its height is about 9.2 Mm. The field strength satisfies $|B| < 10^{-6}$ G.

B.2 Spine and Fan Field Lines

To first order, the magnetic field near a null point located at \mathbf{x}' is approximated by

$$B_i = M_{ij}(x_j - x'_j), \quad (\text{B.4})$$

where the matrix $M_{ij} = \partial B_i / \partial x_j$ is the Jacobian matrix, and is evaluated in this case as

$$M_{ij} = \begin{pmatrix} \partial B_1 / \partial x_1 & \partial B_1 / \partial x_2 & \partial B_1 / \partial x_3 \\ \partial B_2 / \partial x_1 & \partial B_2 / \partial x_2 & \partial B_2 / \partial x_3 \\ \partial B_3 / \partial x_1 & \partial B_3 / \partial x_2 & \partial B_3 / \partial x_3 \end{pmatrix} = \begin{pmatrix} -2.4429 & 9.4865 & -4.5498 \\ 4.4430 & 1.4220 & 2.7926 \\ -6.0043 & 0.6362 & 0.8396 \end{pmatrix}, \quad (\text{B.5})$$

assuming a grid size of 1 and a unit of Gauss. Note that the local electric current (\mathbf{J}) and the Lorentz force (\mathbf{F}) is completely determined by M_{ij} as well.

The behavior of \mathbf{B} near the singularity is represented by the three eigenvectors \mathbf{v}_1 , \mathbf{v}_2 , and \mathbf{v}_3 of M_{ij} . We find the eigenvectors and their corresponding eigenvalues λ_1 , λ_2 , and λ_3 to be:

$$\begin{aligned} \lambda_1 &= 5.4421, & \mathbf{v}_1 &= (0.6118, 0.1347, -0.7795)^T, \\ \lambda_2 &= 4.4599, & \mathbf{v}_2 &= (-0.5130, 0.0380, 0.8575)^T, \\ \lambda_3 &= -10.0833, & \mathbf{v}_3 &= (0.7870, -0.4148, 0.4568)^T. \end{aligned} \quad (\text{B.6})$$

In this case, all three eigenvalues are real with one negative and two positives. The eigenvector \mathbf{v}_3 with the sole negative eigenvalue λ_3 determines the initial direction of the “spine” field line. The other two eigenvectors \mathbf{v}_1 and \mathbf{v}_2 define the “fan” plane; whereas the linear combination of them gives the initial directions of the “fan” field lines (Figure B.1). The fan field lines define the separatrix (fan) surface, which separates different domains of magnetic flux.

In practice, field lines traced slightly away from the null in the fan plane tend to flow along the separatrix surface. Here the traced field lines rapidly converge into two groups connecting to the two negative sunspots, forming a “dome” structure that looks almost two-dimensional (see Chapter 6).

B.3 Classification of Null Point

The one negative and two positive real eigenvalues classify the null point as “positive” (fan field lines going outward). The spine field line flows into the null, while the fan field lines flow out of the null.

The spine is close to but not exactly perpendicular to the fan surface: $\mathbf{v}_1 \cdot \mathbf{v}_3 = 0.0696$ (86°), $\mathbf{v}_2 \cdot \mathbf{v}_3 = -0.0278$ (92°). More interestingly, $\mathbf{v}_1 \cdot \mathbf{v}_2 = -0.9771$, so the two eigenvectors are 168° with respect to each other, almost antiparallel. This forms a skewed “improper null”, owing to the currents components parallel to the spine as well as perpendicular to it.

The current at the null is $\mathbf{j} = (-2.1564, 1.4545, -5.0435)^T$, assuming $\mu_0 = 1$. We rotate the base vectors of our coordinate such that the new z -axis is parallel to the spine (\mathbf{v}_3). The current \mathbf{j} can be decomposed to two orthogonal components, one along the z -axis (j_\parallel), one perpendicular to that (j_\perp). We choose the new x -axis to be the direction of j_\perp . The new base vectors $\mathbf{e}_1, \mathbf{e}_2, \mathbf{e}_3$ can be obtained by:

$$\begin{aligned} \mathbf{e}_3 &= \mathbf{v}_3 = (0.7870, -0.4148, 0.4568)^T \\ \mathbf{e}_1 &= \frac{\mathbf{j} - (\mathbf{j} \cdot \mathbf{v}_3)\mathbf{v}_3}{|\mathbf{j} - (\mathbf{j} \cdot \mathbf{v}_3)\mathbf{v}_3|} = (0.4422, -0.1372, -0.8864)^T \\ \mathbf{e}_2 &= \mathbf{e}_3 \times \mathbf{e}_1 = (0.4303, 0.8995, 0.0754)^T \end{aligned} \quad (\text{B.7})$$

Define matrix \mathbf{P} as

$$\mathbf{P} = (\mathbf{e}_1, \mathbf{e}_2, \mathbf{e}_3) = \begin{pmatrix} 0.4422 & 0.4303 & 0.7870 \\ -0.1372 & 0.8995 & -0.4148 \\ -0.8864 & 0.0754 & 0.4568 \end{pmatrix}. \quad (\text{B.8})$$

We can rotate the matrix \mathbf{M} into \mathbf{M}' , using the new basis $\mathbf{e}_1, \mathbf{e}_2$, and \mathbf{e}_3 :

$$\mathbf{M}' = \mathbf{P}^{-1} \mathbf{M} \mathbf{P} = \mathbf{P}^T \mathbf{M} \mathbf{P} = 3.9173 \times \begin{pmatrix} 1.0000 & 1.1275 & 0.00000 \\ -0.0478 & 1.5278 & 0.00000 \\ 0.0000 & 0.8469 & -2.5741 \end{pmatrix}. \quad (\text{B.9})$$

Equation (14) in [Parnell et al. \(1996\)](#) shows the general form of \mathbf{M} :

$$\mathbf{M} = \begin{pmatrix} 1 & \frac{1}{2}(q - j_\parallel) & 0 \\ \frac{1}{2}(q + j_\parallel) & p & 0 \\ 0 & j_\perp & -(p + 1) \end{pmatrix}. \quad (\text{B.10})$$

Compare Equations B.9 and B.10, we have

$$p \approx 1.551, q = 1.080, j_{\perp} = 0.847, j_{\parallel} = -1.175, j_{thresh} = \sqrt{(p-1)^2 + q^2} = 1.212. \quad (\text{B.11})$$

We see $|j_{\parallel}| < j_{thresh}$, $j_{\perp} \neq 0$, and $j_{\parallel} \neq 0$. This is the third case, or Figure 6(e) in Parnell *et al.* (1996) Section V A.

B.4 Error Estimation

The trace of M_{ij} is just $\nabla \cdot \mathbf{B}$ and should vanish. However, because of the linearization (when there might be sub-grid structures) and the computational errors, the zero divergence is not strictly satisfied. Here we estimate the relative error in calculating M_{ij} to be $|\nabla \cdot \mathbf{B}| / |\nabla \times \mathbf{B}| = 3.2\%$ (Xiao *et al.*, 2006).

We note that in some frames in the time series, multiple null points appear in adjacent computational cells near the modeled loop apexes. Both positive and negative nulls exist in the sample, although the morphology of the closed loops remains similar. Such behavior may be related to the uncertainties in modeling and data, but the detail is unclear.

* The content of this Chapter is partly based on Sun *et al.* (2012b). A major part of the text is reproduced by permission of the AAS.

Bibliography

- Abramenko, V., Yurchyshyn, V., Linker, J., Mikić, Z., Luhmann, J., Lee, C.O.: 2010, Low-latitude coronal holes at the minimum of the 23rd solar cycle. *Astrophys. J.* **712**, 813. doi:[10.1088/0004-637X/712/2/813](https://doi.org/10.1088/0004-637X/712/2/813). 30, 59
- Altschuler, M.A., Newkirk, G. Jr.: 1969, Magnetic fields and the structure of the solar corona. *Sol. Phys.* **9**(1), 131. doi:[10.1007/BF00145734](https://doi.org/10.1007/BF00145734). 13, 18, 63
- Arge, C.N., Pizzo, V.J.: 2000, Improvement in the prediction of solar wind conditions using near-real time solar magnetic field updates. *J. Geophys. Res.* **105**(A5), 10465. doi:[10.1029/1999JA900262](https://doi.org/10.1029/1999JA900262). 8, 18, 21, 39
- Arge, C.N., Luhmann, J.G., Odstrčil, D., Schrijver, C.J., Li, Y.: 2004, Stream structure and coronal sources of the solar wind during the May 12th, 1997 CME. *J. Atmos. Sol. Terr. Phys.* **66**, 1295. doi:[10.1016/j.jastp.2004.03.018](https://doi.org/10.1016/j.jastp.2004.03.018). 19
- Aschwanden, M.J.: 2004, *Physics of the solar corona: An introduction.*, Praxis Publishing Ltd., Chichester, UK. 3
- Aschwanden, M.J., Schrijver, C.J.: 2011, Coronal loop oscillations observed with atmospheric imaging assembly –kink mode with cross-sectional and density oscillations. *Astrophys. J.* **736**, 102. doi:[10.1088/0004-637X/736/2/102](https://doi.org/10.1088/0004-637X/736/2/102). 89
- Aulanier, G., Démoulin, P.: 2003, Amplitude and orientation of prominence magnetic fields from constant- α magnetohydrostatic models. *Astron. Astrophys.* **402**, 769. doi:[10.1051/0004-6361:20030227](https://doi.org/10.1051/0004-6361:20030227). 73
- Aulanier, G., DeLuca, E.E., Antiochos, S.K., McMullen, R.A., Golub, L.: 2000, The Topology and Evolution of the Bastille Day Flare. *Astrophys. J.* **540**, 1126. doi:[10.1086/309376](https://doi.org/10.1086/309376). 94

- Aulanier, G., Török, T., Démoulin, P., DeLuca, E.E.: 2010, Formation of torus-unstable flux ropes and electric currents in erupting sigmoids. *Astrophys. J.* **708**, 314. doi:[10.1088/0004-637X/708/1/314](https://doi.org/10.1088/0004-637X/708/1/314). 88
- Balogh, A., Smith, E.J., and D. J. Southwood, B.T.T., Forsyth, R.J., Horbury, T.S.: 1995, The heliospheric magnetic field over the south polar region of the sun. *Science* **268**, 1007. 17, 23, 31, 52
- Bobra, M.G., van Ballegoijen, A.A., DeLuca, E.E.: 2008, Modeling non-potential magnetic fields in solar active regions. *Astrophys. J.* **672**, 1209. doi:[10.1086/523927](https://doi.org/10.1086/523927). 73
- Bogdan, T.J., Low, B.C.: 1986, The three-dimensional structure of magnetostatic atmospheres. *Astrophys. J.* **306**(1), 271. doi:[10.1086/164341](https://doi.org/10.1086/164341). 116
- Borrero, J.M.: 2004, The fine structure of the sunspot penumbra. PhD thesis, Georg-August-Universität zu Göttingen. 4
- Borrero, J.M., Tomczyk, S., Kubo, M., Socas-Navarro, H., Schou, J., Couvidat, S., Bogart, R.: 2011, VFISV: Very Fast Inversion of the Stokes Vector for the Helioseismic and Magnetic Imager. *Sol. Phys.* **273**, 267. doi:[10.1007/s11207-010-9515-6](https://doi.org/10.1007/s11207-010-9515-6). 9
- Calabretta, M.R., Greisen, E.W.: 2002, Representations of celestial coordinates in FITS. *Astron. Astrophys.* **395**, 1077. doi:[10.1051/0004-6361:20021327](https://doi.org/10.1051/0004-6361:20021327). 11, 69
- Cameron, R., Sammis, I.: 1999, Tangential field changes in the great flare of 1990 May 24. *Astrophys. J.* **525**(1), L61. doi:[10.1086/312328](https://doi.org/10.1086/312328). 68
- Cane, H.V., Richardson, I.G.: 2003, Interplanetary coronal mass ejections in the near-Earth solar wind during 1996-2002. *J. Geophys. Res.* **108**(A4), 1156. doi:[10.1029/2002JA009817](https://doi.org/10.1029/2002JA009817). 27
- Démoulin, P., Hénoux, J.C., Priest, E.R., Mandrini, C.H.: 1996, Quasi-separatrix layer in solar flares. *Astron. Astrophys.* **308**, 643. 94, 103
- DeRosa, M.L., Cheung, M.: 2012, Topology of Coronal Fields from Evolving Magnetofrictional Models. In: *American Astronomical Society Meeting Abstracts, American Astronomical Society Meeting Abstracts* **220**, 411.04. 110
- DeRosa, M.L., Schrijver, C.J., Barnes, G., Leka, K.D., Lites, B.W., Aschwanden, M.J., Amari, T., Canou, A., McTiernan, J.M., Régnier, S., Thalmann, J.K., Valori, G., Wheatland, M.S.,

- Wiegmann, T., Chueng, M.C.M., Conlon, P.A., Fuhrmann, M., Inhester, B., Tadesse, T.: 2009, A critical assessment of nonlinear force-free field modeling of the solar corona for active region 10953. *Astrophys. J.* **696**(2), 1780. doi:[10.1088/0004-637X/696/2/1780](https://doi.org/10.1088/0004-637X/696/2/1780). 12, 15, 89, 90, 104, 110
- Emslie, A.G., Kucharek, H., Dennis, B.R., Gopalswamy, N., Holman, G.D., Share, G.H., Vourlidas, A., Forbes, T.G., Gallagher, P.T., Mason, G.M., Metcalf, T.R., Mewaldt, R.A., Murphy, R.J., Schwartz, R.A., Zurbuchen, T.H.: 2004, Energy partition in two solar flare/cme events. *J. Geophys. Res.* **109**(A18), 10104. doi:[10.1029/2004JA010571](https://doi.org/10.1029/2004JA010571). 81
- Falconer, D.A., Moore, R.L., Gary, G.A.: 2006, Magnetic Causes of Solar Coronal Mass Ejections: Dominance of the Free Magnetic Energy over the Magnetic Twist Alone. *Astrophys. J.* **644**, 1258–1272. doi:[10.1086/503699](https://doi.org/10.1086/503699). 110
- Filippov, B., Koutchmy, S., Tavabi, E.: 2012, Formation of a White-Light Jet Within a Quadrupolar Magnetic Configuration. *Sol. Phys.* in press. doi:[10.1007/s11207-011-9911-6](https://doi.org/10.1007/s11207-011-9911-6). 103
- Fisher, G.H., Welsch, B.T., Abbett, W.P.: 2012, Can We Determine Electric Fields and Poynting Fluxes from Vector Magnetograms and Doppler Measurements? *Sol. Phys.* **277**, 153. doi:[10.1007/s11207-011-9816-4](https://doi.org/10.1007/s11207-011-9816-4). 110
- Fletcher, L., Metcalf, T.R., Alexander, D., Brown, D.S., Ryder, L.A.: 2001, Evidence for the Flare Trigger Site and Three-Dimensional Reconnection in Multiwavelength Observations of a Solar Flare. *Astrophys. J.* **554**, 451. doi:[10.1086/321377](https://doi.org/10.1086/321377). 94
- Forbes, T.G.: 2000, A review on the genesis of coronal mass ejections. *J. Geophys. Res.* **105**(A10), 23153. doi:[10.1029/2000JA000005](https://doi.org/10.1029/2000JA000005). 68, 93
- Gary, G.A.: 2001, Plasma beta above a solar active region: Rethinking the paradigm. *Sol. Phys.* **203**, 71. 3, 11, 99
- Gary, G.A., Hagyard, M.J.: 1990, Transformation of vector magnetograms and the problems associated with the effects of perspective and the azimuthal ambiguity. *Sol. Phys.* **126**, 21. 11, 69
- Gibson, S.E., de Toma, G., Emery, B., Riley, P., Zhao, L., Elsworth, Y., Leamon, R.J., Lei, J., McIntosh, S., Mewaldt, R.A., Thompson, B.J., Webb, D.: 2011, The whole heliosphere interval in the context of a long and structured solar minimum: An overview from sun to earth. *Sol. Phys.* **274**, 5. 58

- Gilchrist, S.A., Wheatland, M.S., Leka, K.D.: 2012, The free energy of NOAA solar active region AR 11029. *Sol. Phys.* **276**, 133. doi:[10.1007/s11207-011-9878-3](https://doi.org/10.1007/s11207-011-9878-3). 110
- Golub, L., Deluca, E., Austin, G., Bookbinder, J., Caldwell, D., Cheimets, P., Cirtain, J., Cosmo, M., Reid, P., Sette, A., Weber, M., Sakao, T., Kano, R., Shibasaki, K., Hara, H., Tsuneta, S., Kumagai, K., Tamura, T., Shimojo, M., McCracken, J., Carpenter, J., Haight, H., Siler, R., Wright, E., Tucker, J., Rutledge, H., Barbera, M., Peres, G., Varisco, S.: 2007, The X-Ray Telescope (XRT) for the Hinode Mission. *Sol. Phys.* **243**, 63. doi:[10.1007/s11207-007-0182-1](https://doi.org/10.1007/s11207-007-0182-1). 105
- Gopalswamy, N., Mäkelä, P., Xie, H., Akiyama, S., Yashiro, S.: 2009, CME interactions with coronal holes and their interplanetary consequences. *J. Geophys. Res.* **114**(A13), A00A22. doi:[10.1029/2008JA013686](https://doi.org/10.1029/2008JA013686). 93
- Greene, J.M.: 1992, Locating three-dimensional roots by a bisection method. *J. Comput. Phys.* **98**, 194. doi:[10.1016/0021-9991\(92\)90137-N](https://doi.org/10.1016/0021-9991(92)90137-N). 104
- Guo, Y., Ding, M.D., Wiegmann, T., Li, H.: 2008, 3d magnetic field configuration of the 2006 december 13 flare extrapolated with the optimization method. *Astrophys. J.* **679**, 1629. doi:[10.1086/587684](https://doi.org/10.1086/587684). 73
- Harvey, J., Worden, J.: 1998, New types and uses of synoptic maps. In: Balasubramaniam, K.S., Harvey, J., Rabin, D. (eds.) *Synoptic Solar Physics, Astronomical Society of the Pacific Conference Series* **140**, 155. 7
- Harvey, J.W.: 1969, Magnetic fields associated with solar active-region prominences. PhD thesis, Univ. of Colorado. 4, 10
- Harvey, K., Recely, F.: 2002, Polar coronal holes during cycles 22 and 23. *Sol. Phys.* **211**, 31. 56
- Hathaway, D.H., Rightmire, L.: 2010, Variations in the suns meridional flow over a solar cycle. *Science* **327**, 1350. doi:[10.1126/science.1181990](https://doi.org/10.1126/science.1181990). 53
- Hayashi, K.: 2005, Magnetohydrodynamic simulations of the solar corona and solar wind using a boundary treatment to limit solar wind mass flux. *Astrophys. J. Suppl.* **161**, 480. doi:[10.1086/491791](https://doi.org/10.1086/491791). 50
- Hayashi, K., Zhao, X., Liu, Y.: 2008, MHD simulations of the global solar corona around the Halloween event in 2003 using the synchronic frame format of the solar photospheric magnetic field. *J. Geophys. Res.* **113**(A12), 7104. doi:[10.1029/2007JA012814](https://doi.org/10.1029/2007JA012814). 40, 50

- Haynes, A.L., Parnell, C.E.: 2007, A trilinear method for finding null points in a three-dimensional vector space. *Phys. Plasmas* **14**, 082107. doi:[10.1063/1.2756751](https://doi.org/10.1063/1.2756751). 102, 119
- Haynes, A.L., Parnell, C.E.: 2010, A method for finding three-dimensional magnetic skeletons. *Phys. Plasmas* **17**, 092903. doi:[10.1063/1.3467499](https://doi.org/10.1063/1.3467499). 119
- Hoeksema, J.T.: 1984, Structure and evolution of the large scale solar and heliospheric magnetic fields. PhD thesis, Stanford Univ.. 14, 39, 63, 109, 111
- Hoeksema, J.T., Wilcox, J.M., Scherrer, P.H.: 1982, Structure of the heliospheric current sheet in the early portion of sunspot cycle 21. *J. Geophys. Res.* **87**, 10331. doi:[10.1029/JA087iA12p10331](https://doi.org/10.1029/JA087iA12p10331). 52
- Hoeksema, J.T., Wilcox, J.M., Scherrer, P.H.: 1983, The structure of the heliospheric current sheet - 1978-1982. *J. Geophys. Res.* **88**, 9910. doi:[10.1029/JA088iA12p09910](https://doi.org/10.1029/JA088iA12p09910). 52
- Hoeksema, J.T., Liu, Y., Hayashi, K., Sun, X., Schou, J., Couvidat, S., Elliot, R.C., Barnes, G., Leka, K.D.: 2012, Measuring the vector magnetic field of AR 11158 with HMI. *Sol. Phys.* in preparation. 80, 94
- Holmann, G.D., Sui, L., Schwartz, R.A., Emslie, A.G.: 2003, Electron bremsstrahlung hard x-ray spectra, electron distributions, and energetics in the 2002 July 23 solar flare. *Astrophys. J.* **595**, L97. doi:[10.1086/378488](https://doi.org/10.1086/378488). 80
- Howard, R.A., Moses, J.D., Vourlidas, A., Newmark, J.S., Socker, D.G., Plunkett, S.P., Korendyke, C.M., Cook, J.W., Hurley, A., Davila, J.M., Thompson, W.T., St Cyr, O.C., Mentzell, E., Mehalick, K., Lemen, J.R., Wuelser, J.P., Duncan, D.W., Tarbell, T.D., Wolfson, C.J., Moore, A., Harrison, R.A., Waltham, N.R., Lang, J., Davis, C.J., Eyles, C.J., Mapson-Menard, H., Simnett, G.M., Halain, J.P., Defise, J.M., Mazy, E., Rochus, P., Mercier, R., Ravet, M.F., Delmotte, F., Auchere, F., Delaboudiniere, J.P., Bothmer, V., Deutsch, W., Wang, D., Rich, N., Cooper, S., Stephens, V., Maahs, G., Baugh, R., McMullin, D., Carter, T.: 2008, Sun earth connection coronal and heliospheric investigation (SECCHI). *Space Science Reviews* **136**, 67. doi:[10.1007/s11214-008-9341-4](https://doi.org/10.1007/s11214-008-9341-4). 89, 95
- Hudson, H.S.: 2000, Implosions in coronal transients. *Astrophys. J.* **531**, L75. doi:[10.1086/312516](https://doi.org/10.1086/312516). 16, 68, 84

- Hudson, H.S.: 2011, Global properties of solar flares. *Space Sci. Rev.* **158**, 5. doi:[10.1007/s11214-010-9721-4](https://doi.org/10.1007/s11214-010-9721-4). 68, 78, 87, 93
- Hudson, H.S., Fisher, G.H., Welsch, B.T.: 2008, Flare energy and magnetic field variations. In: *Subsurface and Atmospheric Influences on Solar Activity, ASPC Series* **383**, 221. 85, 88
- Ji, H., Huang, G., Wang, H.: 2007, The relaxation of sheared magnetic fields: A contracting process. *Astrophys. J.* **660**, 893. doi:[10.1086/513017](https://doi.org/10.1086/513017). 68, 88
- Ji, H., Huang, G., Wang, H., Zhou, T., Li, Y., Zhang, Y., Song, M.: 2006, Converging motion of $h\alpha$ conjugate kernels: The signature of fast relaxation of a sheared magnetic field. *Astrophys. J.* **636**, L173. doi:[10.1086/500203](https://doi.org/10.1086/500203). 88
- Jing, J., Chen, P.F., Wiegelmann, T., Xu, Y., Park, S.-H., Wang, H.: 2009, Temporal evolution of free magnetic energy associated with four X-class flares. *Astrophys. J.* **696**, 84. doi:[10.1088/0004-637X/696/1/84](https://doi.org/10.1088/0004-637X/696/1/84). 68, 93
- Jing, J., Yuan, Y., Wiegelmann, T., Xu, Y., Liu, R., Wang, H.: 2010, Non-linear force-free modeling of magnetic fields in a solar filament. *Astrophys. J.* **719**, L56. doi:[10.1088/2041-8205/719/1/L56](https://doi.org/10.1088/2041-8205/719/1/L56). 73
- King, J.H., Papitashvili, N.E.: 2005, Solar wind spatial scales in and comparisons of hourly wind and ACE plasma and magnetic field data. *J. Geophys. Res.* **110**(A9), 2104. doi:[10.1029/2004JA010649](https://doi.org/10.1029/2004JA010649). 22, 46
- Kirk, M.S., Pesnell, W.D., Young, C.A., Hess Webber, S.A.: 2009, Automated detection of euv polar coronal holes during solar cycle 23. *Sol. Phys.* **257**, 99. doi:[10.1007/s11207-009-9369-y](https://doi.org/10.1007/s11207-009-9369-y). 56
- Kojima, M., Kakinuma, T.: 1990, Solar cycle dependence of global distribution of solar wind speed. *Space Science Rev.* **53**, 173. doi:[10.1007/BF00212754](https://doi.org/10.1007/BF00212754). 55
- Kojima, M., Tokumaru, M., Watanabe, H., Yokobe, A., Asai, K., Jackson, B.V., Hick, P.L.: 1998, Heliospheric tomography using interplanetary scintillation observations 2. latitude and helio-centric distance dependence of solar wind structure at 0.1-1 AU. *J. Geophys. Res.* **103**, 1981. doi:[10.1029/97JA02162](https://doi.org/10.1029/97JA02162). 55
- Kosovichev, A.G.: 2011, Helioseismic response to the X2.2 solar flare of 2011 February 15. *Astrophys. J. Lett.* **734**, L15. doi:[10.1088/2041-8205/734/1/L15](https://doi.org/10.1088/2041-8205/734/1/L15). 88, 89

- Kosugi, T., Matsuzaki, K., Sakao, T., Shimizu, T., Sone, Y., Tachikawa, S., Hashimoto, T., Minesugi, K., Ohnishi, A., Yamada, T., Tsuneta, S., Hara, H., Ichimoto, K., Suematsu, Y., Shimojo, M., Watanabe, T., Shimada, S., Davis, J.M., Hill, L.D., Owens, J.K., Title, A.M., Culhane, J.L., Harra, L.K., Doschek, G.A., Golub, L.: 2007, The Hinode (Solar-B) mission: An overview. *Sol. Phys.* **243**, 3. doi:[10.1007/s11207-007-9014-6](https://doi.org/10.1007/s11207-007-9014-6). 82
- Kuckein, C., Centeno, R., Martínez Pillet, V., Casini, R., Manso Sainz, R., Shimizu, T.: 2009, Magnetic field strength of active region filaments. *Astron. Astrophys.* **501**, 1113. doi:[10.1051/0004-6361/200911800](https://doi.org/10.1051/0004-6361/200911800). 73
- Landolfi, M., Landi Degl’Innocenti, E.: 1982, Magneto-optical effects and the determination of vector magnetic fields from Stokes profiles. *Sol. Phys.* **78**, 355. doi:[10.1007/BF00151615](https://doi.org/10.1007/BF00151615). 9
- Lee, C.O., Luhmann, J.G., Zhao, X., Liu, Y., Riley, P., Arge, C.N., Russel, C.T., de Pater, I.: 2009, Effects of the weak polar fields of solar cycle 23: Investigation using OMNI for the STEREO mission period. *Sol. Phys.* **256**(1-2), 345. doi:[10.1007/s11207-009-9345-6](https://doi.org/10.1007/s11207-009-9345-6). 58, 59
- Lee, C.O., Luhmann, J.G., Hoeksema, J.T., Sun, X., Arge, C.N., de Pater, I.: 2011, Coronal field opens at lower height during the solar cycles 22 and 23 minimum periods: IMF comparison suggests the source surface should be lowered. *Sol. Phys.* **269**, 367. doi:[10.1007/s11207-010-9699-9](https://doi.org/10.1007/s11207-010-9699-9). 14, 63, 65
- Leka, K.D., Barnes, G.: 2003, Photospheric magnetic field properties of flaring versus flare-quiet active regions. II. discriminant analysis. *Astrophys. J.* **595**(2), 1296. doi:[10.1086/377512](https://doi.org/10.1086/377512). 110
- Leka, K.D., Barnes, G.: 2007, Photospheric Magnetic Field Properties of Flaring versus Flare-quiet Active Regions. IV. A Statistically Significant Sample. *Astrophys. J.* **656**, 1173. doi:[10.1086/510282](https://doi.org/10.1086/510282). 110
- Leka, K.D., Canfield, R.C., McClymont, A.N., van Driel-Gesztelyi, L.: 1996, Evidence for Current-carrying Emerging Flux. *Astrophys. J.* **462**, 547. doi:[10.1086/177171](https://doi.org/10.1086/177171). 14
- Leka, K.D., Barnes, G., Crouch, A.D., Metcalf, T.R., Gary, G.A., Jing, J., Liu, Y.: 2009, Resolving the 180° ambiguity in solar vector magnetic field data: Evaluating the effects of noise, spatial resolution, and method assumptions. *Sol. Phys.* **260**(1), 83. doi:[10.1007/s11207-009-9440-8](https://doi.org/10.1007/s11207-009-9440-8). 10, 11

- Lemen, J.R., Title, A.M., Akin, D.J., Boerner, P.F., Chou, C., Drake, J.F., Duncan, D.W., Edwards, C.G., Friedlaender, F.M., Heyman, G.F., Hurlburt, N.E., Katz, N.L., Kushner, G.D., Levay, M., Lindgren, R.W., Mathur, D.P., McFeaters, E.L., Mitchell, S., Rehse, R.A., Schrijver, C.J., Springer, L.A., Stern, R.A., Tarbell, T.D., Wuelser, J.-P., Wolfson, C.J., Yanari, C., Bookbinder, J.A., Cheimets, P.N., Caldwell, D., Deluca, E.E., Gates, R., Golub, L., Park, S., Podgorski, W.A., Bush, R.I., Scherrer, P.H., Gummin, M.A., Smith, P., Auker, G., Jerram, P., Pool, P., Soufli, R., Windt, D.L., Beardsley, S., Clapp, M., Lang, J., Waltham, N.: 2012, The Atmospheric Imaging Assembly (AIA) on the Solar Dynamic Observatory (SDO). *Sol. Phys.* **275**, 17. doi:[10.1007/s11207-011-9776-8](https://doi.org/10.1007/s11207-011-9776-8). 69, 94
- Levine, R.H., Altschuler, M.D., Harvey, J.W.: 1977, Solar sources of the interplanetary magnetic field and solar wind. *J. Geophys. Res.* **82**, 1061. 18, 63
- Lin, R.P., Dennis, B.R., Hurford, G.J., Smith, D.M., Zehnder, A., Harvey, P.R., Curtis, D.W., Pankow, D., Turin, P., Bester, M., Csillaghy, A., Lewis, M., Madden, N., van Beek, H.F., Appleby, M., Raudorf, T., McTiernan, J., Ramaty, R., Schmahl, E., Schwartz, R., Krucker, S., Abiad, R., Quinn, T., Berg, P., Hashii, M., Sterling, R., Jackson, R., Pratt, R., Campbell, R.D., Malone, D., Landis, D., Barrington-Leigh, C.P., Slassi-Sennou, S., Cork, C., Clark, D., Amato, D., Orwig, L., Boyle, R., Banks, I.S., Shirey, K., Tolbert, A.K., Zarro, D., Snow, F., Thomsen, K., Henneck, R., McHedlishvili, A., Ming, P., Fivian, M., Jordan, J., Wanner, R., Crubb, J., Preble, J., Matranga, M., Benz, A., Hudson, H., Canfield, R.C., Holman, G.D., Crannell, C., Kosugi, T., Emslie, A.G., Vilmer, N., Brown, J.C., Johns-Krull, C., Aschwanden, M., Metcalf, T., Conway, A.: 2002, The Reuven Ramaty High-Energy Solar Spectroscopic Imager (RHESSI). *Sol. Phys.* **210**, 3. doi:[10.1023/A:1022428818870](https://doi.org/10.1023/A:1022428818870). 80, 103
- Linker, J.A., Mikić, Z., Biesecker, D.A., Forsyth, R.J., Gibson, S.E., Lazarus, A.J., Lecinski, A., Riley, P., Szabo, A., Thompson, B.J.: 1999, Magnetohydrodynamic modeling of the solar corona during Whole Sun Month. *J. Geophys. Res.* **104**(A5), 9809. doi:[10.1029/1998JA900159](https://doi.org/10.1029/1998JA900159). 39
- Liu, C., Deng, N., Falconer, D., Goode, P.R., Denker, C., Wang, H.: 2005, Rapid change of δ spot structure associated with seven major flares. *Astrophys. J.* **622**, 722. doi:[10.1086/427868](https://doi.org/10.1086/427868). 88
- Liu, R., Wang, H.: 2010, Fast contraction of coronal loops at the flare peak. *Astrophys. J.* **714**, L41. doi:[10.1088/2041-8205/714/1/L41](https://doi.org/10.1088/2041-8205/714/1/L41). 68, 85

- Liu, W., Petrosian, V., Dennis, B.R., Holman, G.D.: 2009, Conjugate hard X-ray footpoints in the 2003 october 29 X10 flare: Unshearing motions, correlations, and asymmetries. *Astrophys. J.* **693**, 847. doi:[10.1088/2041-8205/723/1/L53](https://doi.org/10.1088/2041-8205/723/1/L53). 68
- Liu, Y.: 2007, Halo Coronal Mass Ejections and Configuration of the Ambient Magnetic Fields. *Astrophys. J.* **654**, L171. doi:[10.1086/511385](https://doi.org/10.1086/511385). 93
- Liu, Y., Zhao, J.: 2009, Magnetic Field Elements at High Latitude: Lifetime and Rotation Rate. *Sol. Phys.* **260**, 289. doi:[10.1007/s11207-009-9450-6](https://doi.org/10.1007/s11207-009-9450-6). 110
- Liu, Y., Hoeksema, J.T., Zhao, X., Larson, R.M.: 2007, MDI synoptic charts of magnetic field: Interpolation of polar fields. In: *Bulletin of the American Astronomical Society* **38**, 129. 40, 42, 44
- Liu, Y., Hoeksema, J.T., Scherrer, P.H., Schou, J., Couvidat, S., Bush, R.I., Duvall, T.L., Hayashi, K., Sun, X., Zhao, X.: 2012, Comparison of Line-of-Sight Magnetograms Taken by the Solar Dynamics Observatory/Helioseismic and Magnetic Imager and Solar and Heliospheric Observatory/Michelson Doppler Imager. *Sol. Phys.*, 75. in press. doi:[10.1007/s11207-012-9976-x](https://doi.org/10.1007/s11207-012-9976-x). 6
- Longcope, D.W.: 2005, Topological Methods for the Analysis of Solar Magnetic Fields. *Living Reviews in Solar Physics* **2**, 7. 94
- Longcope, D.W., Fisher, G.H., Pevtsov, A.A.: 1998, Flux-tube twist resulting from helical turbulence: The sigma-effect. *Astrophys. J.* **507**, 417. doi:[10.1086/306312](https://doi.org/10.1086/306312). 73
- Luhmann, J.G., Li, Y., Arge, C.N., Gazis, P.R., Ulrich, R.: 2002, Solar cycle changes in coronal holes and space weather cycles. *J. Geophys. Res.* **107**(A8), 1154. 63
- Luhmann, J.G., Lee, C.O., Li, Y., Arge, C.N., Galvin, A.B., Simunac, K., Russell, C.T., Howard, R.A., Petrie, G.: 2009, Solar wind sources in the late declining phase of cycle 23: Effects of the weak solar polar field on high speed streams. *Sol. Phys.* **256**(1-2), 285. doi:[10.1007/s11207-009-9354-5](https://doi.org/10.1007/s11207-009-9354-5). 8, 39, 58, 59
- Luoni, M.L., Démoulin, P., Mandrini, C.H., van Driel-Gesztelyi, L.: 2011, Twisted flux tube emergence evidenced in longitudinal magnetograms: Magnetic tongues. *Sol. Phys.* **270**, 45. doi:[10.1007/s11207-011-9731-8](https://doi.org/10.1007/s11207-011-9731-8). 72

- Mackay, D.H., Karpen, J.T., Ballester, J.L., Schmieder, B., Aulanier, G.: 2010, Physics of solar prominences: II magnetic structure and dynamics. *Space Sci. Rev.* **151**, 333. doi:[10.1007/s11214-010-9628-0](https://doi.org/10.1007/s11214-010-9628-0). 74
- Mandrini, C.H., Demoulin, P., Schmieder, B., Deluca, E.E., Pariat, E., Uddin, W.: 2006, Companion Event and Precursor of the X17 Flare on 28 October 2003. *Sol. Phys.* **238**, 293. doi:[10.1007/s11207-006-0205-3](https://doi.org/10.1007/s11207-006-0205-3). 94, 103
- Mason, J.P., Hoeksema, J.T.: 2010, Testing Automated Solar Flare Forecasting with 13 Years of Michelson Doppler Imager Magnetograms. *Astrophys. J.* **723**, 634. doi:[10.1088/0004-637X/723/1/634](https://doi.org/10.1088/0004-637X/723/1/634). 110
- Masson, S., Pariat, E., Aulanier, G., Schrijver, C.J.: 2009, The Nature of Flare Ribbons in Coronal Null-Point Topology. *Astrophys. J.* **700**, 559. doi:[10.1088/0004-637X/700/1/559](https://doi.org/10.1088/0004-637X/700/1/559). 94
- Maurya, R.A., Reddy, V., Ambastha, A.: 2012, Velocity and magnetic transients driven by the X2.2 white-light flare of 2011 February 15 in NOAA 11158. *Astrophys. J.* **747**, 134. doi:[10.1088/0004-637X/747/2/134](https://doi.org/10.1088/0004-637X/747/2/134). 89
- McGregor, N.L., Hughes, W.J., Arge, C.N., Owens, M.J.: 2008, Analysis of the magnetic field discontinuity at the potential field source surface and schatten current sheet interface in the wang-sheeley-arge model. *J. Geophys. Res.* **113**(A12), 8112. doi:[10.1029/2007JA012330](https://doi.org/10.1029/2007JA012330). 31
- Metcalf, T.R.: 1994, Resolving the 180-degree ambiguity in vector magnetic field measurements: The 'minimum' energy solution. *Sol. Phys.* **155**(2), 235. doi:[10.1007/BF00680593](https://doi.org/10.1007/BF00680593). 10
- Metcalf, T.R., Leka, K.D., Mickey, D.L.: 2005, Magnetic free energy in NOAA active region 10486 on 2003 October 29. *Astrophys. J. Lett.* **623**, L53. doi:[10.1086/429961](https://doi.org/10.1086/429961). 80
- Metcalf, T.R., Jiao, L., McClymont, A.N., Canfield, R.C., Ultenbroek, H.: 1995, Is the solar chromosphere magnetic field force-free? *Astrophys. J.* **439**, 474. doi:[10.1086/175188](https://doi.org/10.1086/175188). 12, 69, 89
- Metcalf, T.R., Leka, K.D., Barnes, G., Lites, B.W., Georgoulis, M.K., Pevtsov, A.A., Balasubramaniam, K.S., Gary, G.A., Jing, J., Li, J., Liu, Y., Wang, H.M., Abramenko, V., Yurchyshyn, V., Moon, Y.-J.: 2006, An overview of existing algorithms for resolving the 180° ambiguity in vector magnetic fields: Quantitative tests with synthetic data. *Sol. Phys.* **237**(2), 267. doi:[10.1007/s11207-006-0170-x](https://doi.org/10.1007/s11207-006-0170-x). 10

- Metcalf, T.R., DeRosa, M.L., Schrijver, C.J., Barnes, G., van Ballegooijen, A.A., Wiegmann, T., Wheatland, M.S., Valori, G., McTiernan, J.M.: 2008, Nonlinear force-free modeling of coronal magnetic fields. II. modeling a filament arcade and simulated chromospheric and photospheric vector fields. *Sol. Phys.* **247**(2), 269. doi:[10.1007/s11207-007-9110-7](https://doi.org/10.1007/s11207-007-9110-7). 15, 80, 89
- Meunier, N.: 2005, Magnetic network dynamics: Activity level, feature size and anchoring depth. *Astron. Astrophys.* **436**(3), 1075. doi:[10.1051/0004-6361:20042414](https://doi.org/10.1051/0004-6361:20042414). 7, 45
- Moore, R.L., Sterling, A.C., Hudson, H.S., Lemen, J.R.: 2001, Onset of the magnetic explosion in solar flares and coronal mass ejections. *Astrophys. J.* **552**, 833. doi:[10.1086/320559](https://doi.org/10.1086/320559). 88
- Moore, R.L., Cirtain, J.W., Sterling, A.C., Falconer, D.A.: 2010, Dichotomy of Solar Coronal Jets: Standard Jets and Blowout Jets. *Astrophys. J.* **720**, 757. doi:[10.1088/0004-637X/720/1/757](https://doi.org/10.1088/0004-637X/720/1/757). 106
- Moreno-Insertis, F., Galsgaard, K., Ugarte-Urra, I.: 2008, Jets in Coronal Holes: Hinode Observations and Three-dimensional Computer Modeling. *Astrophys. J.* **673**, L211. doi:[10.1086/527560](https://doi.org/10.1086/527560). 94
- Nandy, D., Muñoz-Jaramillo, A., Martens, P.C.H.: 2011, The Unusual Minimum of sunspot cycle 23 caused by meridional plasma flow variations. *Nature* **471**, 80. doi:[10.1038/nature09786](https://doi.org/10.1038/nature09786). 53
- Neugebauer, M., Forsyth, R.J., Galvin, A.B., Harvey, K.L., Hoeksema, J.T., Lazarus, A.J., Leping, R.P., Linker, J.A., Mikić, Z., Steinberg, J.T., von Steiger, R., Wang, Y.M., Wimmer-Schweingruber, R.F.: 1998, Spatial structure of the solar wind and comparisons with solar data and models. *J. Geophys. Res.* **103**(A7), 14587. doi:[10.1029/98JA00798](https://doi.org/10.1029/98JA00798). 17, 37, 49, 52, 63
- Neugebauer, M., Liewer, P.C., Smith, E.J., Skoug, R.M., Zurbuchen, T.H.: 2002, Sources of the solar wind at solar activity maximum. *J. Geophys. Res.* **107**(A12), 1488. doi:[10.1029/2001JA000306](https://doi.org/10.1029/2001JA000306). 17, 29, 37, 52, 63, 67
- Owens, M.J., Arge, C.N., Spence, H.E., Pembroke, A.: 2005, An event-based approach to validating solar wind speed predictions: High-speed enhancements in the Wang-Sheeley-Arge model. *J. Geophys. Res.* **110**(A12), 12105. doi:[10.1029/2005JA011343](https://doi.org/10.1029/2005JA011343). 21, 25, 28, 60
- Owens, M.J., Spence, H.E., McGregor, S., Huges, W.J., Quinn, J.M., Arge, C.N., Riley, P., Linker, J., Odstrčil, D.: 2008, Metrics for solar wind prediction models: comparison of empirical, hybrid and physics-based schemes with 8 years of *l1* observations. *Space Weather* **6**(S08001), 12. doi:[10.1029/2007SW000380](https://doi.org/10.1029/2007SW000380). 47

- Pariat, E., Antiochos, S.K., DeVore, C.R.: 2009, A Model for Solar Polar Jets. *Astrophys. J.* **691**, 61. doi:[10.1088/0004-637X/691/1/61](https://doi.org/10.1088/0004-637X/691/1/61). 94
- Parker, E.N.: 1958, Dynamics of the interplanetary gas and magnetic fields. *Astrophys. J.* **128**, 664. 3
- Parker, E.N.: 1961, The stellar-wind regions. *Astrophys. J.* **134**, 20. doi:[10.1086/147124](https://doi.org/10.1086/147124). 3, 17
- Parnell, C.E., Smith, J.M., Neukirch, T., Priest, E.R.: 1996, The structure of three dimensional magnetic neutral points. *Phys. Plasmas* **3**, 759. doi:[10.1063/1.871810](https://doi.org/10.1063/1.871810). 102, 119, 122, 123
- Poduval, B., Zhao, X.: 2004, Discrepancies in the prediction of solar wind using potential field source surface model: An investigation of possible sources. *J. Geophys. Res.* **109**(A18), 8102. doi:[10.1029/2004JA010384](https://doi.org/10.1029/2004JA010384). 29
- Priest, E., Forbes, T. (eds.): 2000, *Magnetic reconnection: MHD theory and applications*. 3, 94
- Reardon, K.P., Wang, Y.-M., Muglach, K., Warren, H.P.: 2011, Evidence for two separate but inter-laced components of the chromospheric magnetic field. *Astrophys. J.* **742**, 119. doi:[10.1088/0004-637X/742/2/119](https://doi.org/10.1088/0004-637X/742/2/119). 104
- R gnier, S., Canfield, R.C.: 2006, Evolution of magnetic fields and energetics of flares in active region 8210. *Astron. Astrophys.* **451**, 319. doi:[10.1051/0004-6361:20054171](https://doi.org/10.1051/0004-6361:20054171). 68, 93
- Richardson, I.G., Cane, H.V.: 1995, Regions of abnormally low proton temperature in the solar wind (1965-1991) and their association with ejecta. *J. Geophys. Res.* **100**(A12), 23397. doi:[10.1029/95JA02684](https://doi.org/10.1029/95JA02684). 22
- Riley, P., Linker, J., Mikić, Z., Lionello, R.: 2001, MHD modeling of the solar corona and inner heliosphere: Comparison with observations. In: Song, P., Singer, H., Siscoe, G. (eds.) *Space Weather Geophysical Monograph Series* **125**, Washington D. C., 159. 19
- Riley, P., Linker, J., Mikić, Z., Lionello, R., Ledvina, S.A., Luhmann, J.G.: 2006, A comparison between global solar magnetohydrodynamic and potential field source surface model results. *Astrophys. J.* **653**, 1510. doi:[10.1086/508565](https://doi.org/10.1086/508565). 14
- Sakao, T., Kano, R., Narukage, N., Kotoku, J., Bando, T., DeLuca, E.E., Lundquist, L.L., Tsuneta, S., Harra, L.K., Katsukawa, Y., Kubo, M., Hara, H., Matsuzaki, K., Shimojo, M., Bookbinder, J.A., Golub, L., Korreck, K.E., Su, Y., Shibasaki, K., Shimizu, T., Nakatani, I.: 2007, Continuous

- plasma outflows from the edge of a solar active region as a possible source of solar wind. *Science* **318**(5856), 1585. doi:[10.1126/science.1147292](https://doi.org/10.1126/science.1147292). 52
- Sakurai, T.: 1989, Computational modeling of magnetic fields in solar active regions. *Space Sci. Rev.* **51**, 11. doi:[10.1007/BF00226267](https://doi.org/10.1007/BF00226267). 13
- Schatten, K.H.: 1971, Current sheet magnetic model for the solar corona. *Cosmic Electrodyn.* **2**, 232. 14, 31, 116, 117, 118
- Schatten, K.H., Wilcox, J.M., Ness, N.F.: 1969, A model of interplanetary and coronal magnetic fields. *Sol. Phys.* **6**(3), 442. doi:[10.1007/BF00146478](https://doi.org/10.1007/BF00146478). 13, 18, 39, 63
- Scherrer, P.H., Wilcox, J.M., Svalgaard, L., Duvall, T.L. Jr., Dittmer, P.H., Gustafson, E.K.: 1977, The mean magnetic field of the sun - Observations at Stanford. *Sol. Phys.* **54**, 353. doi:[10.1007/BF00159925](https://doi.org/10.1007/BF00159925). 5
- Scherrer, P.H., Bogart, R.S., Bush, R.I., Hoeksema, J.T., Kosovichev, A.G., Schou, J., Rosenberg, W., Springer, L., Tarbell, T.D., Title, A., Wolfson, C.J., Zayer, I., Team, M.E.: 1995, The Solar oscillations investigation - Michelson Doppler Imager. *Sol. Phys.* **162**(1-2), 129. doi:[10.1007/BF00733429](https://doi.org/10.1007/BF00733429). 5
- Schou, J., Brown, T.M.: 1994, Generation of artificial helioseismic time-series. *Astron. Astrophys. Suppl.* **107**, 541. 115
- Schou, J., Scherrer, P.H., Bush, R.I., Wachter, R., Couvidat, S., Rabello-Soares, M.C., Bogart, R.S., Hoeksema, J.T., Liu, Y., Duvall, T.L. Jr., Akin, D.J., Allard, B.A., Miles, J.W., Rairden, R., Shine, R.A., Tarbell, T.D., Title, A.M., Wolfson, C.J., Elmore, D.F., Norton, A.A., Tomczyk, S.: 2012, Design and ground calibration of the Helioseismic and Magnetic Imager (HMI) instrument on the Solar Dynamic Observatory (SDO). *Sol. Phys.* **275**, 229. doi:[10.1007/s11207-011-9842-2](https://doi.org/10.1007/s11207-011-9842-2). 5, 94
- Schrijver, C.J.: 2009, Driving major solar flares and eruptions: A review. *Advances in Space Research* **43**, 739. doi:[10.1016/j.asr.2008.11.004](https://doi.org/10.1016/j.asr.2008.11.004). 15, 68, 74, 93
- Schrijver, C.J., DeRosa, M.L.: 2003, Photospheric and heliospheric magnetic fields. *Sol. Phys.* **212**(1), 165. doi:[10.1023/A:1022908504100](https://doi.org/10.1023/A:1022908504100). 41, 58, 63
- Schrijver, C.J., Title, A.M.: 2011, Long-range magnetic couplings between solar flares and coronal mass ejections observed by SDO and STEREO. *J. Geophys. Res.* **116**(A4), 4108. 20

- Schrijver, C.J., DeRosa, M.L., Title, A.M., Metcalf, T.: 2005, The nonpotentiality of active-region coronae and the dynamics of the photospheric magnetic field. *Astrophys. J.* **628**, 501. doi:[10.1086/430733](https://doi.org/10.1086/430733). 68
- Schrijver, C.J., DeRosa, M.L., Metcalf, T.R., Liu, Y., McTiernan, J., Régnier, S., Valori, G., Wheatland, M.S., Wiegmann, T.: 2006, Nonlinear force-free modeling of coronal magnetic fields part I: A quantitative comparison of methods. *Sol. Phys.* **235**(1-2), 161. doi:[10.1007/s11207-006-0068-7](https://doi.org/10.1007/s11207-006-0068-7). 15
- Schrijver, C.J., DeRosa, M.L., Metcalf, T., Barnes, G., Lites, B., Tarbell, T., McTiernan, J.M., Valori, G., Wiegmann, T., Wheatland, M.S., Amari, T., Aulanier, G., Démoulin, P., Fuhrmann, M., Kusano, K., Régnier, S., Thalmann, J.K.: 2008, Nonlinear force-free field modeling of a solar active region around the time of a major flare and coronal mass ejection. *Astrophys. J.* **675**(2), 1637. doi:[10.1086/527413](https://doi.org/10.1086/527413). 12, 74, 90
- Schrijver, C.J., Aulanier, G., Title, A.M., Pariat, E., Delannée, C.: 2011, The 2011 February 15 x2 flare, ribbons, and mass ejection: Interpreting the three-dimensional views from the Solar Dynamics Observatory and STEREO guided by magnetohydrodynamic flux-rope modeling. *Astrophys. J.* **738**, 167. doi:[10.1088/0004-637X/738/2/167](https://doi.org/10.1088/0004-637X/738/2/167). 70, 72, 74, 85, 88, 94
- Shibata, K., Nitta, N., Strong, K.T., Matsumoto, R., Yokoyama, T., Hirayama, T., Hudson, H., Ogawara, Y.: 1994, A gigantic coronal jet ejected from a compact active region in a coronal hole. *Astrophys. J.* **431**, L51. doi:[10.1086/187470](https://doi.org/10.1086/187470). 104
- Shibata, K., Masuda, S., Shimojo, M., Hara, H., Yokoyama, T., Tsuneta, S., Kosugi, T., Ogawara, Y.: 1995, Hot-Plasma Ejections Associated with Compact-Loop Solar Flares. *Astrophys. J.* **451**, L83. doi:[10.1086/309688](https://doi.org/10.1086/309688). 103
- Shibata, K., Shimojo, M., Yokoyama, T., Ohya, M.: 1997, Theory and Observations of X-Ray Jets. In: Bentley, R.D., Mariska, J.T. (eds.) *Magnetic Reconnection in the Solar Atmosphere*, *Astronomical Society of the Pacific Conference Series* **111**, 29. 93, 97, 105
- Shiota, D., Tsuneta, S., Shimojo, M., Sako, N., Orozco Suárez, D., Ishikawa, R.: 2012, Polar Field Reversal Observations with Hinode. *Astrophys. J.* **753**, 157. doi:[10.1088/0004-637X/753/2/157](https://doi.org/10.1088/0004-637X/753/2/157). 110

- Smith, E.J., Balogh, A.: 2008, Decrease in heliospheric magnetic flux in this solar minimum: Recent Ulysses magnetic field observations. *Geophys. Res. Lett.* **35**, 22103. doi:[10.1029/2008GL035345](https://doi.org/10.1029/2008GL035345). 53
- Stenflo, J.O.: 1994, *Solar magnetic fields: Polarized radiation diagnostics*, Kluwer Academic Publishers, Dordrecht, The Netherlands. 4
- Su, J.T., Shen, Y.D., Liu, Y.: 2012, Extreme-Ultraviolet Multi-wavelength Observation of Quasi-Periodic Pulsations in a Solar Post-Flare Cusp-Shape Loop with SDO/AIA. *Astrophys. J.* **754**, 43. doi:[10.1088/0004-637X/754/1/43](https://doi.org/10.1088/0004-637X/754/1/43). 97, 105, 106
- Su, Y., Golub, L., Van Ballegooijen, A.A.: 2007, A statistical study of shear motion of the footpoints in two-ribbon flares. *Astrophys. J.* **655**, 606. doi:[10.1086/510065](https://doi.org/10.1086/510065). 88
- Su, Y., Surges, V., Van Ballegooijen, A.A., DeLuca, E.E., Golub, L.: 2011, Observations and magnetic field modeling of the flare/coronal mass ejection event on 2010 April 8. *Astrophys. J.* **734**, 53. doi:[10.1088/0004-637X/734/1/53](https://doi.org/10.1088/0004-637X/734/1/53). 73
- Sudol, J.J., Harvey, J.W.: 2005, Longitudinal magnetic field changes accompanying solar flares. *Astrophys. J.* **653**, 647. doi:[10.1086/497361](https://doi.org/10.1086/497361). 68
- Sun, X., Hoeksema, J.T.: 2009, A New Source Surface Radius in Potential Field Modeling During the Current Weak Solar Minimum? *AGU Fall Meeting*, A1487. 67
- Sun, X., Liu, Y., Hoeksema, J.T.: 2008, Polar magnetic fields observed during the last four solar minima. *AGU Fall Meeting*, 1589–. 53, 58, 59, 60, 65, 67
- Sun, X., Liu, Y., Hoeksema, J.T., Hayashi, K.: 2011, A new method for polar field interpolation. *Sol. Phys.* **270**(1), 9. doi:[10.1007/s11207-011-9751-4](https://doi.org/10.1007/s11207-011-9751-4). 8, 20, 25, 51
- Sun, X., Hoeksema, J.T., Liu, Y., Chen, Q., Hayashi, K.: 2012b, A Non-radial Eruption in A Quadrupolar Magnetic Configuration With A Coronal Null. *Astrophys. J.* in press. 107, 123
- Sun, X., Hoeksema, J.T., Liu, Y., Wiegmann, T., Hayashi, K., Chen, Q., Thalmann, J.: 2012a, Evolution of Magnetic Field and Energy in a Major Eruptive Active Region Based on SDO/HMI Observation. *Astrophys. J.* **748**, 77. doi:[10.1088/0004-637X/748/2/77](https://doi.org/10.1088/0004-637X/748/2/77). 74, 92, 93, 97, 98, 99
- Svalgaard, L., Duvall, T.L. Jr., Scherrer, P.H.: 1978, The strength of the sun's polar fields. *Sol. Phys.* **58**, 225. 41

- Tadesse, T., Wiegmann, T., Inhester, B., Pevtsov, A.: 2012, Magnetic connectivity between active regions 10987, 10988, and 10989 by means of nonlinear force-free field extrapolation. *Sol. Phys.* **277**, 119. doi:[10.1007/s11207-011-9764-z](https://doi.org/10.1007/s11207-011-9764-z). 91, 110
- Taylor, J.R.: 1997, *An introduction to error analysis: The study of uncertainties in physical measurement, 2nd ed.*, University Science Books, ???, 25
- Thalmann, J.K.: 2010, Evolution of coronal magnetic fields. PhD thesis, Technischen Universitt Carolo-Wilhelmina. 14
- Thalmann, J.K., Wiegmann, T.: 2008, Evolution of the flaring active region NOAA 10540 as a sequence of nonlinear force-free field extrapolations. *Astron. Astrophys.* **484**, 495. doi:[10.1051/0004-6361:200809508](https://doi.org/10.1051/0004-6361:200809508). 68, 93
- Thompson, B.J., Gibson, S.E., Schroeder, P.C., Webb, D.F., Arge, C.N., Bisi, M.M., de Toma, G., Emery, B.A., Galvin, A.B., Haber, D.A., Jackson, B.V., Jensen, E.A., Leamon, R.J., Lei, J., Manoharan, P.K., Mays, M.L., McIntosh, P.S., Petrie, G.J.D., Plunkett, S.P., Qian, L., Riley, P., Suess, S.T., Tokumaru, M., Welsch, B.T., Woods, T.N.: 2011a, A Snapshot of the Sun Near Solar Minimum: The Whole Heliosphere Interval. *Sol. Phys.* **274**, 29. doi:[10.1007/s11207-011-9891-6](https://doi.org/10.1007/s11207-011-9891-6). 53
- Thompson, B., Démoulin, P., Mandrini, C., Mays, M., Ofman, L., Van Driel-Gesztelyi, L., Viall, N.: 2011b, Pulsed Flows Along a Cusp Structure Observed with SDO/AIA. In: *AAS/Solar Physics Division Abstracts #42*, 2117. 97, 105
- Thompson, W.T.: 2006, Coordinate systems for solar image data. *Astron. Astrophys.* **449**, 791. doi:[10.1051/0004-6361:20054262](https://doi.org/10.1051/0004-6361:20054262). 11, 69
- Tian, H., McIntosh, S.W., Xia, L., He, J., Wang, X.: 2012, What can We Learn about Solar Coronal Mass Ejections, Coronal Dimmings, and Extreme-ultraviolet Jets through Spectroscopic Observations? *Astrophys. J.* **748**, 106. doi:[10.1088/0004-637X/748/2/106](https://doi.org/10.1088/0004-637X/748/2/106). 97, 106
- Titov, V.S., Hornig, G., Démoulin, P.: 2002, Theory of magnetic connectivity in the solar corona. *J. Geophys. Res.* **107**, 1164. doi:[10.1029/2001JA000278](https://doi.org/10.1029/2001JA000278). 104
- Tiwari, S.K., Venkatakrishnan, P., Gosain, S., Joshi, J.: 2009, Effect of polarimetric noise on the estimation of twist and magnetic energy of force-free fields. *Astrophys. J.* **700**, 199. doi:[10.1088/0004-637X/700/1/199](https://doi.org/10.1088/0004-637X/700/1/199). 80

- Török, T., Panasenco, O., Titov, V.S., Mikić, Z., Reeves, K.K., Velli, M., Linker, J.A., De Toma, G.: 2011, A Model for Magnetically Coupled Sympathetic Eruptions. *Astrophys. J.* **739**, L63. doi:[10.1088/2041-8205/739/2/L63](https://doi.org/10.1088/2041-8205/739/2/L63). 94
- Tsuneta, S.: 1996, Structure and Dynamics of Magnetic Reconnection in a Solar Flare. *Astrophys. J.* **456**, 840. doi:[10.1086/176701](https://doi.org/10.1086/176701). 104
- Tsuneta, S., Ichimoto, K., Katsukawa, Y., Nagata, S., Otsubo, M., Shimizu, T., Suematsu, Y., Nagagiri, M., Noguchi, M., Tarbell, T., Title, A., Shine, R., Rosenberg, W., Hoffmann, C., Jurcevich, B., Kushner, G., Levay, M., Lites, B., Elmore, D., Matsushita, T., Kawaguchi, N., Saito, H., Mikami, I., Hill, L.D., Owens, J.K.: 2008, The Solar Optical Telescope for the Hinode mission: An overview. *Sol. Phys.* **249**, 167. doi:[10.1007/s11207-008-9174-z](https://doi.org/10.1007/s11207-008-9174-z). 82, 103
- Turmon, M., Jones, H.P., Malanushenko, O.V., Pap, J.M.: 2010, Statistical feature recognition for multidimensional solar imagery. *Sol. Phys.* **262**(2), 277. doi:[10.1007/s11207-009-9490-y](https://doi.org/10.1007/s11207-009-9490-y). 8
- Wang, H.: 2006, Rapid changes of photospheric magnetic fields around flaring magnetic neutral lines. *Astrophys. J.* **649**, 490. doi:[10.1086/506320](https://doi.org/10.1086/506320). 68
- Wang, H., Ewell, M.W., Zirin, H., Ai, G.: 1994, Vector magnetic field changes associated with x-class flares. *Astrophys. J.* **424**, 436. doi:[10.1086/173901](https://doi.org/10.1086/173901). 68, 84, 87
- Wang, S., Liu, C., Liu, R., Deng, N., Liu, Y., Wang, H.: 2012, First flare-related rapid change of photospheric magnetic field observed by Solar Dynamics Observatory. *Astrophys. J.* **745**, L17. doi:[10.1088/2041-8205/745/2/L17](https://doi.org/10.1088/2041-8205/745/2/L17). 81
- Wang, Y.M., Robbrecht, E.: 2011, Asymmetric sunspot activity and the southward displacement of the heliospheric current sheet. *Astrophys. J.* **736**, 136. doi:[10.1088/0004-637X/736/2/136](https://doi.org/10.1088/0004-637X/736/2/136). 53
- Wang, Y.M., Sheeley, N.R. Jr.: 1988, The solar origin of long-term variations of the interplanetary magnetic field strength. *J. Geophys. Res.* **93**(A10), 11227. 14, 41, 63
- Wang, Y.M., Sheeley, N.R. Jr.: 1990, Solar wind speed and coronal flux-tube expansion. *Astrophys. J.* **355**, 726. doi:[10.1086/168805](https://doi.org/10.1086/168805). 18, 34, 35, 39
- Wang, Y.M., Sheeley, N.R. Jr.: 1992, On potential field models of the solar corona. *Astrophys. J.* **392**, 310. doi:[10.1086/171430](https://doi.org/10.1086/171430). 7, 13, 111

- Wang, Y.M., Sheeley, N.R. Jr.: 1995, Solar implication of ulysses interplanetary field measurements. *Astrophys. J. Lett.* **447**, L143. doi:[10.1086/309578](https://doi.org/10.1086/309578). 63, 64
- Wang, Y.M., Nash, A.G., Sheeley, N.R. Jr.: 1989a, Evolution of the sun's polar fields during sunspot cycle 21 - poleward surges and long-term behavior. *Astrophys. J.* **347**, 529. doi:[10.1086/168143](https://doi.org/10.1086/168143). 109
- Wang, Y.M., Nash, A.G., Sheeley, N.R. Jr.: 1989b, Magnetic flux transport on the sun. *Science* **245**, 712. doi:[10.1126/science.245.4919.712](https://doi.org/10.1126/science.245.4919.712). 55, 110
- Wang, Y.M., Robbrecht, E., Sheeley, N.R. Jr.: 2009, On the weakening of the polar magnetic fields during solar cycle 23. *Astrophys. J.* **707**, 1372. doi:[10.1088/0004-637X/707/2/1372](https://doi.org/10.1088/0004-637X/707/2/1372). 53, 58, 60
- Wang, Y.M., Sheeley, N.R. Jr., Rich, N.B.: 2007a, Coronal pseudostreamers. *Astrophys. J.* **658**, 1340. doi:[10.1086/511416](https://doi.org/10.1086/511416). 32
- Wang, Y.M., Sheeley, N.R. Jr., Howard, R.A., Kraemer, J.R., Rich, N.B., Andrews, M.D., Brueckner, G.E., Dere, K.P., Koomen, M.J., Korendyke, C.M., Michels, D.J., Moses, J.D., Paswaters, S.E., Socker, D.G., Wang, D., Lamy, P.L., Liebaria, A., Vibert, D., Schwenn, R., Simnett, G.M.: 1997, Origin and evolution of coronal streamer structure during the 1996 minimum activity phase. *Astrophys. J.* **485**, 875. doi:[10.1086/304467](https://doi.org/10.1086/304467). 53
- Wang, Y.M., Biersteker, J.B., Sheeley, N.R. Jr., Koutchmy, S., Mouette, J., Druckmüller, M.: 2007b, The solar eclipse of 2006 and the origin of raylike features in the white-light corona. *Astrophys. J.* **660**, 882. doi:[10.1086/512480](https://doi.org/10.1086/512480). 32, 53
- Wang, Y.M., Robbrecht, E., Rouillard, A.P., Sheeley, N.R. Jr., Thernisien, A.F.R.: 2010, Formation and evolution of coronal holes following the emergence of active regions. *Astrophys. J.* **715**, 39. doi:[10.1088/0004-637X/715/1/39](https://doi.org/10.1088/0004-637X/715/1/39). 30, 59
- Wang, Y., Chen, C., Gui, B., Shen, C., Ye, P., Wang, S.: 2011, Statistical study of coronal mass ejection source locations: Understanding CMEs viewed in coronagraphs. *J. Geophys. Res.* **116**(A15), 4104. doi:[10.1029/2010JA016101](https://doi.org/10.1029/2010JA016101). 93
- Welsch, B.T., Fisher, G.H.: 2012, A Magnetic Calibration of Photospheric Doppler Velocities. *ArXiv e-prints*. 110
- Wiegmann, T.: 2004, Optimization code with weighting function for the reconstruction of coronal magnetic fields. *Sol. Phys.* **219**(1), 87. doi:[10.1023/B:SOLA.0000021799.39465.36](https://doi.org/10.1023/B:SOLA.0000021799.39465.36). 15, 69

- Wiegmann, T., Inhester, B.: 2010, How to deal with measurement errors and lacking data in nonlinear force-free coronal magnetic field modelling? *Astron. Astrophys.* **516**, A107. doi:[10.1051/0004-6361/201014391](https://doi.org/10.1051/0004-6361/201014391). 90
- Wiegmann, T., Inhester, B., Sakurai, T.: 2006, Preprocessing of vector magnetograph data for a nonlinear force-free magnetic field reconstruction. *Sol. Phys.* **233**(2), 215. doi:[10.1007/s11207-006-2092-z](https://doi.org/10.1007/s11207-006-2092-z). 15, 90
- Wiegmann, T., Thalmann, J.K., Schrijver, C.J., DeRosa, M.L., Metcalf, T.R.: 2008, Can we improve the preprocessing of photospheric vector magnetograms by the inclusion of chromospheric observations? *Sol. Phys.* **247**, 249. doi:[10.1007/s11207-008-9130-y](https://doi.org/10.1007/s11207-008-9130-y). 15
- Wiegmann, T., Thalmann, J.K., Inhester, B., Tadesse, T., Sun, X., Hoeksema, J.T.: 2012, How to optimize non-linear force-free coronal magnetic field extrapolations from SDO/HMI vector magnetograms? *Sol. Phys.* in press. 89, 90, 110
- Wolfson, R.: 1985, A coronal magnetic model with volume and sheet current. *Astrophys. J.* **288**, 769. 14
- Xiao, C.J., Wang, X.G., Pu, Z.Y., Zhao, H., Wang, J.X., Ma, Z.W., Fu, S.Y., Kivelson, M.G., Liu, Z.X., Zong, Q.G., Glassmeier, K.H., Balogh, A., Korth, A., Reme, H., Escoubet, C.P.: 2006, In situ evidence for the structure of the magnetic null in a 3D reconnection event in the Earth's magnetotail. *Nat. Phys.* **2**, 478. doi:[10.1038/nphys342](https://doi.org/10.1038/nphys342). 123
- Yamamoto, T.T., Kusano, K.: 2012, Preprocessing Magnetic Fields with Chromospheric Longitudinal Fields. *Astrophys. J.* **752**, 126. doi:[10.1088/0004-637X/752/2/126](https://doi.org/10.1088/0004-637X/752/2/126). 110
- Zhao, L., Fisk, L.: 2011, Understanding the Behavior of the Heliospheric Magnetic Field and the Solar Wind During the Unusual Solar Minimum Between Cycles 23 and 24. *Sol. Phys.* **274**, 379. doi:[10.1007/s11207-011-9840-4](https://doi.org/10.1007/s11207-011-9840-4). 53
- Zhao, X., Hoeksema, J.T.: 1994, A coronal magnetic field model with horizontal volume and sheet currents. *Sol. Phys.* **151**(1), 91. 31, 116
- Zhao, X., Hoeksema, J.T.: 1995, Prediction of the interplanetary magnetic field strength. *J. Geophys. Res.* **100**(A1), 19. 14, 116

- Zhao, X., Hoeksema, J.T., Scherrer, P.H.: 1999, Changes of the boot-shaped coronal hole boundary during Whole Sun Month near sunspot minimum. *J. Geophys. Res.* **104**(A5), 9735. doi:[10.1029/1998JA900010](https://doi.org/10.1029/1998JA900010). 7, 8, 23
- Zhao, X., Hoeksema, J.T., Scherrer, P.H.: 2005, Prediction and understanding of the north-south displacement of the heliospheric current sheet. *J. Geophys. Res.* **110**(A10), 10101. 53
- Zhao, X., Hoeksema, J.T., Liu, Y., Scherrer, P.H.: 2006, Success rate of predicting the heliospheric magnetic field polarity with Michelson Doppler Imager (MDI) synoptic charts. *J. Geophys. Res.* **111**(A10), 10108. 25
- Zharkov, S., Green, L.M., Matthews, S.A., Zharkova, V.V.: 2011, 2011 february 15: Sunquakes produced by flux rope eruption. *Astrophys. J.* **741**, L35. doi:[10.1088/2041-8205/741/2/L35](https://doi.org/10.1088/2041-8205/741/2/L35). 88
- Zurbuchen, T.H.: 2007, A new view of the coupling of the sun and the heliosphere. *Annu. Rev. Astron. Astrophys.* **45**, 297. 52